# 7. Saturn Atmospheric Structure and Dynamics

Anthony D. Del Genio
NASA Goddard Institute for Space Studies, 2880 Broadway, New York, NY 10025

Richard K. Achterberg
University of Maryland, Department of Astronomy, College Park, MD 20742

Kevin H. Baines
Jet Propulsion Laboratory, 4800 Oak Grove Drive, Pasadena, CA 91109

F. Michael Flasar
NASA Goddard Space Flight Center, Greenbelt, MD 20771

Peter L. Read
Atmospheric, Oceanic & Planetary Physics, Clarendon Laboratory, Parks Road, Oxford OX1 3PU, United Kingdom

Agustín Sánchez-Lavega
Departamento de Física Aplicada, Universidad del Pais Vasco, Bilbao, Spain

Adam P. Showman
Department of Planetary Sciences and Lunar and Planetary Laboratory, University of Arizona, Tucson, AZ 85721

**Abstract**

Saturn inhabits a dynamical regime of rapidly rotating, internally heated atmospheres similar to Jupiter. Zonal winds have remained fairly steady since the time of Voyager except in the equatorial zone and slightly stronger winds occur at deeper levels. Eddies supply energy to the jets at a rate somewhat less than on Jupiter and mix potential vorticity near westward jets. Convective clouds exist preferentially in cyclonic shear regions as on Jupiter but also near jets, including major outbreaks near 35°S associated with Saturn electrostatic discharges, and in sporadic giant equatorial storms perhaps generated from frequent events at depth. The implied meridional circulation at and below the visible cloud tops consists of upwelling (downwelling) at cyclonic (anti-cyclonic) shear latitudes. Thermal winds decay upward above the clouds, implying a reversal of the circulation there. Warm-core vortices with associated cyclonic circulations exist at both poles, including surrounding thick high clouds at the south pole. Disequilibrium gas concentrations in the tropical upper troposphere imply rising motion there. The radiative-convective boundary and tropopause occur at higher pressure in the southern (summer) hemisphere due to greater penetration of solar heating there. A temperature "knee" of warm air below the tropopause, perhaps due to haze heating, is stronger in the summer hemisphere as well. Saturn's south polar stratosphere is warmer than predicted by radiative models and enhanced in ethane, suggesting subsidence-driven adiabatic warming there. Recent modeling advances suggest that shallow weather layer theories of jet pumping may be viable if water condensation is the source of energy input driving the flow, and that deep convective cylinder models with a sufficiently large tangent cylinder radius can reproduce observed flow features as well.

## 7.1 Introduction

### *7.1.1 Saturn's place among planetary atmospheres*

Surrounded by a family of exotic icy satellites, partially obscured by a complex set of rings, and pale compared to its sister giant planet Jupiter, Saturn's atmosphere has received less attention than most other celestial objects visited by the Cassini spacecraft. Nonetheless, over its four-year nominal mission, the Cassini Orbiter has acquired a wealth of information about Saturn's atmosphere that is unprecedented among the planets other than Earth. Cassini observations have confirmed some expected similarities between Saturn and the previously much better-observed Jupiter, and provided insights into some important differences as well. The goal of this chapter is to place our understanding of the thermal structure and dynamics of Saturn on the same footing as that of other planetary atmospheres, and to consider which aspects of that science are informed by our existing knowledge of Jupiter and Earth and which are unique to Saturn.

Atmospheric circulations generally exist primarily to transport heat from regions of excess to regions of deficit. Thus, the thermal structure and circulation are intertwined – temperature gradients created by diabatic heating drive specific types of circulations, and the resulting dynamical transport modifies the temperature field and sometimes induces secondary mechanically-driven circulations that may be thermodynamically indirect. Planet rotation and the vertical stratification imposed by the heating determine the "stiffness" of an atmosphere against latitudinal and vertical motions, respectively, and thereby control the extent to which poleward vs. upward dynamical heat transport dominates. To a first approximation this can be diagnosed from dimensionless parameters such as the Rossby and Richardson numbers, or alternatively, from the relative potential temperature contrasts in the vertical and horizontal over the characteristic scales of motion (Gierasch 1976; Allison et al. 1995).

By this reckoning, planets fall into three general classes. Terrestrial planets (Earth, Mars) have comparable vertical and horizontal contrasts and are dominated by baroclinic waves that transport heat both poleward and upward. Slowly rotating planets (Venus, Titan) have strong stratification but weak horizontal temperature gradients and are characterized by a planet-wide Hadley cell that efficiently transports heat poleward. Saturn's atmosphere is roughly similar to that of Jupiter in radius, depth, composition, rotation rate, albedo, and ratio of internal to external heating, and they are consequently thought to inhabit the same general dynamical regime (perhaps along with Neptune and Uranus), but one unique to the giant planets in several respects. The rapid rotation of the giant planets and the weak stratification imposed by their internal heat sources create vertical potential temperature contrasts that are less than horizontal contrasts, implying that the general circulation acts primarily to transport efficiently the internal heat upward to levels where it can easily be radiated to space. Furthermore, the giant planets' deep atmospheres allow for two very different possibilities for the dynamics. One picture assumes that large-scale convective organization of the flow driven solely by the internal heating extends through much of the depth of the atmosphere, while the other invokes a shallower upper "weather layer" that is largely decoupled from the deep convective interior by an intermediate stable layer and may respond to both solar heating from above and the convective heat flux at its lower boundary.

One major difference between Saturn and Jupiter is in their obliquities (26.7° vs. 3.1°, respectively). The greater seasonality of solar heating on Saturn thus suggests a more temporally variable atmospheric structure and dynamics in Saturn's upper troposphere and stratosphere. Observations of changes over Saturn's 29.5 year orbital period may therefore help distinguish aspects of the structure and circulation that are affected by insolation from those tied directly to the deep internal heating.

Compared to Earth, Saturn presents tremendous challenges for remote sensing. Saturn's surface area is two orders of magnitude greater than Earth's, making it impossible to observe the entire planet at once at spatial resolutions at which the relevant dynamical processes operate. Cassini remote sensing of Saturn thus combines global low-resolution mapping at long wavelengths by instruments with large fields of view when the orbiter is close to periapsis, and regional high-resolution image mosaics at shorter wavelengths by instruments with small fields of view at greater distances. Earth is partly cloud-covered and remote sensing thus sees the atmosphere from top to bottom, whereas Saturn is nearly overcast, precluding direct observations of the deep atmosphere that might differentiate deep from shallow circulation mechanisms. Earth is close to the Sun and thus

strongly forced, and its solid surface dissipates atmospheric kinetic energy. As a result the dynamical phenomena of interest are frequent and grow and decay on short time scales, so observations over a limited time period suffice to diagnose the processes that control its general circulation. Saturn, however, is far from the Sun, weakly forced, and has no solid surface to dissipate energy, so much of the circulation is invariant for long intervals, and the more transient features of the dynamics are very sporadic. Thus Cassini must observe Saturn for many years to detect changes and to sample the dynamics adequately. Unlike Earth, for which routine weather balloon launches provide "ground truth" for the interpretation of remote sensing, Saturn's troposphere and stratosphere have never been sampled *in situ* by probes. Even compared to Jupiter, Saturn's clouds exhibit much weaker feature contrasts in reflected sunlight and its colder temperatures imply less emission of thermal radiation. Thus, Saturn must be observed for longer time intervals than Jupiter for remote sensing to acquire the same amount of information.

Several previous review articles provide an excellent foundation for our discussion of the current understanding of Saturn's atmosphere. Ingersoll et al. (1984) summarize the knowledge of Saturn gleaned from ground-based observations and the Voyager flyby encounters of the early 1980s. Ingersoll et al.'s (2004) review focuses instead on the dynamics of Jupiter as understood at the conclusion of the Galileo mission, addressing many issues relevant to our discussion of Saturn as well. Finally, Sánchez-Lavega et al. (2004a) and Vasavada and Showman (2005) review dynamical theories for all the giant planets. A synthesis of the record of temporal changes in Saturn's atmosphere obtained by ground-based observers and the Hubble Space Telescope in the interim between Voyager and Cassini is presented in Chapter 3. We briefly summarize this recent history here to set the stage for our subsequent discussion of Cassini's contribution to our evolving view of Saturn.

### *7.1.2 Saturn science between the Voyager and Cassini epochs*

Following the Voyager 1 and 2 Saturn encounters, new dynamical data were obtained by employing ground-based telescopes and instrumentation of a new generation, in particular the Hubble Space Telescope (HST), which has operated since 1990. HST images improved on ground-based resolution of Saturn by a factor of ten, first using from 1990-1994 the Wide Field Planetary Camera 1 (WFPC1) and afterwards using the WFPC2 and optical correction system that improved considerably the resolution and image quality. The introduction in the mid-80's of the Charged Coupled Device (CCD) with its high sensitivity and image digitization allowed the use of a variety of narrow spectral filters (in particular those centered in methane absorption bands) that permitted probing of the clouds at different altitudes. Detection of discrete features from 1981-2005 was restricted to those with a high contrast and sizes > 1,000 km with ground-based telescopes or to sizes > 300 km with HST.

The most conspicuous dynamical phenomenon that occurred during this period was the rarely observed "Great White Spot" (GWS). Based on the apparent recurrence of the few available recorded cases during the last century, a prediction was made of the possibility that a GWS could erupt in the 1990's (Sánchez-Lavega and Battaner 1986; Sánchez-Lavega 1989). In September 1990 the outburst of a huge bright spot occurred at Saturn's equator, being the last and best studied GWS to date (Sánchez-Lavega et al. 1991; Beebe et al. 1992). The use of the CCD and the timing of the event a few months after the HST was placed in orbit, enabled HST to obtain the first high-resolution multi-wavelength images of the phenomenon (Barnet et al. 1992; Westphal et al. 1992). This allowed the cloud vertical structure to be determined from radiative transfer modeling (Sánchez-Lavega et al. 1994a; Acarreta and Sánchez-Lavega 1999), revealing the GWS to be a huge moist convective storm formed by cumulus-like cell clusters elevated above surrounding clouds (Sánchez-Lavega and Battaner 1986; Hueso and Sánchez-Lavega 2004; section 7.4.3). Bright cloud patches were observed in 1991-1992 as residuals of the 1990 GWS (Sánchez-Lavega et al. 1993a) until a second large equatorial storm erupted in 1994 (Sánchez-Lavega et al. 1996). The second half of the 1990's was dominated by the continuous formation and disappearance of bright spots in the equatorial region perhaps as residuals of deeper processes that produced the activity in 1990 and 1994 (Sánchez-Lavega et al. 1999).

A major advance in the study of Saturn's atmosphere was the determination at high spatial resolution of the meridional structure of the alternating pattern of zonal winds and in particular of the presence of a broad intense equatorial jet (peak velocity ~450 $ms^{-1}$) in the Voyager epoch (Ingersoll et al., 1984). This wind profile was re-measured and extended by Sánchez-Lavega et al. (2000). Another major discovery of the Voyagers was the observation of planetary scale waves in the upper cloud deck. A reanalysis of the images and the use of appropriate polar projections led to the discovery of the hexagonal wave, an

unusual feature embedded in a strong eastward jet (peak velocity 100 $ms^{-1}$) centered at 80ºN latitude (Godfrey 1988). The phenomenon was later modelled as a Rossby wave forced by a huge anticyclone, the North Polar Spot (NPS) located in one of the equatorward edges of the hexagon (Allison et al. 1990). The NPS and Hexagon were re-observed ten years later using ground-based CCD and HST imaging (Caldwell et al. 1993; Sánchez-Lavega et al. 1993b, 1997), confirming that both features are long-lived. However no hexagon-wave counterpart was observed around the South Pole in HST images (Sánchez-Lavega et al. 2002b). Another wave discovered by the Voyagers was called the "ribbon", a thin undulating band centered at latitude 47ºN in the peak of an eastward jet with velocity of 140 $ms^{-1}$ (Sromovsky et al. 1983). The phenomenon was interpreted as a baroclinically unstable wave with cyclonic and anticyclonic circulations on either side by Godfrey and Moore (1986). It was re-observed 14 years later in HST images (Sánchez-Lavega 2002a), suggesting again that it is a long lived feature.

The detection of planetary scale thermal waves in the upper troposphere (130-270 mbar) was reported by Achterberg and Flasar (1996) from the analysis of Voyager IRIS infrared spectra and interpreted as an equatorial Rossby wave (section 7.4.3). Long-term ground-based infrared observations of 7.8-μm and 12.2-μm stratospheric emission revealed a semiannual oscillation (14.8 years) in Saturn's low latitude stratospheric temperatures, suggesting a link to seasonal forcing (Orton et al. 2008; section 7.3.7.2). The response of Saturn's temperature to seasonally varying radiative forcing was calculated for the upper troposphere by Bézard et al. (1984) and for the stratosphere by Bézard and Gautier (1985). Comparison with the Voyager temperature measurements gave reasonable agreement in the altitude range from ~10 to 350 mbar. More advanced radiative-dynamical models were presented by Conrath et al. (1990), and including the seasonal variability in ring shadowing and ring thermal emission, by Barnet et al. (1992). Confirmation before the arrival of Cassini of the seasonal effects in the thermal structure of the stratosphere was obtained using ground-based mid-infrared imaging by Ollivier et al. (2000). Long-term changes, probably coupled to the seasonal insolation cycle, were also detected in the haze optical depth above the ammonia cloud deck from a 1967-1984 spectroscopic survey performed by Trafton (1985). This variability study was extended later from 1986 to 1989 by Karkoschka and Tomasko (1992) using ground-based data and from 1994 to 2003 by Pérez-Hoyos et al. (2005) and Karkoschka and Tomasko (2005) using HST images.

That Saturn possesses an active cloud structure below the ammonia cloud level was inferred from the detection of dark spots at different latitudes at a wavelength of 5 μm (Yanamandra-Fisher et al. 2001). The spots result from the effect of variability of the cloud opacity at the 2-4 bar pressure level on radiation coming from deeper levels. At visible wavelengths, a long-term HST-imaging survey of Saturn from 1994-2002 allowed the tracking of discrete spots and the detection of an apparent strong decrease in the equatorial jet speed while the jet profile at other latitudes remained constant (Sánchez-Lavega et al. 2003, 2004b). Similar results were obtained by the first multi-spectral Cassini wind measurements (Porco et al. 2005; Sánchez-Lavega et al 2007). The extent to which this variability represents real temporal dynamical changes versus variations in the level of seeing in the presence of vertical wind shear (Pérez-Hoyos and Sánchez-Lavega 2006) is discussed in section 7.3.5.

### *7.1.3 Questions about Saturn entering the Cassini era*

As Cassini approached the Saturn system in early 2004, a number of fundamental questions about Saturn's circulation and structure had been raised. Many of these concerned the series of alternating eastward and westward jets that Saturn has in common with Jupiter: What dynamical processes provide energy to the jets, and what is the nature of associated vertical overturning circulations? Is Saturn's apparent preference for prograde flow real or an artifact of uncertainty in its rotation rate? Given the stability of the jets at most latitudes over many decades, what is the first-order momentum balance between sources and sinks? To what depth do the jets extend, and does this tell us the relative importance of deep vs. shallow circulation mechanisms? Is Saturn's internal heating the control on its circulation, or does differential insolation also play a role? Does water moist convection and latent heat release create a stable layer at intermediate depths that decouples convective turbulence at depth from the dynamics of the cloud layer, or are convective storms merely a tracer of the large-scale dynamics?

Other questions concerned the role of the clouds and upper level hazes in both the dynamics and our ability to observe it and the transition from the flow at depth to the upper troposphere and stratosphere: Why are cloud albedo contrasts on Saturn more loosely related to the jets than on Jupiter? To what pressure do remote sensing observations "see" at levels where

cloud and haze opacity are non-negligible? Has Saturn's equatorial jet actually weakened? Are the observed equatorial variations, whether in wind speed or cloud altitude, a signature of seasonal insolation variations? How important is Saturn's tropospheric haze to the local heating, static stability, and upper troposphere dynamics? What is the upper tropospheric circulation associated with the decay of the jets with height, what processes explain it, and how does it connect to the deeper circulation? How does Saturn's stratospheric temperature distribution vary seasonally, and to what degree is it modified by the dynamics?

The Cassini Orbiter remote sensing instruments together cover a broad range of wavelengths and thus sense a wide range of altitudes to address these questions (sections 7.2.3 and 7.3.1). Most of the information presented in this chapter is the result of observations from the following instruments. The Composite Infrared Spectrometer (CIRS; Flasar et al. 2004) senses the stratosphere and upper troposphere down to the visible cloud level at thermal infrared wavelengths. The Imaging Science Subsystem (ISS; Porco et al. 2004) provides high-resolution images of several levels within the ammonia clouds and tropospheric haze from the near ultraviolet to the near-infrared. The Cassini RADAR passive radiometry mode (Elachi et al. 2004) measures microwave emission from near the ammonia saturation level. The Visual and Infrared Mapping Spectrometer (VIMS; Brown et al. 2004) operates in both visible and infrared wavelength ranges to observe reflected sunlight and thermal emission, sometimes from relatively deep within the ammonium hydrosulfide cloud layer.

### *7.1.4 Scope and organization of the chapter*

This chapter considers all aspects of the thermal structure and dynamics of Saturn's atmosphere. Our lower boundary is the ~1-2 Mbar pressure of the molecular-metallic hydrogen transition (Guillot 1999; Hubbard et al., Chapter 5), below which Saturn's rotation rate is determined; this is the lower boundary for deep convective cylinder models. Our upper boundary is at a few μbar, above which non-neutral species and magnetospheric interactions become important (Nagy et al., Chapter 9; Mitchell et al., Chapter 11). Saturn's gases, aerosols and clouds determine the level we observe and act as tracers of vertical motions that cannot be directly observed; these are discussed in more detail in Chapters 6 (Fouchet et al.) and 8 (West et al.). Our discussion is organized as follows. Observational inferences about the atmosphere below the visible cloud tops and its relevance to processes at higher levels are described in Section 7.2. Global aspects of the more extensively observed visible cloud level, upper troposphere and stratosphere are considered in Section 7.3. Section 7.4 describes discrete and regional phenomena, with an emphasis on what they imply about physical processes and unobserved aspects of the atmosphere. In Section 7.5 we assess competing ideas about the maintenance of Saturn's general circulation, inferences about these mechanisms from recent modeling studies, and the extent to which observations constrain these theories. Finally, in Section 7.6 we consider the major remaining outstanding questions about Saturn structure and dynamics, how some of these may be addressed by observations taken during the Cassini Equinox and Solstice mission phases, potential avenues for modeling advances in the next few years, and long-term observational needs that might help define a future follow-on Saturn mission.

## 7.2 Observational inferences about the deep atmosphere

### *7.2.1 Saturn's rotation period*

On gas giant planets, the actual rotation period of the deep interior cannot be determined directly. Jupiter's magnetic field is tilted and thus modulates radio emissions with a periodicity that is interpreted as being representative of the interior rotation. On Saturn, however, the tilt is very small and the magnetic field nearly symmetric (see Chapter 11). Nonetheless, Voyager radio measurements detected Saturn Kilometric Radiation (SKR) that was variable but modulated at a period of 10 hr, 39 min, 24 s (Desch and Kaiser 1981). This has been used ever since as the reference frame for measuring winds on Saturn.

Cloud-tracked winds based on the SKR period behave quite unlike those observed for Jupiter (Smith et al. 1982). Both planets have a strong prograde equatorial jet and a series of weaker alternating prograde and retrograde jets at higher latitudes. On Saturn, though, the equatorial jet is extremely strong and the westward jets either very weak or merely eastward minima (section 7.3.3). The strong equatorial jet, if confined to a shallow weather layer, would require equator-pole geopotential height differences of 40% relative to the thickness of the weather layer, which is inconsistent with the small observed equator-pole temperature difference at cloud top. This led Smith et al. (1982) to conclude that the level of no motion must be quite deep, of order $10^4$ bars, although they noted that if the true rotation period were ~ 8 minutes shorter the requirement for deep flow would disappear. Allison and Stone (1983) argued that thin weather layer configurations would still be viable if a significant latitudinal temperature gradient, associated with a latitudinally varying level of no motion somewhat analogous to Earth's oceanic thermocline, existed below cloud level. They suggested that the buoyancy contrasts required by such a structure might be provided by latitudinally varying latent heat release if the water abundance on Saturn were sufficiently in excess of solar.

Ulysses and Cassini observations, however, indicate that the SKR modulation period varies by ~1% on time scales of years and is now ~8 minutes *longer* than the Voyager SKR-based reference period (Galopeau and Lecacheux 2000; Gurnett et al. 2005; Kurth et al. 2007, 2008). These variations are considerably greater than any possible real variation in the rotation period of Saturn's massive interior. Instead the SKR period is now thought to reflect magnetospheric slippage from a centrifugally driven convective instability, associated with mass loading from the Enceladus neutral gas torus (Gurnett et al. 2007).

This leaves the actual Saturn deep interior rotation period unknown – a considerable obstacle to interpretations of its atmospheric dynamics. Anderson and Schubert (2007) returned to the original idea of a shorter period. They calculated a reference geoid from Saturn gravitational data and then estimated the rotation period that would minimize the dynamical height deviations of the 100 mbar surface from that geoid; the resulting rotation period is 10 hr, 32 min, 35 s. Figure 7.1 shows that use of this period as a reference reduces Saturn's equatorial jet by ~100 m $s^{-1}$ and produces alternating eastward and westward jets of comparable magnitude at higher latitudes. Both features make the Saturn wind profile much more like that of Jupiter.

The difficulty with the Anderson and Schubert (2007) result is that there is no physical requirement for the flow to minimize dynamic height deviations from the geoid. Physical arguments can be marshaled both for and against this being the true rotation period of Saturn. Although the Voyager SKR-based period creates a seemingly unrealistically strong equatorial jet (~450 m $s^{-1}$), this must be placed in the context of Saturn's size and (apparently) rapid rotation. The ratio of this wind speed to the tangential speed of a point at Saturn's cloud level rotating with the planet (in effect an equatorial Rossby number) is only ~.04. This is somewhat larger than the terrestrial value of ~.01, but considerably smaller than the value of ~50 for slowly rotating Venus. Furthermore, there is no fundamental reason to rule out global superrotation at the Saturn visible cloud level. Aurnou and Heimpel (2004), for example, show that a no-slip lower boundary condition applied in a deep convective cylinder simulation of Saturn produces a wind profile quite like that obtained from the data using the Voyager SKR period.

On the other hand, if such a lower boundary condition is relevant to Saturn, the conundrum simply shifts to deeper levels: What would the physical source of friction at the lower boundary be on Saturn, and why would a similar behavior at depth not be applicable to Jupiter, which does not show nearly as strong a preference for prograde flow? Use of something closer to the shorter Anderson and Schubert (2007) period removes this discrepancy and leaves shallow weather layer models of the cloud level dynamics in play. Possibly more compelling are two recent pieces of observational evidence. Kurth et al. (2008) report a second shorter SKR modulation period of 10.59 hr, tantalizingly close to the various alternative rotation periods considered by Smith et al. (1982), Allison and Stone (1983), and Anderson and Schubert (2007), although this period too appears to be variable. Another intriguing result comes from potential vorticity analysis of Saturn's upper troposphere winds and temperatures (Read et al. 2009; section 7.3.8), which suggests that the wind field measured in a reference frame based on a shorter rotation period might be close to neutrally stable, a desirable result given the constancy of most of Saturn's jets over long time intervals. Since the issue is not settled, we continue to report winds based on the Voyager SKR period in this chapter and await a possible resolution if highly inclined orbits in Cassini's extended mission allow the magnetic field of Saturn to be documented with greater accuracy (Bagenal 2007).

### *7.2.2 Convective heat flux and condensation levels*

Saturn is estimated to emit 1.78 ± 0.09 times more longwave radiation than the shortwave radiation that it absorbs (Hanel et al. 1983). This implies the existence of a 2.01 ± 0.14 W $m^{-2}$ internal heat source due to both gravitational contraction and helium differentiation (see Chapter 5). The molecular envelope is poorly conducting, and opacity due to hydrogen, helium, and several minor constituents becomes substantial at depth. Thus it has long been anticipated that Saturn's interior is convective and its lapse rate close to dry adiabatic. Ingersoll and Porco (1978) concluded that convection could transport sufficient heat poleward along sloping surfaces with very small temperature gradients to offset the latitudinal gradient of insolation and explain the small equator-pole temperature contrasts observed on the giant planets (Ingersoll 1976).

A possible difficulty with this picture was raised by Guillot et al. (1994a), who pointed out that at temperatures of ~1200-1500 K, photon emission shifts to shorter wavelengths as temperature increases, and that the resulting opacity due to hydrogen and helium absorption might decrease, creating a stable radiative zone. Gierasch (1999) showed that the existence of a radiative zone could have significant consequences for latitudinal temperature gradients at higher altitudes and might explain Saturn's preference for prograde winds in the Voyager SKR reference frame (section 7.2.1). However, the presence of wide sodium and potassium absorption lines in spectra of brown dwarfs has led Guillot (2005) to conclude that transparent regions of the spectrum are most likely not present and therefore that a deep radiative zone is unlikely on the gas giants. Thus gases are assumed to be well-mixed in the molecular envelope until reaching their condensation levels.

Thermo-chemical equilibrium models predict that Jupiter and Saturn have three main cloud decks in the upper troposphere. For Saturn they are: an upper ammonia ($NH_3$) ice crystal layer centered at ~1 bar, an ammonium hydrosulfide layer ($NH_4SH$) centered at ~3-4 bar, and a water layer centered at ~8-10 bar (Weidenschilling and Lewis 1973). The actual locations are uncertain because of the unknown abundances of the condensing constituents (see Chapter 6). These results have often been interpreted as implying the existence of extensive cloud decks of each species, but the terrestrial experience of a partly cloud covered planet hints at more complexity. Carlson et al. (1988) examined cloud microphysics on the giant planets. They concluded that the $NH_3$ and $NH_4SH$ decks on Saturn were relatively thin, only lightly precipitating, and thus the equivalent of cirrus clouds on Earth. The water cloud is more massive, however, even for solar abundance, and is more likely to be convective and sporadic with small areal coverage. Del Genio and McGrattan (1990) used a cumulus parameterization to show that water-based moist convection would occur on the giant planets and create a stable layer over a depth of about a scale height above the water condensation level via the combined effects of latent heat release, compensating subsidence, and molecular weight gradients. This putative stable layer is too deep to have been observed but is crucial to many shallow weather layer theories of giant planet circulations (section 7.5). Beyond the first scale height above the water condensation level, the lapse rate is assumed to once again become dry adiabatic because the other condensate species release too little latent heat to have a significant effect. Above the 1 bar level dry adiabatic lapse rates have been retrieved from Voyager occultations (Lindal et al. 1985) and Cassini CIRS (Fletcher et al., 2007b), with a transition to a stable temperature gradient occurring at ~400-500 mbar.

### *7.2.3 Cassini probing of the atmosphere below cloud top*

Cassini does not directly sense the Saturn atmosphere at or below the water cloud level. However, Cassini VIMS and RADAR provide the first detailed global views of the depths of Saturn underneath the upper-level hazes and ammonia cloud tops. Each does this in modes somewhat atypical to the usual near-infrared and radar means of exploring planets.

VIMS uses wavelengths beyond 4.5 μm to image the planet bathed from within by its own thermal emission, as has been done for Venus (Baines et al 2006; Drossart et al. 2007; Piccioni et al. 2007). In the 5 μm spectral region, the primary sources of extinction are spectrally-localized molecular absorption by trace gases (e.g., phosphine, germane, ammonia) and the extinction of deep clouds comprised of large particles with radii near or larger than 5-μm. The extensive upper level haze (section 7.3.2) does produce significant scattering of sunlight. This, together with the weak solar flux there - just 0.2 % of the visible near 0.5 μm - inhibits sunlit views of these deep large-particle clouds. However, a second source of radiation is available to probe the ammonia-cloud region and below: Saturn's own indigenous heat radiation. Thus deep clouds and their motions

are detected by observing their silhouettes against the background glow. For Saturn, the 5-μm signal is produced near the 6.5-bar, 245-K level and attenuated primarily by overlying large-particle clouds. Thus, relatively dark regions depict thick large-particle clouds, while relatively bright regions depict relatively cloud-free areas. The spectrum near 4.65 μm and 5.1 μm can be used to determine the cloud base pressure level for clouds located deeper than 1.8 bar, below the ammonia condensation level (Baines et al. 2009a). This technique reveals that a deep cloud layer exists with base pressure varying between ~ 2.5 and 4.5 bars, depending on location, corresponding to that thermochemically predicted for a cloud comprised of $NH_4SH$.

RADAR, in its passive "listening" mode, views the thermal emission of Saturn as well, but at an effective wavelength of 2.2 cm, which is unaffected by haze and cloud particles but is sensitive to ammonia gas absorption, an important cloud-forming condensable. This longer wavelength has one particular drawback: the instantaneous field-of-view is an order of magnitude larger than for VIMS (~ 6 mrad vs. 0.5 mrad), despite the larger telescope (in this case, the spacecraft's 4-meter telecommunications antenna). Thus, useful maps (IFOV better than 2000 km) are only acquired within ~ 330,000 km above the planet, which occurs only during the 12 hours around periapse on the closest orbits.

VIMS and RADAR have revealed an unexpectedly different world at levels underneath the hazes of Saturn. Figure 7.2 compares the VIMS view of Saturn in reflected sunlight at 0.9 μm, a methane absorption band that senses the upper troposphere haze, to that at 5 μm (Baines et al. 2009c). At 0.9 μm several broad bands of hazes circle the planet, with little longitudinal variability and relatively little contrast between adjacent bands. The equatorial region sports a broad band of unusually high and thick haze reaching into the stratosphere. In contrast, the lower tropospheric view at 5 μm reveals a dense array of narrow bands – cloudy "zones" and less cloudy "belts". Many of the zonal bands are broken up by discrete cloud features.

Figure 7.3 compares RADAR (Janssen et al. 2008) and VIMS global cylindrical mosaics of Saturn acquired within one day of each other. Two common features of dynamical significance are evident. Outside the equatorial region, both images exhibit a tendency for cloud bands to organize on a scale of ~1.8° latitude, a behavior not observed at cloud top in reflected sunlight. The source of this fine-scale structure is unknown. The primary difference between the $NH_4SH$ and $NH_3$ cloud level atmosphere sensed by VIMS and RADAR, and the visible cloud top level sensed by ISS (section 7.3.2), is static stability. ISS images view the transition region between the stable upper troposphere and near-adiabatic lower troposphere (Fletcher et al., 2007b), while VIMS and RADAR sense the near-adiabatic region, above any stable layer below associated with water condensation. The Rossby deformation radius $L_d = NH/f$, where $N$ is the Brunt-Väisälä frequency, $H$ the scale height, and $f$ the Coriolis parameter, is a characteristic scale at which Coriolis forces effectively counter pressure gradient forces and at which instabilities inject energy into the flow. Since $L_d$ decreases as static stability decreases, these views of the deeper atmosphere might reveal something more directly about the forcing of the cloud-top dynamics, which is almost certainly driven by processes operating at or below the water cloud level. Near the equator, exceptionally large discrete clouds exist near 6°N and 6°S latitude. These clouds are likely associated with enhancements of ammonia gas observed by RADAR, and may be ammonia plumes delivering aerosols to the upper atmosphere, thereby producing the band of enhanced upper-level aerosols observed there. Since these features appear to correspond to similar scale cloudy features in the VIMS image, which senses deeper than RADAR, both features may be produced by water convection triggered at deeper levels.

## 7.3 Observations at and above the visible cloud top

### *7.3.1 Levels sensed by Cassini instruments from cloud top to the stratosphere*

Cassini remote sensing exploits the wavelength-dependent scattering and absorption properties of gases and particulates to sense temperatures and dynamics at different pressure levels (see Chapter 8). In reflected sunlight we "see" down to a level not much greater than that for which the two-way extinction optical thickness ($\tau$) is ~1-2. Rayleigh scattering by the gaseous $H_2$-He Saturn atmosphere varies approximately as $\lambda^{-4}$, where $\lambda$ is the wavelength of the observation. Particulates

(aerosols and clouds) scatter more efficiently than gases and with a weaker ($\sim\lambda^{-1}$) dependence. Thus, in the presence of aerosols or clouds, we generally see down to the particulate scattering $\tau = 1$ level at non-absorbing (continuum) wavelengths, which is usually close to the highest cloud top. Clouds are almost conservative scatterers in the shortwave band and appear bright in continuum images, more so the more optically thick they are. Aerosol hazes (section 7.3.2) can be either absorbing or scattering at different wavelengths and thus may appear either dark or bright in different filters. At wavelengths centered on gaseous absorption bands (usually of methane), we see no deeper than the absorption two-way $\tau = 1$ level in clear regions. In cloudy or optically thick aerosol regions, if the cloud/aerosol top is above the gas $\tau = 1$ level, absorption by the overlying gas is reduced and scattering from near the cloud/aerosol top takes place. This allows us to discriminate cloud/aerosol top heights – the brighter the feature, the higher the cloud top.

In the ultraviolet (UV), ISS would only see to ~500-1000 mbar if the atmosphere were clear, and in practice, ubiquitous stratospheric aerosols (section 7.3.2) are sensed at these wavelengths. Most ISS imaging is done at near-infrared wavelengths (Fig. 7.4), where scattering by small aerosol particles is reduced and deeper cloud layers are easier to see. However, unlike Jupiter, Saturn has a relatively thick upper tropospheric haze (section 7.3.2) that limits our ability to see to depth, and thus feature contrasts are more muted on Saturn than on Jupiter. Nonetheless, in the continuum filter CB2 (750 nm) we can see features attributed to reflection by optically thick clouds with a variety of cloud top altitudes within and below the haze. ISS contains three methane band filters, at wavelengths of weak (MT1, 619 nm), moderate (MT2, 727 nm), and strong (MT3, 889 nm) absorption. The clear-sky $\tau = 1$ level for MT3 is ~330 mb (Tomasko et al. 1984), above the ammonia cloud top, and it thus sees only variations in haze. MT2 penetrates to ~1.2 bars in clear sky and thus sees haze, some ammonia cloud tops and occasional high-penetrating convective water clouds. MT1 is sensitive to even deeper levels. Figure 7.4 (upper left) shows that CB2 gives the most detailed view of the ammonia cloud tops. MT1 (upper right) sees most but not all of the same clouds as are visible in the continuum filter, but the sizes of discrete features are smaller, suggesting either that the weak methane absorption prevents seeing of optically thinner cloud edges or that the clouds decrease in size upward. The MT2 image (lower right) is very different from the others – no small discrete cloud features are visible, though there are numerous striated features that appear to be correlated with those visible at the other wavelengths. Much of what we see in MT2 appears to be due to variations in the tropospheric haze instead. During the Cassini epoch, CB2 images of the Southern Hemisphere (lower left) generally have much less contrast than those of the Northern Hemisphere, suggesting that the haze optical thickness is lower in the winter hemisphere (see Chapter 8). This is consistent with inferences about local haze heating from the upper troposphere thermal structure (section 7.3.6) and greater Northern Hemisphere emission variability at 5 μm in VIMS images (Fig. 7.2).

In the mid- and far-infrared ($\lambda > \sim 7\mu m$), reflected sunlight can be ignored, and the observed radiation is due entirely to thermal emission. If the vertical distribution of absorption is known, spectra can be inverted to determine a vertical temperature profile. Conversely, if the temperature is known, abundances of absorbers can be determined. In practice, temperatures can be retrieved from two regions of the spectrum. The $\nu_4$ rovibrational band of methane, at ~1200 to 1400 $cm^{-1}$, provides information on mid-stratospheric temperatures between ~0.5 and 4 mbar in nadir-viewing mode and up to a few μbar in limb-viewing mode. The S(1) and S(0) collision-induced rotational lines, plus part of the translational continuum, from 220 to 670 $cm^{-1}$, provide information on temperatures in the upper troposphere and tropopause regions, between ~50 and 800 mbar. The collision-induced hydrogen absorption is also sensitive to the ratio of *ortho*-hydrogen to *para*-hydrogen. At temperatures less than 300K, the equilibrium *para* to *ortho* ratio varies with temperature, and the expected equilibration timescales are comparable to or longer than the dynamical timescales (Massie and Hunten 1982; Conrath and Gierasch 1984). The *para*-hydrogen abundance can thus be used as a diagnostic of vertical motions in the troposphere. Thermal infrared spectra can also be used to retrieve abundances of several trace gaseous species that are useful tracers of the circulation. Two regions of the spectra, from about 20 to 200 $cm^{-1}$ and from about 900 to 1200 $cm^{-1}$, can be used to measure the tropospheric abundances of ammonia ($NH_3$) and phosphine ($PH_3$) at pressures around 500 mbar. Both species are transported upwards from reservoirs in the interior, and destroyed in the upper troposphere by photodissociation ($NH_3$ is also lost through condensation); their abundances are thus affected by vertical mixing and transport by the meridional circulation. Between 650 and 850 $cm^{-1}$, the spectrum contains stratospheric emission lines of several hydrocarbons, in particular acetylene and ethane, which can be used to measure their abundances in the middle stratosphere. These hydrocarbons have photochemical lifetimes comparable to or longer than the dynamical timescales of the meridional circulation. Thus, their distributions can be used to infer information about the meridional circulation in the stratosphere.

### *7.3.2 Albedo patterns vs. jets on Saturn vs. Jupiter*

HST and Cassini reflectivity measurements from the near-UV (200 nm) to the near-infrared (3 μm), including the 619, 725 and 890 nm and 2.3 μm methane absorption bands, indicate that at least two haze layers of aerosol particles permanently exist above the ammonia cloud (see Chapter 8). An upper thin haze in the stratosphere (between pressure levels 1-50 mbar) is formed by small particles strongly absorbent in the UV (radii ~ 0.2 μm, optical depth $\tau \sim 1$). Beneath it a thicker haze extending from the ammonia cloud to the tropopause level shows a temporally variable optical depth (typically $\tau \sim 10$ at 814 nm with a variability of a factor ~ 2). Saturn's banded appearance at visible wavelengths, extending along parallels, results mostly from the combined effect of scattering and absorption of solar photons (350-800 nm) by these hazes (Karkoschka and Tomasko 1991, 2005). In the UV ISS filters the planet appears more homogeneous due to absorption and scattering of solar photons by the upper haze and gaseous atmosphere, but the latitudinal contrast between dark and bright bands is slightly greater (Vasavada et al. 2006). In the near IR filters banding is less pronounced in the continuum but becomes more evident in the deep methane absorption bands MT2 and MT3 (Vasavada et al. 2006) and at 2.3 μm where bright bands, a signature of high altitude hazes, detach at the equator and in temperate latitudes. In the thermal infrared window (4-5 μm), radiation escaping from the interior allows us to see distinct features produced by opacity variability in the $NH_3$ - $NH_4SH$ cloud system and perhaps in water clouds as well, and zonally aligned features occur (Yanamandra-Fisher et al. 2001; Baines et al. 2005; section 7.2.3).

The meridional distribution of Saturn's cloud/haze bands is related to the zonal wind profile of alternating eastward and westward jets (Karkoschka and Tomasko 1991, 2005) but is quite different from that on Jupiter in several ways:

(1) In visible and near-infrared continuum images, Jupiter's bright bands (zones) reside in the anti-cyclonic shear regions that lie equatorward of the eastward jets and its darker bands (belts) in the cyclonic shear regions poleward of these jets (Smith et al. 1979). The belts and zones are of comparable (~5°) width. A different relationship occurs on Saturn (Smith et al. 1981; Vasavada et al. 2006): Eastward jets occupy narrow dark regions, often bisected by a thin bright band, while the much broader region between successive eastward jets and including the westward jets tends to be brighter (Fig. 7.5). The eastward jet morphology resembles that seen in VIMS nighttime 5 μm thermal emission (Fig. 7.2) but that elsewhere does not.

(2) The morphology of the bands also differs on the two planets. Bright zones on Jupiter tend to have lower feature contrast than the darker belts. On Saturn, the dark bands associated with the eastward jets are generally low in contrast with mostly linear features, while the broad brighter regions show considerable evidence of turbulent, cellular, discrete features.

(3) While the jet profile is stable in its latitudinal location on Saturn (Smith et al. 1981; Sánchez-Lavega et al. 2000, 2003; Vasavada et al. 2006), the cloud/haze bands change their brightness and edge positions on time scales of both years (Sánchez-Lavega et al. 1993a; Pérez-Hoyos et al. 2005; Karkoschka and Tomasko 2005) and months (Sánchez-Lavega et al. 1993a; Pérez-Hoyos et al. 2006). The brightness changes are wavelength dependent. A band can remain stable in brightness in one wavelength range but brighten or darken with time at others.

A long-term comparison between Voyager, Hubble and Cassini images in haze-sensitive methane band images suggests that on average, the albedo banding takes on distinct characters in the equatorial region (20ºN to 20ºS), the temperate region (20º to 55º in each hemisphere) and the polar area (55º to the pole in each hemisphere). The broad and intense equatorial jet correlates with an Equatorial Zone that is bright at 890 nm (due to high dense hazes) but dark in the UV (due to UV-blue absorption by this haze). The thick and vertically extended tropospheric haze contains discrete features moving at different altitude levels between 50 and 700 mbar (Pérez-Hoyos and Sánchez-Lavega 2006). Outside the equatorial region, the albedo pattern at 890 nm is well correlated with the eastward jets and the temperature field at 500 mbar (Fletcher et al. 2007a,b): equatorward of the eastward jet peak the haze is bright (high and dense) and the temperatures low, with the contrary occurring on the poleward side (dark band and high temperatures). This suggests that in the upper troposphere and lower stratosphere, ascending motions occur on the equatorward side of the jet peak whereas descending motions occur on the poleward side accompanied by adiabatic cooling and warming, in good agreement with results obtained from the Voyagers (Conrath and Pirraglia 1983). This stands in contrast to the tropospheric continuum cloud top level, where the inferred pattern of rising and sinking motions is just the opposite (Del Genio et al. 2007a) and not obviously related to the albedo pattern (see section 7.4.2).

### *7.3.3 Cloud level winds and dynamical fluxes*

The early Voyager image measurements (Smith et al. 1981, 1982, later reworked by Ingersoll et al. 1984) obtained up to 1000 velocity vectors from cloud tracers and showed a roughly symmetric pattern of eastward zonal jets about the equator, with strong eastward motion at speeds of more than 450 m $s^{-1}$ (relative to System III) in an equatorial jet, extending to nearly 30° latitude north and south of the equator. At higher latitudes, 4-5 additional eastward jets are found (including a 'shoulder' on the flanks of the equatorial jet at ±30°) between 30° and 80° latitude, with velocities ranging from 60-160 m $s^{-1}$. As mentioned earlier, the cloud-tracked zonal velocity profile on Saturn exhibits a near-absence of westward jets, with the flow between the eastward jets staying close to zero in System III (Fig. 7.1). Such a pattern is quite unlike the corresponding profile on Jupiter, for which mid-latitude eastward and westward jets are of comparable strength relative to System III. This has raised doubts over the robustness of Saturn's System III, as derived from measurements of SKR emissions, which have been further reinforced by the indication from Cassini that the rotation of the SKR reference frame is not constant in time (section 7.2.1).

More recent measurements have included a detailed study of the high latitude jets around 64°-84°N by Godfrey (1988) and a more extensive analysis of Voyager images by Sanchez-Lavega (2000), which included ~2000 vectors covering latitudes 81°N – 71°S with improved error analysis, together with comparisons with measurements taken during the 1990s using HST images. Processing of Cassini ISS images is continuing at the time of writing, and so far has led to published profiles in the southern hemisphere by Porco et al. (2005), Vasavada et al. (2006) and Sanchez-Lavega et al. (2006). A combined profile from all of these data is shown in Figure 7.6a. The new data from Cassini show few changes from the earlier Voyager measurements, though do confirm the existence of additional eastward jets at 74.5°S and 88°S. The latter represents the edge of the polar vortex over the south pole, with zonal wind speeds of more than 160 m $s^{-1}$, in association with the polar hot-spot found in both ground-based infrared images and from Cassini CIRS (Fletcher et al. 2007b).

Zonal winds at the ammonium hydrosulfide cloud level have also been estimated by tracking features in VIMS 5 μm images (Baines et al. 2005, 2009a; Choi et al. 2009). These profiles (Fig. 7.7) are quite similar to those at the visible cloud level during the Voyager encounter, but suggest slightly higher jet speeds at the deeper level sensed by VIMS. Above the visible cloud level CIRS thermal winds indicate a further decay of the jets with height (section 7.3.4), although tracking of features in methane band images suggests that the shear in eastward jets exceeds that in westward jets (García-Melendo et al., 2009).

It is notable that the shapes of the various eastward and westward jets take on particular characteristics that may have some dynamical significance. The equatorial jet appears to have a complex shape with either a relatively flat peak or even some tendency towards a double-peaked form with a local minimum of $u$ on the equator itself. At higher latitudes, the eastward jets are typically much sharper and narrower than the corresponding westward jets or minima in $\bar{u}$. Such a trend is consistent with a tendency for the flow to adopt a relatively weak latitudinal gradient of absolute vorticity $\zeta = f + \xi$ (where $\xi$ is the relative vorticity) in westward flow, while the gradient is enhanced in association with eastward jets. In practice, however, like on Jupiter, the northward gradient, $d\zeta/dy$ (Fig. 7.6b), is found to reverse in sign around many of the westward jets, such that $\beta - d\xi/dy$ changes sign several times between equator and pole in each hemisphere (where $\beta$ is the planetary vorticity gradient $df/dy$). Such reversals of $d\zeta/dy$ would, at face value, suggest the possibility of barotropic instability, though the role of baroclinic effects should also be taken into account (see Section 7.3.8).

The processes maintaining this pattern of jets continues to excite controversy, though some indication of the possible role of eddy momentum transports is starting to become apparent from measurements of the non-zonal components of velocity from more detailed cloud-tracking. Early attempts to measure the horizontal transport of momentum via 'eddy correlation' techniques on both Jupiter and Saturn (Ingersoll et al. 1981, 1984; Mitchell and Maxworthy 1985) claimed to find quite strong correlations between $\overline{u'v'}$ and $d\bar{u}/dy$, suggesting a significant conversion of eddy into zonal mean kinetic energy. Sromovsky et al. (1982, 1983), however, suggested that these initial results may have been affected by possible selection effects, which tended to over-emphasize contributions to $\overline{u'v'}$ from bright or active cloud features. The use of relatively small numbers of vectors (< 1000) in the statistics may also have prejudiced the ability to detect a statistically significant correlation.

Recent attempts to measure this conversion from eddy to zonal mean flow (Salyk et al. 2006; Del Genio et al. 2007a) have made use of automated image correlation techniques from Cassini ISS images. Such methods enable many more cloud vectors to be measured, and appear to be much less affected by visual selection effects of cloud targets, thereby achieving a more uniform and representative sampling of velocity structures across the planet. Results indicate a reasonably clear and robust positive global correlation between $\overline{u'v'}$ and $d\bar{u}/dy$, accelerating the jet with implied mean energy conversion rates from eddies to the zonal flow of ~7.1-12.3 x $10^{-5}$ W $kg^{-1}$ for Jupiter (Salyk et al. 2006) and ~3.3 x $10^{-5}$ W $kg^{-1}$ for Saturn (Del Genio et al. 2007a). Such a correlation is broadly consistent with the notion of an anisotropic upscale turbulent cascade in a geostrophically turbulent flow (e.g. Vasavada and Showman 2005; Galperin et al. 2006; section 7.5). However, this phenomenon needs more detailed analysis, particularly with regard to the roles of different scales. Mitchell and Maxworthy (1985), for example, noted that the correlation between $\overline{u'v'}$ and $d\bar{u}/dy$ near Jupiter's Great Red Spot was significantly *negative*, implying a conversion of kinetic energy *from* the zonal flow *into* the GRS. Such a result might indicate different mechanisms for the production and maintenance of different types of eddy, with small-scale features emerging from active upwelling convection or baroclinic instability while larger eddies are sustained (at least in part) by barotropic exchanges with the zonal jets.

### *7.3.4 Thermal structure and circulation above cloud level*

Information on temperatures in Saturn's upper troposphere and stratosphere comes from two primary sources. Radio occultations provide vertical temperature profiles with high vertical resolution, but at a limited number of locations. Thermal infrared sounding provides extensive spatial coverage, but the vertical resolution is limited to roughly one scale height.

The earliest spatially resolved thermal observations of Saturn, using north-south scans at 12μm in the $\nu_9$ band of ethane during southern summer, showed an increase in emission from north to south with a strong peak in the emission at the south pole (Gillet and Orton, 1975; Rieke, 1975). However, these observations did not have the information needed to determine if the spatial variations in emission were caused by variations in the temperature or ethane profiles. Later observations by Tokunaga et al. (1978) found similar north to south variations in emission from the $\nu_4$ band of methane at 7.8μm, indicating that there were stratospheric temperature variations, with the south (summer) pole warmer than the equator. Tokunaga et al. (1978) also observed near 20 μm, in the upper tropospheric hydrogen band, and found that the meridional emission variations were weaker than in the stratospheric emission bands, indicating that the equator-to-pole temperature gradients were smaller near the tropopause than in the stratosphere.

The first spacecraft observations of Saturn's thermal structure came from Pioneer 11 in 1979. Measurements at 20 and 45μm by the infrared radiometer were inverted by Orton and Ingersoll (1980) to give temperatures from ~60 to 500 mbar from 30°S to 10°N. They found a temperature minimum at the equator, which became weaker with increasing pressure, with no meridional gradient between 10°S and 30°S. More extensive thermal data was obtained by the infrared spectrometer IRIS on Voyagers 1 and 2. Conrath and Pirraglia (1983) used Voyager IRIS data to obtain meridional temperature profiles at three pressure levels in the upper troposphere just after northern spring equinox. At 150 mbar, they found a hemispheric asymmetry, with the north pole ~5K colder than the equator, but no large-scale gradient in the south. Superimposed on the large-scale gradients were smaller variations of ~2K which are correlated with the zonal jets. The temperature variations become weaker with depth, disappearing by 700 mbar where the temperature is uniform with latitude except for a warm region near 30°N.

Ground-based maps of emission from stratospheric ethane and methane bands during early northern summer by Gezari et al. (1989) showed emission increasing from the equator to the north (summer) pole, as well as a narrow band of enhanced emission at the equator, but they did not attempt to retrieve temperatures from their data. Later, Ollivier et al. (2000) imaged Saturn in several stratospheric and tropospheric bands during late northern summer. They also saw enhanced emission at north polar latitudes in the stratosphere, but not in the troposphere. Greathouse et al. (2005) used high spectral resolution observations in the methane $\nu_4$ band to retrieve stratospheric temperatures at southern summer solstice. They found a general equator-to-south-pole temperature gradient, with the south pole ~10K warmer than the equator and the gradient slightly stronger at lower pressures. Orton and Yanamandra-Fisher (2005) made high spatial resolution thermal infrared images of

Saturn in the stratospheric methane and upper tropospheric hydrogen bands during early southern summer, allowing them to determine temperatures at 3 mbar and 100 mbar. The 3 mbar stratospheric temperatures show a ~15K temperature gradient from the equator to the south pole, with a sharp temperature increase at 70°S. The tropospheric temperatures show variations of ~3 K on the scale of the zonal jets, with no clear equator to pole gradient. They also found a hot spot at the pole, with a sharp 2.5 K temperature increase between 87°S and the pole (section 7.4.5).

Cross-sections of southern hemispheric temperatures from Cassini CIRS data were presented by Flasar et al. (2005). Temperatures from CIRS mapping observations were retrieved by Fletcher et al. (2007b), giving a latitude-pressure cross section of temperatures in the upper troposphere and middle stratosphere during southern mid-summer (Figure 7.8). There is a well-defined tropopause at ~80 mbar, separating a strongly statically stable stratosphere with temperatures increasing with altitude, from a troposphere with temperatures increasing with depth. In the upper troposphere, the temperature gradient increases with depth down to approximately 400-500 mbar, where the gradient becomes nearly dry adiabatic (Lindal et al. 1985; Fletcher et al. 2007b). This transition to the adiabat likely indicates the radiative-convective boundary, with temperatures and dynamics at higher pressures determined primarily by convection, and the temperatures at lower pressures determined by solar heating and the solar driven circulation. Stratospheric temperatures at 1 mbar show a strong pole to pole gradient, with the south (summer) pole almost 40 K warmer than the north (winter) pole. The hemispheric temperature asymmetry weakens with increasing pressure, with the winter hemisphere ~10K colder than the summer hemisphere in the upper troposphere, and disappears at pressures greater than about 500 mbar where the temperature becomes nearly uniform with latitude. In addition to the large scale equator-to-pole temperature gradients, between ~2-300 mbar there are temperature variations of 2-3 K on the scale of the zonal jets. Outside the equatorial region, the temperature gradients are correlated with the mean zonal winds, with warmer temperatures where the winds are cyclonic, and colder temperatures where the winds are anticyclonic (Conrath and Pirraglia 1983; Fletcher et al. 2007b, 2008). Temperatures in the equatorial region have been observed to oscillate with a period of ~15 Earth years (Orton et al. 2008; section 7.3.7).

The observed hemispheric-scale temperatures and their temporal variations are qualitatively consistent with seasonal radiative-dynamic models of Saturn (Cess and Caldwell 1979; Bézard et al. 1984; Bézard and Gautier 1985; Barnet et al. 1992; section 7.3.7). Seasonal variations are largest in the stratosphere, where the timescale for response to radiative forcing is about one Saturnian season. The radiative timescale increases at higher pressures, reaching a Saturn year in the troposphere, resulting in a decrease in the seasonal temperature variations and an increasing lag between the solar forcing and the temperature response. The magnitude of the hemispheric differences appears to be larger than can be fully explained radiatively, however; this has implications for the stratospheric circulation.

For an atmosphere in geostrophic balance, where the Coriolis acceleration is balanced by pressure gradients, the meridional temperature gradient is related to the vertical wind gradient through the thermal wind equation:

$$\frac{du}{d\ln p} = \frac{R}{f}\frac{dT}{dy}$$

where $T$ is temperature and $R$ is the gas constant. Conrath and Pirraglia (1983) found that outside the equatorial region, the temperature gradient at 150 mbar in the Voyager IRIS data is anti-correlated with the measured cloud-top zonal wind velocities. The anti-correlation has also been seen in temperatures from Cassini CIRS (Flasar et al. 2005, Fletcher et al. 2007c). Application of the thermal wind equation then indicates that the zonal winds decay with altitude over about 5 scale heights.

To explain the decay of the zonal winds with altitude, Conrath and Pirraglia (1983) proposed a simple model of a meridional circulation that is mechanically forced by the zonal jets; the model was later expanded upon by Gierasch et al. (1986) and Conrath et al. (1990). In this model, turbulent or large-scale eddy processes acting on the mean zonal flow, parameterized by Rayleigh friction, are balanced by Coriolis acceleration acting on the meridional velocities. Mass continuity requires a corresponding vertical velocity. Adiabatic heating or cooling from the vertical motion is balanced by radiative damping parameterized as Newtonian cooling to an equilibrium temperature profile. The resulting meridional circulation has rising motion, and cold temperatures, on the equatorward side of eastward jets, and subsidence and warm temperatures on the poleward side of eastward jets, as is observed. Conrath et al. (1990) also found that the amplitude of the temperature variations is consistent

with the temperature observation when the radiative and frictional timescales are approximately equal. Pirraglia (1989) and Orsolini and Leovy (1993a,b) have proposed a model in which the frictional damping corresponds to eddy fluxes induced by large-scale instabilities of the zonal jets. This has been recently extended to a semi-geostrophic theory by Zuchowski et al. (2009) which allows for the attribution of meridional transport circulations respectively either to frictional damping corresponding to eddy momentum fluxes or to radiative imbalances around or above the visible clouds.

Information on the tropospheric circulation may also be obtained from the distribution of disequilibrium chemical species. Meridional cross-sections of the para-hydrogen fraction $f_p$ in the upper troposphere have been obtained from Voyager IRIS (Conrath et al. 1998) and Cassini CIRS (Fletcher et al. 2007c) data. The IRIS data did not have the spatial resolution to fully resolve the jet structure, but Conrath et al. (1998) did find a minimum of $f_p$ near 60°S and a maximum near 15°S, roughly coincident with a local maximum and minimum in the temperatures, suggestive of upward motion near 60°S and downward motion at 15°S. The CIRS data, with higher spatial resolution, show a local minimum in $f_p$ in a narrow band at the equator, with local maxima at ±15° but stronger in the south. This is suggestive of upwelling at the equator and subsidence at ±15°, which is consistent with the circulation implied by the temperature field. Fletcher et al. (2007a,c) used CIRS data to retrieve the upper tropospheric phosphine abundance in Saturn's southern hemisphere. At equatorial and mid-latitudes phosphine around 250 mbar is approximately anti-correlated with the temperature, consistent with the jet-scale variations in both being driven by vertical motions, except that there is no minimum in phosphine corresponding to the temperature maximum near 15°S. They also found a strong enhancement in the phosphine abundance between 60°S and 80°S for pressures less than 500 mbar. Studies of the upper tropospheric and stratospheric haze also show a change in the properties of the haze particles poleward of ~60°S (Karkoschka and Tomasko 2005; Perez-Hoyos et al. 2005), suggesting that the phosphine enhancement in the polar region may be produced by changes in the chemistry as well as the dynamics.

### *7.3.5 Temporal variation of the equatorial jet*

At most latitudes Saturn's zonal winds have been remarkably stable over time. The one major exception is the prograde equatorial jet (Fig. 7.9). Voyager green filter images yielded a peak zonal wind of ~450 m $s^{-1}$ in the System III reference frame in 1980-81 (Sánchez-Lavega et al. 2000). However, a major outbreak of convective storms was triggered in 1990 (section 7.4.2). The results of Sánchez-Lavega et al. (2004), Temma et al. (2005), and Pérez-Hoyos and Sánchez-Lavega (2006) suggest that the level of tracked equatorial cloud/haze features rose from ~200-360 mb at the time of Voyager to ~45-70 mb after 1990. Barnet et al. (1992) found that winds measured by different HST filters sensitive to different altitudes at this time had different speeds, suggesting the presence of vertical shear in the zonal wind. HST measurements after the 1990 event and over the period 1996-2004 gave systematically weaker equatorial wind speeds of ~275 m $s^{-1}$, independent of wavelength (Sánchez-Lavega et al. 2003, 2004). Cassini ISS wind speeds in 2004 CB2 continuum images yielded equatorial wind speeds intermediate between the Voyager and HST results (~325-400 m $s^{-1}$), but moderate strength methane band filter (MT2) images, which sense higher altitudes, gave speeds similar to those determined from HST (Porco et al. 2005; Sánchez-Lavega et al. 2008).

To what extent can these differences be attributed to real temporal wind changes, as opposed to changes in the altitude at which features are tracked in the presence of a vertically varying, but constant in time, zonal wind? One constraint comes from CIRS thermal winds (Flasar et al. 2005; section 7.3.4; Fig. 7.10). If the Voyager images are assumed to sense cloud features near 500 mb, then the thermal winds imply that Cassini ISS MT2 winds of 275 m $s^{-1}$ would need to be characteristic of levels near ~3-30 mb. This is probably outside the uncertainties in modeling estimates of the haze altitude, suggesting that although a large portion of the apparent change may be due to an upward shift in seeing level after 1990, an additional component of real temporal wind change may be present as well. The VIMS zonal wind profile (Choi et al. 2009; Fig. 7.7), which senses the ammonium hydrosulfide cloud level, suggests that at deeper levels equatorial zonal winds are as strong as or slightly stronger than those retrieved in the visible during the Voyager era. Thus, any real temporal changes in the wind must be restricted to the upper troposphere and lower stratosphere.

Several possible effects of the 1990 convective storm development on the equatorial jet were investigated using a numerical model by Sayanagi and Showman (2007). Convection was represented in this model by the injection of mass at speci-

fied detrainment levels. Geostrophic adjustment to the mass anomaly produced an anticyclonic circulation which, in the presence of a strong β effect, spread the energy longitudinally by wave radiation. The resulting westward-propagating Rossby waves generated by the storm decelerated the jet at their level of critical layer absorption, sometimes reaching the 10 mbar level. In some of their experiments, latitudinal mixing of potential vorticity produced a local minimum in the zonal wind at the equator, a feature common to the jovian planets (Allison et al. 1995). The net result, however, was a decrease in the equatorial jet by only tens of $ms^{-1}$ despite the excessive magnitude of the mass injection assumed.

Other mechanisms not explored by Sayanagi and Showman might further contribute to jet changes. For example, mesoscale gravity waves generated at the tops of thunderstorms are important to the momentum budget of Earth's stratosphere and mesosphere (section 7.3.7). Convective clusters also transport momentum directly, often but not always downgradient; since Saturn's zonal winds decrease upward from the ammonium hydrosulfide cloud level, this effect would actually accelerate upper level winds instead. Thus, while the enhanced convection that occurred after 1990 is likely to have had some decelerating effect on upper level equatorial winds, it is likely to be too small an effect to explain by itself the observed cloud tracked wind differences from the Voyager to the HST to the Cassini eras. Additional long-term changes in cloud altitude, combined with the known thermal wind shear, must probably be invoked to explain the detected changes (Pérez-Hoyos et al. 2006).

Regardless of the contributions to the cloud tracking results by wind changes and cloud/haze height changes, we are still left with the mystery of why Saturn's equatorial region is more variable than the rest of the planet. The 1990 onset of the GWS disturbance is consistent with long-term behaviour that suggests a connection to the seasonal cycle (section 7.4.2). Saturn's large obliquity gives it greater seasonality than Jupiter, and shadowing by the rings can enhance the seasonality at low latitudes. However, sunlight penetrates not much deeper than ~1 bar on Saturn, while GWS-type storms must be driven by water convection originating at ~10-15 bars (section 7.4.2). Furthermore, Bézard et al. (1984) estimate that seasonal effects cause temperature to vary by 1.5 K or less in Saturn's upper troposphere. This modest upper-level destabilization (< 1 K $km^{-1}$ in the model of Barnet et al. 1992) would seem to be incapable of causing convective penetration depths to vary by more than a few kilometres. Finally, if seasonal ring shading is the forcing mechanism for the observed variability, we are left with the question of why the time scale appears to be annual rather than the semi-annual time scale on which one or the other half of the equatorial region should be destabilized. If a longer record of observations eventually suggests semi-annual variability instead, then perhaps the tropospheric convection variations seen near the equator are related to the possible semi-annual oscillation observed in the stratosphere (Orton et al. 2008; Fouchet et al. 2008; section 7.3.7).

### *7.3.6 Upper troposphere temperature knee: structure and seasonality of solar heating*

An interesting feature of Saturn's temperature structure is a "knee" in the vertical temperature profile in the upper troposphere, first noted in temperature retrievals by Voyager IRIS at near-equatorial and southern latitudes (Hanel et al., 1981). The knee was also seen in temperature profiles from Voyager radio occultations at 3°S and 74°S (Lindal et al., 1985). Fletcher et al. (2007b) used Cassini CIRS data from 2004-2006, during southern mid-summer, to map the strength and pressure of the knee as a function of latitude (Figure 7.11). The structure of the knee shows strong hemispheric variations, being very weak or absent in the northern (winter) hemisphere north of 20°N. The knee is higher, smaller, and weaker at the equator and south (summer) pole than at mid-latitudes, and has local maxima in strength at ±15°.

Pérez-Hoyos and Sánchez-Lavega (2006) calculated heating rates from absorption of sunlight in the visible (0.25–1μm) for a range of plausible haze models for different latitudes and seasons. For all of their models, tropospheric heating was confined to a narrow pressure region just below the tropopause. Along with the hemispheric asymmetry in the knee, this led Fletcher et al. (2007b) to conclude that the knee is primarily a radiative effect. The latitudinal variations of the knee are then the result of latitudinal and seasonal variations in insolation, and the distribution and properties of the absorbing aerosols.

The large-scale variations in the atmospheric heating, and thus the structure of the temperature knee, can be partially explained by the latitudinal variation in insolation. In addition, Karkoschka and Tomasko (2005) found that the tropospheric aerosols are larger in the summer hemisphere than the winter hemisphere. This is consistent with the greater northern hemisphere visibility seen in ISS and VIMS images (Figs. 7.2, 7.3, 7.4) Furthermore, Barnet et al. (1992) found that their seasonal

radiative-dynamical model could match the upper temperature structure observed by Voyager IRIS without any heating from aerosols in the northern hemisphere, but aerosol heating was required in the southern hemisphere to match the data.

## *7.3.7 Stratospheric circulation*

### 7.3.7.1 Meridional circulation

The mean meridional circulation in Saturn's stratosphere has primarily been inferred from observations of the temperature field and the distribution of gaseous constituents. The heat equation is:

$$\frac{\partial T}{\partial t} + v\frac{\partial T}{\partial y} + w\left(\frac{\partial T}{\partial z} + \frac{g}{C_p}\right) = \frac{J}{C_p} \approx \frac{T_e - T}{\tau_r},$$

where $v$, $w$ are the meridional and vertical velocities, respectively, $y$ is the northward coordinate, $C_p$ is the specific heat, and $J$ is the net radiative heating. $J$ is often parameterized in terms of a Newtonian cooling rate specified by an equilibium temperature $T_e$ and a radiative relaxation time, $\tau_r$. In the (stably stratified) stratosphere the (second) horizontal advective term on the left-hand side is much smaller than the (third) vertical advective term. The thermodynamic equation does not contain divergences of eddy heat fluxes, because $v$, $w$ are not Eulerian velocities discussed earlier; instead they correspond to the residual transformed Eulerian-mean circulation (see, *e.g.*, Andrews et al. 1987). The use of these variables, common in middle-atmospheric studies, is based on the existence of so-called "non-interaction theorems," which note that for steady, inviscid flow the eddy and wave fluxes of heat and momentum induce mean meridional circulations that cancel these transports (Charney and Drazen 1961; Eliassen and Palm 1961; Andrews et al. 1987). Some transience and dissipation exist in all real atmospheres, but these are often weak enough that the residual circulation provides a more meaningful picture of momentum and heat transports. The thermodynamic equation above is relatively simple and provides a means of probing zonal-mean vertical velocities from the observed temperature field. Dunkerton (1978) has shown that the residual mean circulation in Earth's middle atmosphere is equivalent to the Lagrangian circulation, which describes the transport of quasi-conserved constituents.

Unlike the deep troposphere, the radiative time constant in the stratosphere is sufficiently short (~9.5 yr) that large seasonal modulation of temperatures is expected (Conrath et al. 1990) and observed (Conrath and Pirraglia 1983). However, the thermal contrast between low and high southern latitudes during early southern summer (Flasar et al. 2005; Fletcher et al. 2007b), is much greater than expected from simulations of the atmospheric radiative response assuming a uniform distribution of opacity (Bézard and Gautier 1985). The CIRS observations indicated that 1-mbar temperatures near the south pole were 15 K higher than at low latitudes (Fig. 7.8), whereas the simulations predicted only 5 K in early southern summer. While the effects of the variation in opacity with latitude from hazes and gaseous coolants have yet to be modeled, Flasar et al. (2005) suggested that weak subsidence over the south polar region could also adiabatically heat the stratosphere there. Assuming a balance between the first and third terms in the heat equation, above, they estimated a subsidence velocity ~ 0.01 $cm^{-1}$. Later observations of the south-polar region at higher spatial resolution by CIRS, VIMS, and ISS showed a very compact region with a hot spot extending down to the troposphere, which was also consistent with subsidence over the south pole (section 7.4.5).

So far, only the meridional distributions of ethane ($C_2H_6$) and acetylene ($C_2H_2$) have been mapped in detail in Saturn's stratosphere, at southern latitudes from CIRS nadir-viewing observations (Howett et al. 2007). Perhaps the most striking feature of the meridional profiles is the two-fold enhancement in the $C_2H_6$ abundance at 2 mbar as one moves from mid to high southern latitudes (Fig. 7.12). $C_2H_2$ actually decreases over this range. Ground-based observations at the Infrared Telescope Facility (Hesman et al. 2009) confirm this general pattern but also indicate a localized south pole acetylene peak. Since these hydrocarbons are formed at higher altitudes than probed by CIRS, their mixing ratios should increase with altitude. Thus, one might ascribe the enhancement in $C_2H_6$ to subsidence in the south polar regions, as already suggested by the temperature field. However, the potential problem with this is that one would expect $C_2H_2$ to show a similar increase toward the south pole, because of the short time scales that characterize the photochemical link between the two species (see Chapter 6). This tight

coupling in fact occurs in a 2D chemistry-climate model of Saturn's stratosphere (Moses et al. 2007). Hence the derived distribution of $C_2H_6$ and $C_2H_2$ is currently not well understood.

### 7.3.7.2 Equatorial oscillations

Oscillations in middle-atmospheric zonal-mean temperatures and zonal winds at low latitudes are common on rapidly rotating planets. These have been best studied on Earth, where two major types have been identified. The quasi-biennial oscillation (QBO), dominant in the lower stratosphere, exhibits downward propagating layers of eastward and westward winds (and, from the thermal wind equation, associated warm and cold temperatures at the equator). The period is variable, but averages to ~28 months. The source of this structure is from momentum stresses associated with vertically propagating waves. The wave stresses induce meridional circulations in the equatorial region, and the adiabatic heating and cooling associated with the vertical motions produce the warm and cold temperature anomalies observed to vary with altitude and time. For this oscillation to exist, a set of atmospheric waves including modes with both easterly and westerly phase velocities is needed. Because these waves can transfer zonal momentum, respectively, in the eastward and westward directions, this is a fundamental requirement. Which waves are the key players is a complicated story (see, e.g., Baldwin et al. 2001; Hamilton 1998). The candidates range from planetary-scale to mesoscale: eastward-propagating Kelvin and westward-propagating Rossby-gravity waves have been studied, as well as inertial-gravity waves and gravity waves propagating in both directions. All may well contribute to the QBO on Earth, directly through the zonal momentum deposited in the mean flow, and also by the mean meridional circulations they induce, which transport angular momentum and heat. There is evidence that the QBO influences the Earth's atmosphere at extratropical latitudes. One reason is simply that the induced vertical motions near the equator are associated with meridional cells that close at higher latitudes. Beyond this, the altered pattern of eastward and westward winds at low latitudes modifies the propagation of atmospheric waves. For example, topographically forced (i.e., stationary) planetary Rossby waves cannot propagate in regions where the zonal winds are westward. Waves propagating at low-to-mid latitudes in the winter hemisphere would be refracted poleward, where they can deposit their zonal momentum into the mean flow.

The other major equatorial oscillation in the Earth's stratosphere and mesosphere is the semi-annual oscillation (SAO), and it has a well defined period. It dominates in the terrestrial mesosphere. Forcing by wave-generated momentum stresses is still a critical ingredient of the oscillation, but the cross-equatorial meridional circulation from the summer pole to the winter pole also appears to be important. This may account for the more regular nature of the SAO, effectively synchronizing the natural wave-driven oscillation to a simple fraction of the seasonal cycle.

Ground-based observations of Jupiter identified an oscillation in stratospheric equatorial temperatures, relative to those at adjacent latitudes, with a cycle of 4-5 years (Orton et al. 1991). By analogy with Earth, studies were undertaken to explain this as a quasi-quadrennial oscillation (QQO), based on wave-forcing mechanisms analogous to those for the QBO (Leovy et al. 1991; Friedson 1999; Li and Read 2000). During the Cassini swingby of Jupiter in 2000, CIRS nadir-viewing observations (Flasar et al. 2004) allowed the retrieval of the meridional cross section of stratospheric (from ~1 mbar) and tropospheric (down to 400 mbar) temperatures. The temperatures showed a colder equator at the tropopause near 100 mbar, warmer near 10 mbar, and colder higher up near 1 mbar. Associated with this, the zonal wind first decayed with altitude at the tropopause, and then higher up increased again, leading to a 140 m $s^{-1}$ eastward jet near 4 mbar that had not been previously identified. This vertical structure was broadly consistent with a wave-forced equatorial oscillation, like the terrestrial QBO.

More recently, more than two decades of ground-based observations have identified an equatorial oscillation on Saturn, with a period of ~15 years (Fig. 7.13; Orton et al. 2008). Because Cassini is currently in orbit about Saturn, CIRS observations near periapsis could be undertaken in the limb-viewing mode, providing middle atmospheric temperatures with relatively high vertical resolution and extending quite high into the atmosphere, ~ a few μbar (Fouchet et al. 2008). Fig. 7.14 shows a meridional cross section of temperatures and the zonal winds, relative to those at 10 mbar, below which the mid-infrared limb observations did not probe. One sees the characteristic reversal of relative temperatures and winds with altitude. The limb observations do not constitute a zonal average, but more complete coverage of the stratosphere at 1-3 mbar from nadir-viewing observations indicates that zonal variations at this level are small (Flasar et al. 2005; Fletcher et al. 2007c). Note that the illustrated winds overlay the much larger winds inferred at the cloud tops from feature tracking (Porco et al. 2005), so

the wind field does not reverse, as it does on Earth. Nonetheless, it is plausible that some wave-forcing mechanism analogous to the terrestrial SAO or QBO is at play. One 3-D primitive equation model with prescribed equatorial forcing, for example, produces upward propagating Kelvin waves that might be relevant to the Saturn SAO (Yamazaki et al. 2005). However, the Saturn oscillation needs to be better characterized. It is hoped that the expected descent of the temperature and wind field can be measured, which may be possible if Cassini can observe long enough.

Features associated with these zonal flow oscillations may also be visible in compositional anomalies produced by changes in vertical and latitudinal transport. The meridional cross section of $C_2H_6$ (Fig. 7.15), for example, shows an enhanced tongue extending downward at 20-30° N. Because $C_2H_6$ is expected to form higher up in the atmosphere and because it is relatively long-lived, it should be a good tracer of motion. This suggests sinking motion in this region. This may be associated with the circulations induced by the equatorial oscillation. That happens on Earth, where sinking motion is often observed at mid-latitudes in the winter hemisphere (Baldwin et al. 2001).

### *7.3.8 Potential vorticity diagnosis*

Potential vorticity (PV) is one of the most fundamental variables in dynamical meteorology and oceanography, whose behaviour is crucial to understanding a wide variety of fluid dynamical phenomena. The Ertel form is the most fundamental, defined in terms of potential temperature $\theta$ as

$$q_E = \frac{(2\boldsymbol{\Omega} + \boldsymbol{\xi}).\nabla\theta}{\rho},$$

where ρ is density, and is formally conserved in frictionless, adiabatic flow *provided the composition of the air is uniform* (Gierasch et al. 2004). Unfortunately the latter is not strictly the case in the upper tropospheres of the gas giant planets, because the ortho-para ratio of molecular hydrogen varies across the planet. In principle, this can have significant consequences where the temperature leads to significant differences in physical properties between ortho- and para-hydrogen.

In practice, various approximations to $q$ may be used as the basis for measuring potential vorticity from observations, such as the shallow-water (e.g. Dowling and Ingersoll 1988, 1989) or quasi-geostrophic forms (Gierasch et al. 2004). Most recently, Read et al. (2006a,b, 2009) have combined cloud-tracked velocities and retrievals of temperature and $f_p$ from infrared remote sounding to obtain potential vorticity maps and profiles in the upper tropospheres and stratospheres of both Jupiter and Saturn. This approach uses either the large Richardson number approximation to $q_E$,

$$q_E \approx -g(f + \xi_\theta)\frac{\partial\theta}{\partial p}$$

(where $\xi_\theta$ and $\partial\theta/\partial p$ are evaluated on surfaces of constant $\theta$) or the quasi-geostrophic form (Gierasch et al. 2004)

$$q_G \approx f + \xi_p - \left(\frac{\partial}{\partial p}\left[\frac{pT_d(x,y,p)}{s(p)T_s(p)}\right]\right),$$

where

$$s = -\frac{pc_{p0}}{\langle c_p(p)\rangle}\frac{\partial\langle\ln\theta\rangle}{\partial\ln p}$$

is the stability parameter, defined in terms of potential temperature, $T_s(p)$ is the horizontal mean reference temperature profile, $T_d(x,y,p) = T - T_s$ and $c_p$ is the specific heat capacity of the air. Angle brackets denote horizontal means. A possible advantage of $q_G$ is that it is formally conserved (to O(Ro)) in the absence of diabatic effects or friction, even if $f_p$ varies in space and time.

Typical profiles of $q_E$ on Saturn with latitude largely reflect the behavior of zonal mean absolute vorticity, and generally show a large-scale increase from large negative values in the south to large positive values in the north, crossing zero near the equator. Figure 7.16 shows a profile of $q_E$ at $\theta = 160$ K, just below the Saturn tropopause, derived from Cassini data (Read et al. 2009). Superimposed on the northward increasing global trend, however, are substantial undulations, with steep positive gradients of $q_E$ aligned with eastward jets and much weaker, or even negative, gradients aligned with each westward jet. Such local reversals in $\partial q_E/\partial y$ become most prominent at high latitudes, where the planetary vorticity gradient ($\beta$) is weakest.

The implications of these reversals for the stability of the flow are the subject of controversy, since current models disagree over whether such persistent reversals are to be expected in geostrophically turbulent flow. But the recent results using the best available velocity and thermal measurements for both Jupiter and Saturn do suggest that these reversals in $\partial q_E/\partial y$ are robust features of the circulations of both planets, at least in their tropospheres. Taken at face value, however, this would seem to imply the possibility of barotropic instability around those latitudes where the reversals occur, on the flanks of the eastward jets, while Rossby wave propagation and inhibited meridional transport is anticipated around the eastward jet peaks.

In the north, reversals or near-reversals of $\partial q_E/\partial y$ occur at the latitudes of Saturn's north polar hexagon and "ribbon wave" at 76°N and 47°N, for example. But similar (or stronger) reversals are also found in the south where no such prominent wave-like disturbances occur (although Vasavada et al. (2006) do comment on more localised polygonal perturbations to the jets at 47°S and 62°S, which might indicate a role for barotropic instability, suggested by reversals in the sign of $\partial q_E/\partial y$).

Although an absence of reversals in the sign of $\partial q/\partial y$ would imply stability, the existence of a sign reversal does not necessarily imply instability. Dowling (1995) has drawn attention to the potential relevance of the stability theorems of Arnol'd (1966), the second of which (hereafter, Arnol'd II) emphasizes a flow in which $\partial q/\partial y$ and $\bar{u}$ are linearly related as representing a state of neutral stability. Such a neutrally stable flow may exhibit reversals in the sign of $\partial q/\partial y$ provided these are accompanied by corresponding reversals in $\bar{u}$ *in an appropriate reference frame*. The latter condition is necessary to ensure that Rossby wave propagation relative to the local zonal flow precludes sustained, coherent interactions between adjacent latitude bands. Dowling (1995) presented evidence to suggest that Jupiter's atmosphere approached this state of neutral stability with respect to Arnol'd II quite closely. This was subsequently confirmed using fully stratified PV by Read et al. (2006a).

For Saturn, the PV distributions derived by Read et al. (2009) indicate that its atmosphere seems to approach this neutrally stable state even more closely than on Jupiter, with clear evidence of a locally linear relationship between $\bar{u}$ and $\partial q_G/\partial y$,

$$\bar{u} - \alpha \approx L_d^2 \frac{\partial \bar{q}}{\partial y},$$

(where $\alpha$ is a constant; see e.g. Dowling 1995) at almost all latitudes except close to the equator. The gradient of this relationship provides a measure of the (square of the) local baroclinic Rossby deformation radius which, in Saturn's upper troposphere, appears to range between around 1500 km at high latitudes and more than 6000 km in the sub-tropics. An intriguing additional result of this analysis is the suggestion from the $\bar{u}$-intercept that the reference frame for Rossby wave dynamics on Saturn at most latitudes may be quite different from the System III determined by the Voyager missions, and may even approach the interior rotation period determined by Anderson and Schubert (2007) of $10^h\ 32^m\ 35^s$, a frame that moves prograde relative to System III at more than 100 m s$^{-1}$ at the equator (section 7.2.1). Use of such a 'true' reference frame would render Saturn's zonal velocity profile somewhat less anomalous compared with Jupiter, with mid- and high-latitude jets then alternating in sign with latitude with roughly comparable westward and eastward amplitudes. The effect of this proposed alternative interior reference frame on the dynamics of wave propagation and instability in the upper tropospheres of the outer planets has been compared by Dowling (1995) with the story of the 'princess and the pea', which seems an apt analogy with the notion that such waves and instabilities can 'sense' the circulation at much deeper levels inside the planet.

Whether such an alternative reference frame will be confirmed by more direct methods of determining the interior circulation remains to be seen. But an appealing consequence of the possible approach of both Jupiter and Saturn to a neutrally stable condition with respect to Arnol'd II is that this may explain why most zonal jets in these atmospheres remain coherent and relatively undisturbed for long periods of time. The jets are then sporadically disturbed by occasional perturbations when such jets go locally unstable to form large-scale eddies, such as the compact ovals or polygonal waves.

## 7.4 Discrete features as constraints on processes and structure

The zonally averaged behavior of Saturn's atmosphere defines its global circulation but does not provide all the information needed to diagnose the physical processes responsible for the observed dynamical configuration. Furthermore, many important parts of the atmosphere remain unobserved or poorly observed. The morphology, size, and temporal variation of localized meteorological features helps isolate specific physical mechanisms that may either be manifestations of the important transport processes, or at least diagnostic of physical conditions at levels that are difficult to observe.

### *7.4.1 Anti-cyclonic and cyclonic vortices*

Compared to Jupiter, Saturn has fewer long-lived vortices. Cassini images have confirmed previous Voyager results (Ingersoll et al. 1984) that anticyclones dominate in number over cyclones (Porco et al. 2005; Vasavada et al. 2006). Only four features survived the 9 months period that elapsed between the Voyager encounters (Sánchez-Lavega et al. 2000), among them the largest anticyclone, the North Polar Spot (NPS) at 75.2° N latitude, that was also observed during the years 1992 to 1995 using ground-based telescopes (Sánchez-Lavega et al. 1993b) and HST (Caldwell et al. 1993).

Prior to Cassini, the 1996-2004 HST imaging survey of the southern hemisphere detected the formation of vortices (seen as dark spots at red continuum wavelengths) in the polar area (65ºS to 75ºS) and in southern mid-latitudes (40ºS to 44ºS), in this last case associated with storm activity seen as bright spots in blue - red wavelengths (Sánchez-Lavega et al. 2003, 2004b). The highest concentration (10-15 spots) occurs at mid-latitudes in the equatorward flank of the eastward jets at 47º (northern and southern hemispheres). The vortex production in southern mid-latitudes was confirmed by the first Cassini images from 2004 to 2005 (Porco et al. 2005; Vasavada et al. 2006) suggesting that activity similar to that seen by the Voyagers in the north is now occurring in the south, in a jet similar in latitude location, shape and peak intensity.

Anticyclones appear as oval spots, typically with east-west length up to 5,000 km (most ~1,000 km), dark albedo at 500-900 nm continuum wavelengths, and contrasted dark in the UV and bright in the 890-nm methane band. They drift slowly in either direction relative to the mean zonal flow at 0-10 m $s^{-1}$. In between, convective activity occurs with some regularity, interacting with the vortex circulation (Sromovsky et al. 2003; Porco et al. 2005; Vasavada et al. 2006; Dyudina et al. 2007). Vasavada et al. (2006) report observed episodes of formation and disappearances of vortices suggestive of particular physical mechanisms. Particularly interesting are those cases in which vortices (anticyclones and cyclones) form following the decay of a bright convective storm (Porco et al. 2005; Vasavada et al. 2006). A common interaction between close vortices is mutual orbiting and merger, occurring in particular around latitudes 41º-44º where the maximum concentration of anticyclones occurs.

Vorticity measurements are available only for the anticyclonic "Brown Spot" (BS-1) observed by Voyager with a maximum value of $4.0 \pm 1.5 \times 10^{-5}$ $s^{-1}$, corresponding to a tangential velocity of 45 m $s^{-1}$ (Ingersoll et al. 1984; García-Melendo et al. 2007). Model simulations of this anticyclone (Dowling et al. 1988) from 10 mbar - 10 bar were used to constrain the vertical wind shear and static stability of Saturn's upper troposphere at this latitude (García-Melendo and Sánchez-Lavega 2007). Comparison between the observed and simulated vortex properties indicates that the Brunt-Väisäla frequency is nearly constant from the ammonia to the water cloud levels with a value above $3 \times 10^{-3}$ $s^{-1}$. The one-year stability of this vortex requires that the wind speed slightly decays below the visible cloud deck at a rate no larger than $\partial u/\partial z \sim$ 2-6 m $s^{-1}$ per scale height.

The "North Polar Spot" (NPS) at 75ºN was the largest and long-lived anticyclone observed on Saturn with east-west size of 11,000 km (Sánchez-Lavega et al. 1997). This vortex drifted slowly from 1980 to 1995 at a zonal velocity of just 0.084 m $s^{-1}$ in the Voyager System III reference frame. Calculations of the seasonal insolation at the North Pole together with a simple linear radiative response of the atmosphere to the heating at different altitudes showed a temperature variability of few Kelvins at cloud tops. Because of its long lifetime, and because its motions did not vary appreciably during the 16-year observing period, it seems that the main properties and dynamics of the NPS were insensitive to the external solar forcing.

As stated above, large (~2000-3000 km) stable and coherent cyclones are rarer than anticyclones. The two cases reported in mid-latitudes, the UV spot in the northern hemisphere in the Voyager era (Smith et al. 1981, 1982) and the oval "e" in the southern hemisphere in the Cassini era (Vasavada et al. 2006), are bright in the UV but dark in the 725-nm and 890-nm methane bands, and moderately dark in the continuum. This indicates thinner hazes at their tops relative to anticyclones.

Two remarkable long-lived (> 1.5 yr) cloud features observed by VIMS below the 1-bar level are annular rings of clouds at 48.8 $^{o}$N and 57.5 $^{o}$N latitude planetocentric (Baines et al. 2009c). These features span ~7000 km in diameter, with a central cloud clearing of ~2800 km in diameter. The 57.5 $^{o}$N feature, discovered in 2005, began to dissipate after 3 years of observation, and could not be clearly discerned against the zonal background clouds a few months later. The 48.8$^{o}$N feature has been observed continuously since 2006. It is located in a westward jet, with relative retrograde motion of 2.6 ± 0.1 $ms^{-1}$.

### *7.4.2 Convective clouds and lightning*

Moist convection is the primary mechanism by which Earth's tropical atmosphere transports energy from the radiatively heated surface to high altitudes where it is radiated to space. The same is likely to be true on the jovian planets, except that the energy transported is due to the internal heat source. Different varieties of convection exist on Earth, each diagnostic of the thermodynamic structure and circulation in which it occurs. Shallow cumulus occur in the presence of large-scale subsidence, and transition to midlevel congestus clouds when moisture convergence sets in at low levels but the atmosphere is too dry above to support deep convection (Derbyshire et al. 2004). Deep cumulonimbus that account for most latent heat release require a moist atmosphere and large-scale upwelling; they may be individual cells or mesoscale clusters depending on the sustainability of the cloud base moisture source and the wind shear environment (Schumacher and Houze 2006). They have weak updrafts if the lapse rate is nearly moist adiabatic, or strong updrafts that produce lightning if instability builds before convection is triggered (Zipser et al. 2006; Del Genio et al. 2007b). Diagnosis of convection provides indirect information about conditions near and just above the water condensation level at 10-15 bars, a level not sensed directly by Cassini instruments.

Convective clouds are the most conspicuously visible features on Saturn. They are identified by their high brightness at continuum wavelengths (indicating large optical thickness) and large contrast relative to neighboring clouds and hazes, and by their rapid temporal evolution. Second, methane band filters allow for height discrimination – the brighter the feature in a methane band and the progressively stronger bands in which it is visible, the higher its cloud top. These characteristics imply features that are both high and deep. This detection method has been quite successful for Jupiter, where storms are visible even in a strong methane band (Gierasch et al. 2000; Porco et al. 2003). On Saturn, however, the thick tropospheric haze limits seeing, and no convective features have been observed in the ISS MT3 filter (Del Genio et al. 2007a).

There are two types of convective features on Saturn. The most prevalent are fields of puffy discrete clouds that primarily occupy broad bands centered on the westward jets but are also common in both polar regions (Godfrey 1988; Sánchez-Lavega et al. 1997, 2007; Vasavada et al. 2006; Dyudina et al. 2008, 2009). They are visible in the weak methane band filter MT1 but not the moderate strength band MT2 (Fig. 7.4), suggesting that their tops are only modestly higher than those of other clouds. These may be the equivalent of the midlevel congestus clouds or isolated deep convective cells common over Earth's oceans. Their frequent occurrence adjusts the lapse rate to nearly moist adiabatic, but as a result rising air parcels are only weakly buoyant and sometimes unable to penetrate to great height because of dilution by mixing with drier surrounding air.

More remarkable are the single events that appear suddenly and grow as irregular structures that are dispersed by the meridional wind shear in a few weeks. There are two types of features within this family: occasional mesoscale storm clusters and the rare "Great White Storms" (GWS) (Fig. 7.17). Outbursts of bright spots with sizes ~1,000-3,000 km have been observed in the westward jets at latitude 40ºN in the Voyager era (Hunt et al. 1982; Sromovsky et al. 1983; Ingersoll et al. 1984) and at 35°S in 2004 (dubbed the "dragon storm; Fig. 7.17) by Cassini (Porco et al. 2005; Vasavada et al. 2006; Del Genio et al. 2007a; Dyudina et al. 2007). Another outbreak at this latitude in 2008 was associated with the first tentative spectroscopic detection of ammonia ice on Saturn, presumably formed when the water cloud penetrated the ammonia saturation level (Baines et al. 2009b). Other less dramatic examples are found preferentially in the cyclonic shear regions and at times in the vicinity of the eastward jets, but almost never in regions of anti-cyclonic shear (Del Genio et al. 2007a). This suggests that anti-cyclonic shear regions might be analogous to Earth's subtropics, dominated by large-scale subsidence with possibly an inversion layer of stable temperature and dry air at depth that suppresses vertical development of storms (e.g., Del Genio and McGrattan 1990; Showman and de Pater 2005), while the cyclonic shear regions are areas of net large-scale upwelling at depth.

Cassini images showed dark anticyclones forming after the decay of the dragon storm (Porco et al. 2005; Vasavada et al. 2006), raising the question of whether such storms might be involved in maintenance of the jets (section 7.5.3). The expanding area that occurs after onset indicates divergence, implying upward vertical velocities ~ 1 m $s^{-1}$ over several scale heights (Hunt et al. 1982; Del Genio et al. 2007a). The dragon storm is one of only a few convective features detected in the ISS MT2 filter, indicating that it is deeper than other convective storms. Interestingly, this feature is associated with short high frequency (1-15 MHz) radio emission outbursts (of typical duration 49 ms) known as "Saturn Electrostatic Discharges" (SEDs) (Porco et al. 2005; Fischer et al. 2006, 2007). There is a consensus that SED episodes are due to lightning originating within the storm clouds, in agreement with previous Voyager findings at low latitudes (Kaiser et al. 1983). However, contrary to Jupiter, visible lightning flashes have not been detected. This is probably due to the fact that lightning originates at deeper levels on Saturn (~10-20 bars) than on Jupiter, and thus may suffer more extinction by overlying cloud and the denser Saturn tropospheric haze layer as well as being obscured by ringshine (Dyudina et al. 2007). The dragon storm is not visible in the UV3 (338 nm) and MT3 filters (Dyudina et al. 2007). Using HST multi-wavelength images and a radiative transfer model, Pérez-Hoyos et al. (2005) put the convective cloud tops at ~200 mbar. If the coincident appearance of SEDs and the dragon storm is evidence of lightning, it implies that the westward jets in which the Voyager and Cassini events occurred have lapse rates significantly in excess of the moist adiabatic lapse rate at depth, as is the case for lightning-producing convection on Earth.

The observed distributions of convective clouds and eddy momentum fluxes on Saturn (section 7.3.3) allows us to infer the nature of the mean meridional overturning circulation, which is too weak to observe directly, at and below the cloud tops. Early ideas about the jovian planets, especially Jupiter, interpreted the bright anti-cyclonic zones and darker cyclonic belts to be the result of rising motion (which forms clouds) in the former and sinking motion (which evaporates clouds) in the latter (Hess and Panofsky 1951; Ingersoll and Cuzzi 1969), analogous to Earth's tropical Hadley circulation. Poleward flow aloft from the rising to the sinking branch would experience a positive zonal acceleration due to the Coriolis force, thus maintaining the eastward jets. However, deep moist convection, which occurs overwhelmingly in the presence of low-level convergence and large-scale mean rising motion, was observed by Galileo and Cassini (during its Jupiter flyby) to be restricted to the belts (Gierasch et al. 2000; Porco et al. 2003), leading Ingersoll et al. (2000) to suggest that the belts are actually the seat of net rising motion. This picture is supported by Jupiter's belt-zone ammonia distribution at 1-5 bars (Showman and de Pater 2005). On the other hand, if Saturn had been the only giant planet the Hadley cell analogy might never have been considered, since the albedo-wind shear correlation breaks down there (section 7.3.2). The observed distribution of convection on Saturn is generally consistent with that on Jupiter, although on Saturn convection is observed near the jet latitudes as well as in the cyclonic shear regions. Figure 7.18 illustrates a working hypothesis for the meridional circulation between the water and ammonia cloud levels on Saturn, which is exactly the opposite of the Hadley cell model. Deep moist convection, and thus net rising motion, occurs in cyclonic shear regions, and sinking in anti-cyclonic regions. At the visible cloud tops the meridional flow is then equatorward across eastward jets and poleward across westward jets (Fig. 7.18). The Coriolis force acting on this flow would decelerate both jets. Acceleration of the flow in this picture is instead provided by the observed convergence of the eddy momentum flux into the eastward jets and its divergence from the westward jets (Del Genio et al. 2007a; Showman 2007; Lian and Showman 2008). The remarkable stability of the jets outside the equatorial region suggests that these competing influences are approximately in balance, and thus $fv \sim -\partial\langle u'v'\rangle/\partial y$. A reversed direction meridional return flow near the base of the water cloud would then provide moisture convergence in cyclonic shear regions needed to sustain convection there.

The dynamical source of the eddy momentum fluxes observed by Cassini at cloud top is unknown, but several possibilities exist (section 7.5.3). Figure 7.18 illustrates how one possible mechanism, baroclinic instability, might be consistent with the observed patterns of convection. The instability would produce a poleward and upward eddy heat flux at depth beneath the eastward jets. This in turn would generate upward-propagating waves that lead to eddy momentum fluxes at cloud top. If the jet scale is broader than $L_d$ the fluxes tend to converge on the jet (Held and Andrews 1983). The eddy heat flux convergence at the poleward edge requires rising motion and adiabatic cooling there to maintain hydrostatic equilibrium, while the eddy momentum flux convergence aloft requires the meridional flow described above to remain geostrophically balanced. This is similar to the processes responsible for the midlatitude Ferrel cell on Earth (Hartmann 2007). The deep-seated meridional temperature gradient that drives the baroclinic instability in this picture comes from the moist convection itself (Lian and Showman 2009). Assuming a near-moist adiabatic lapse rate in the cyclonic regions, subsidence along a steeper dry adiabat in the anti-cyclonic regions would suppress deep convection and lead to a warm temperature inversion just above the water condensation level (Showman and de Pater 2005). Temperatures just above cloud base would be lower, but moisture greater, in the convergent cyclonic regions, creating baroclinically unstable conditions between the two. The base-level meridional flow from the anti-cyclonic to cyclonic regions would be initially depleted in moisture but could gradually humidify via upward turbulent mixing from the convective interior, eventually allowing rising parcels to punch through the overlying inversion into the highly unstable air above. This might explain the association of the most vigorous temperate latitude storms on Saturn with the westward jets. A similar flow would occur in this scenario beneath the eastward jets, but there the upward eddy heat flux from baroclinic instability would partly stabilize the lapse rate and obviate the need for moist convection to be as intense. In fact, "slantwise" moist convection on Earth is common within the frontal regions of baroclinic eddies. We might then speculate that isentropic slopes on Saturn in the putative statically stable layer above the base of the water cloud are the combined result of baroclinic and latent heating processes and follow the approximate terrestrial relationship $\Delta_z\theta_e \sim \Delta_y\theta_e$, where $\theta_e$ is the equivalent potential temperature, a conserved quantity for saturated adiabatic ascent, and $\Delta_z$ and $\Delta_y$ are differences over characteristic vertical and horizontal length scales (Frierson 2008). This would differ from the nearly adiabatic layer at higher altitudes, for which the ratio of vertical to horizontal equivalent potential temperature contrasts is small (Allison et al. 1995).

The terrestrial midlatitude analogy may or may not be relevant, though. Baroclinic instability produces jets in numerical simulations of giant planet atmospheres (section 7.5) but has not yet been observed on either Jupiter or Saturn, although one eastward jet feature has been proposed to be the result of such an instability (section 7.4.6). If it does exist, the required heat fluxes should occur primarily below the visible cloud tops, making them a challenge to detect. Coordinated CIRS-VIMS-ISS feature tracks acquired at various times throughout the mission might be examined for correlations between temperature and meridional wind perturbations diagnostic of baroclinic eddies. Furthermore, the width of the terrestrial jet stream is only marginally greater than $L_d$, the scale at which baroclinic instability injects energy into the flow, while on Saturn the two scales may or may not be more widely separated depending on the static stability used to estimate $L_d$. A near-adiabatic value (small $L_d$) would imply different characteristics of the inverse energy cascade leading from the forcing to the jet scale on Saturn (section 7.5). On Saturn, the inferred overturning circulation in Fig. 7.18 cannot penetrate to the tropopause, where latitudinal temperature contrasts retrieved by CIRS are of the opposite sense (section 7.3.4), and haze top height and albedo variations suggest rising/sinking motion in the anti-cyclonic/cyclonic regions instead (section 7.3.2). Finally, other mechanisms may be capable of providing the observed $u'v'$ to accelerate the jets. In at least one model, for example, idealized thunderstorms directly pump the jets over a wide range of assumed $L_d$ values (Li et al. 2006; section 7.5).

Convection in the equatorial region on Saturn differs from that elsewhere. In this region the most dramatic convective events, the "Great White Spots" (GWS), are periodically observed. GWS outbreaks start with the eruption of a very bright spot that grows in days to a size of 10,000-20,000 km (section 7.1.2). Meridional wind shear ultimately disperses the clouds and forms a wake of regularly spaced bright clouds moving zonally in opposite directions at different latitudes dragged by the prevailing winds. The white spots suggest an associated wave phenomenon. Only five such GWS events have been recorded during the last century (in 1876, 1903, 1933, 1960 and 1990) with the three most prominent occurring at the equator in 1876, 1933 and 1990 (Sánchez-Lavega et al. 1991). The 1990 event erupted in Saturn's northern Equatorial Zone at 5ºN, disturbing the whole equatorial band from 8°S to 22°N for several months (Sanchez-Lavega *et al*. 1991; Beebe *et al.* 1992; Barnet *et al.* 1992; Westphal *et al.* 1992). Radiative transfer calculations indicate that the GWS cloud tops reached the tropopause with probable overshooting into the stable region up to 60 mbar (Acarreta and Sánchez-Lavega 1999). Following this last giant dis-

turbance the equatorial region became active in synoptic-scale cloud formation, in particular during 1991 and 1992 (Sánchez-Lavega et al. 1993a). This activity was followed by a second large-scale storm in 1994 at 10°N (Sanchez-Lavega *et al.* 1996) reaching a longitudinal size ~ 27000 km and a latitudinal size ~ 12000 km, with a lifetime > 1 year. It moved with a zonal velocity of 274 m $s^{-1}$, 150 m $s^{-1}$ slower than that of the Voyager mean wind at this latitude (section 7.3.5). White cloud activity continued in the southern Equatorial Zone (13.5°N) during 1996, declining one year later (Sanchez-Lavega *et al.* 1999).

VIMS imagery of the deep troposphere shows discrete, convective cloud structures occupying ~50% of the area near 6°N and S latitude (Baines et al. 2009c; Fig. 7.2). These features span 7,000-9,000 km in longitude and 2,500-4,000 km in latitude, similar to the shape, size and latitudinal position of enhanced ammonia gas absorption mapped by RADAR (Janssen et al. 2008). These results suggest that the equatorial region is typically convectively unstable at depth, perhaps continually supplying aerosols that form the thick upper tropospheric haze observed at these latitudes. The GWS and other visually-observed outbursts are likely then just the manifestation of unusually energetic convective motions by these regularly occurring clouds.

Our inferences of convective clouds in Saturn images are indirect – unlike Earth, we have no measurements of precipitation or static stability beneath the visible cloud tops, nor do we even know the composition of the clouds we identify as convective features. In recent years, however, numerical models have been employed to support our interpretations. These models indicate that convection starting in the water clouds is the only plausible candidate mechanism to explain the more obvious organized, deeply penetrating features such as the GWS and dragon storm. A standard 1D ascending parcel model driven by the latent heat released upon condensation of water and ammonia, can explain the high altitude of the cloud tops (Sánchez-Lavega and Battaner 1986). The details of the development, growing stage and evolution of the storm (including microphysics and interaction with surrounding air) have been studied in detail with a 3D anelastic model by Hueso and Sánchez-Lavega (2004). Buoyant parcels can develop from an initial heating of 1-2 K at the water cloud level at 10 bar when the environment becomes saturated and the water abundance is assumed to be supersolar. In the core of the updrafts the vertical velocities can reach 150 m $s^{-1}$. Less vigorous moist convective storms can also develop at the ammonia cloud level, in particular under very large abundances of ammonia (10 times solar). These might explain some of the ubiquitous puffy clouds in the broad latitude bands between successive eastward jets and in the polar regions. However, deeper isolated water-based convective cells are equally likely to explain these features if the lapse rate is near-neutral and the relative humidity above cloud base subsaturated.

### *7.4.3 Upper troposphere thermal features and Rossby waves*

Diagnosis of the physical mechanisms responsible for observed wavelike and eddy mixing behavior seen within and above the cloud layer is aided by knowledge of the vertical extent of such disturbances. Temperature retrievals in the upper troposphere with sufficient spatial and temporal resolution provide one useful constraint.

Achterberg and Flasar (1996) used a set of global mapping observations by Voyager IRIS to search for waves in Saturn's temperature field in the upper troposphere at 130 and 270 mbar, although the relatively large IRIS field of view, approximately 8° of latitude, meant they were only sensitive to planetary scale waves. The majority of statistically significant features in the data were at wavenumbers $k \leq 4$ at 130 mbar at low to mid-northern latitudes. By far the most prominent wave was a quasi-stationary zonal wavenumber 2 feature extending from 10°N to 40°N at 130 mbar. The meridional structure of this wave is shown in Figure 7.19. The wave has a maximum amplitude of ~0.5K at 35°N-40°N, at the northern edge of the equatorial jet, with an amplitude that drops rapidly to the north, and more slowly to the south. The zonal phase of the wave is constant between 10°N and 45°N. The amplitude of the wave at 270 mbar was roughly half of the amplitude at 130 mbar.

Ray-tracing calculations by Achterberg and Flasar (1996) showed that the observed structure of the wavenumber 2 wave was consistent with a quasi-stationary Rossby wave, confined meridionally by the structure of the zonal winds, and to pressures less than ~200 mbar by the static stability structure. Furthermore, for wave velocities near zero, the structure of the waveguide is consistent with the generation of barotropic instabilities through wave overreflection at a critical layer where the wave velocity equals the zonal wind velocity (Lindzen *et al*. 1980). Also, the meridional gradient of potential vorticity (section 7.3.8), calculated from Voyager imaging and thermal data, changes sign at approximately the latitude where the mean zonal wind is zero. This led Achterberg and Flasar (1996) to propose that the observed quasi-stationary wavenumber 2 wave is forced by a barotropic instability of the zonal mean flow. The wave is quasi-stationary because the instability occurs at a lati-

tude of weak zonal wind velocity, and not because the wave is linked to Saturn's interior, as has been proposed for quasi-stationary waves on Jupiter (Magalhaes *et al*. 1990) and for Saturn's north polar hexagon (Godfrey 1990; section 7.4.4).

Periodic temperature anomalies have also been detected in CIRS data at 160 mb, at the northern latitude of the ribbon wave (Fletcher et al. 2007c; section 7.4.6). These periodic structures thus may be related to a deep-seated disturbance, perhaps associated with baroclinic instability (Godfrey and Moore 1986). Orton and Yanamandra-Fisher (2005) also observe temperature oscillations near 100 mb at 32°S, where a weaker version of the ribbon morphology is seen (section 7.4.6).

### *7.4.4 North polar hexagon*

Polar projection maps of Voyager 2 images of Saturn's north polar region by Godfrey (1988) revealed a striking hexagonal cloud structure surrounding the pole at about 76°N planetocentric latitude, with a prominent anticyclonic oval, the North Polar Spot (NPS), centered on the southern side of one of the hexagon edges. Wind measurements (Godfrey 1988) showed that the hexagon coincides with a strong eastward jet (100 m $s^{-1}$), with the velocity streamlines also following the hexagonal pattern. The hexagonal pattern, however, was stationary, to within measurement error, in the System III reference frame assumed at the time to indicate the rotation rate of Saturn's interior. By adding in an observation from Voyager 1, Godfrey (1990) measured a small eastward velocity for the NPS, and presumably the hexagon, of 0.108±0.007 m $s^{-1}$.

A decade after the Voyager encounter, the hexagon and the NPS were observed in HST (Caldwell *et al*. 1993) and ground based (Sanchez-Lavega et al. 1993b, 1997) images. Measurements of the longitude of the NPS in these datasets give long-term averaged drift rates between 0.11 and 0.23 m $s^{-1}$ depending upon the time span used, indicating long-term changes in the rotation period of the hexagon. There were also short term variations in the drift rate of the NPS of about ±4 m $s^{-1}$.

Starting in 1996, the latitude of the hexagon was unobservable from Earth and in shadow during the Cassini mission until 2009. Prior to 2009, however, the hexagon was detected in thermal emission by both CIRS and VIMS. Maps of upper tropospheric temperatures (100 to 800 mbar) by CIRS (Fletcher *et al*. 2008) show a hexagonal warm band at 79°N, and a hexagonal cold band at 76°N (Fig. 7.20 left). The temperatures are consistent with the standard upper troposphere pattern on both Jupiter and Saturn of warm temperatures in regions of cyclonic shear on the poleward side of eastward jets, and cold temperatures in regions of anticyclonic shear equatorward of eastward jets, suggesting that the hexagon is a typical jet except for its hexagonal shape. The hexagon is also clearly visible in 5 μm thermal images from VIMS (Baines et al. 2009a), which are sensitive to large-particle cloud opacity at 1.5-4 bars. Figure 7.20 (right) shows Saturn's emission through clearings between the clouds, which are silhouetted against the background glow. Hundreds of discrete clouds populate the scene inside the polar hexagon. The hexagon, located near 78°N (planetocentric) is comprised of several nested and alternating hexagonally-shaped clouds and clearings. Near the pole, alternating concentric bands of thick and somewhat optically thinner clouds extend out to ~ 87°N. As observed 4 times over 6 hours, the pole itself has a near-stationary cloud feature that is offset from the pole by 0.5 degrees of latitude (~ 500 km), surrounded by a narrow ring of clearings in the clouds about 0.5 degrees wide. This behavior is different from that in the Southern Hemisphere, where cloud clearing occurs at the pole (section 7.4.5). The combination of CIRS and VIMS observations indicates that the hexagon exists over an extended pressure range from at least the tropopause region (50 mbar) down to the ~3 bar pressure level, consistent with features in other eastward jet regions.

The VIMS hexagon cloudy and clear latitudes correlate with the CIRS cool and warm latitudes, suggesting rising and sinking in the eastward jets are correlated over great vertical distances. This is a counter-example to the tendency elsewhere for inferred vertical motions at depth to differ from those in the upper troposphere. It is interesting to note that in baroclinic instability models of gas giant planets (Williams 2003; Lian and Showman 2008a), vertical and especially horizontal eddy heat fluxes at eastward jet latitudes are coherent over great depths, a behavior that may be relevant to this question.

VIMS detections of the hexagon in 2006 and 2008 indicate that it is still stationary in the Voyager reference frame (Baines et al. 2009c). Small clouds embedded within the clear regions move at about 125 m $s^{-1}$, similar to the zonal speeds observed by Voyager. Flows outside the hexagon are significantly less – about 30 m $s^{-1}$ (Baines et al, 2009a). Thus, over a quarter century, the basic structure and dynamical characteristics of the north polar hexagon appear to have changed very little.

The persistence of the hexagon over nearly a full Saturnian year suggests that it is insensitive to solar forcing. The small drift rate in System III, less than the uncertainty in the Voyager radio period, led to suggestions that the hexagon and the NPS are rooted in the deep interior (Godfrey 1988, 1990; Caldwell *et al.* 1993). However, the radio period is now known to be variable (see Chapter 11) and likely not representative of Saturn's interior rotation rate, making any direct relation between the hexagon and Saturn's interior unlikely. Allison *et al.* (1990) proposed that the hexagon is a stationary Rossby wave imbedded in and meridionally trapped by the eastward jet, and forced by the interaction of the jet with the NPS. Matching the observed phase velocity requires that the Rossby wave be vertically trapped, which may be consistent with the confinement of the observed hexagon to the troposphere (Fletcher et al. 2008).

An alternative view has been put forward by Aguiar et al. (2009), based on a laboratory analog of the barotropic instability of zonal shear layers and jets. In the experiment, a zonally-symmetric shear layer or jet is maintained in a cylindrical tank by differentially rotating sections of the horizontal boundaries. The whole container is then rotated about the vertical axis of symmetry, so that a Rossby number for the flow can be defined as

$$Ro = \frac{R\omega}{2\Omega H},$$

where $R$ is the radius of the jet or shear layer, $H$ the depth of the tank, $\omega$ the angular velocity of differential rotation and $\Omega$ that of the background rotation. Both jets and shear layers in such a system exhibit inflection points such that the absolute vorticity gradient changes sign with radius, and can therefore exhibit fully developed barotropic instability if the effective Reynolds number is sufficiently large.

When barotropic instability occurs, the fully developed form equilibrates to a large amplitude Rossby wave-like pattern, whose manifestation may resemble polygonal meanders of the original jet or shear layer. Under conditions favoring wavenumber $m = 6$, the flow appears as a hexagonal jet (with rounded corners), which may be accompanied by cyclonic or anticyclonic vortices both inside and outside the hexagon whose strength depends on the velocity profile of the jet or shear layer. A typical example of such a flow is illustrated in Fig. 7.21 below. In this case the equilibrated hexagonal flow maintains a constant amplitude (so long as the basic jet or shear layer forcing is maintained), and moves around the tank at a rate determined by the strength of the jet or shear layer and any β-effect produced, e.g., by a sloping bottom. The scale selection process in these experiments, favoring $m = 6$ in this case, is not well understood, but these (and similar) experiments (e.g., Niino and Misawa 1984; Sommeria et al. 1991; Fruh and Read 1999) suggest a dependence of equilibrated wavenumber primarily on the ratio of the width of the jet to its radius of curvature (cf. Howard and Drazin 1964). In practice this appears as a dependence primarily on the imposed Rossby number, with relatively little dependence on the viscosity of the fluid.

These experiments suggest the possibility that Saturn's hexagon owes its origin to the predominantly barotropic instability of the strong jet at 76°N. The nonlinear equilibration of this instability would lead to a steady amplitude Rossby wave which, in a spherical domain, propagates retrograde relative to the eastward jet. According to this scenario, however, there is no fundamental reason for the hexagonal wave to be stationary in any particular System III, although its retrograde propagation relative to the eastward jet might happen to render it very slowly-moving in Voyager's System III. The origin of the NPS (and other, weaker and more ephemeral vortices noted by Godfrey [1988]) is then seen to be from the same instability as the hexagon itself, in the same way as vortices appear on either side of the hexagonal jet in the laboratory experiments.

### *7.4.5 South polar vortex*

Ground-based measurements prior to Cassini revealed a dark disk-shaped feature at visible wavelengths centered on the South Pole and extending to 88.5°S with warm temperatures relative to its surroundings (Orton and Yanamandra-Fisher 2005). ISS imaged the feature in 2004 and at higher resolution in 2006 in continuum and methane band filters (Dyudina et al. 2008, 2009; Fig. 7.22 left). These observations revealed a dark central "eye" with either clear air or lower cloud tops relative to two surrounding "eyewalls" of thicker, higher clouds at 88 and 89°S planetocentric. The height of the inner and outer "eye-

walls" was estimated to be 70 ± 30 and 40 ± 20 km relative to the surrounding clouds based on the shadows they cast. High-resolution images acquired in 2008 show a third innermost ring of somewhat elevated clouds punctuated by occasional deep convective clouds, some of which appear to be creating vortices at their divergent outflow levels. Dozens of small (< 1000 km in diameter) discrete puffy clouds occupy the south polar region farther away from the pole.

The use of the terms "eye" and "eyewall" for the cloud morphology of the south polar feature is obviously evocative of terrestrial hurricanes, which also have clear central eyes and surrounding eyewalls of towering convective clouds. It is instructive to explore what the Saturn feature does and does not have in common with terrestrial hurricanes. The structure and physics of hurricanes is reviewed by Emanuel (2003). Hurricanes are cyclonic vortices, with tangential wind speeds increasing toward the center, peaking at the eyewall, and then decreasing within the eye. The Saturn south polar feature is also a cyclonic vortex, with peak prograde winds of 160 ± 10 m $s^{-1}$ at 88°S (the outer "eyewall") in ISS and VIMS images, decreasing poleward and more slowly equatorward to < 10 m $s^{-1}$ at ~80°S (Fig. 7.22 right). Hurricanes are warm-core features; the Saturn south polar vortex has enhanced VIMS 5 μm emission at the pole, indicating clearing at depth, and anomalously warm central temperatures in CIRS data just beneath the tropopause (by 5 K) and also in the stratosphere (by 3-4 K) (Fletcher et al. 2008). The warm central core implies a decay of the vortex wind speed with altitude of ~10 m $s^{-1}$ per scale height (26 km at the pole), which is also consistent with the slightly stronger wind speeds measured by VIMS at deeper levels (Dyudina et al. 2008b).

Hurricanes have maximum angular momentum at their outer periphery, decreasing inward due to friction experienced by the near-surface radial inflow, and upper level divergent outflow; observed latitudinal near-surface wind profiles often exhibit approximately constant vorticity. The Saturn south polar vortex wind profiles also decrease in angular momentum toward the pole and exhibit almost constant absolute vorticity (Fig. 7.22 right). However, no evidence for systematic meridional flow toward or away from the pole has been found; in the absence of such evidence a more reasonable interpretation might be that eddy mixing smoothes the vorticity, as it appears to do at lower latitudes (section 7.3.8).

Thus, obvious morphological similarities between the Saturn south polar vortex and terrestrial hurricanes exist. However, this may be the extent to which the analogy can be carried. Hurricanes are transient propagating features, often originating in the troughs of tropical easterly waves that propagate from the continents over ocean. The warm tropical ocean surface is crucial to the genesis of hurricanes, being the source of moist entropy via surface evaporation and sensible heat fluxes during the near-surface radial inflow that provides the energy to intensify an existing convective vortex (Emanuel 2003). Hurricanes weaken quickly once they reach land and are cut off from the surface moisture source. The Saturn vortex, however, is a polar feature (itself not a problem since polar and equatorial temperatures are comparable on Saturn), fixed in location, and apparently long-lived. Hurricanes can have multiple eyewalls, but these usually migrate inward and are replaced by eyewalls farther from the center, whereas the Saturn "eyewalls" are fixed. Most importantly, there is no real equivalent to the terrestrial ocean surface source of moist entropy. Turbulent mixing of water vapor up to the condensation level may provide the condensation source that drives the convection in the Saturn vortex "eyewalls," but this may be no different than the situation occurring in eastward jets and cyclonic shear regions at other latitudes, where low-level convergence organizes moist convection (Fig. 7.18). Thus, the Saturn south polar vortex is more appropriately viewed as a feature of the mean meridional circulation.

We also note that Saturn's north and south poles are more similar than different. VIMS detects a north polar vortex with winds peaking at 88°N, but with a higher velocity (200 m $s^{-1}$) than that at the south pole. While the south pole does not have a hexagonal structure (Sánchez-Lavega et al. 2002b), Vasavada et al. (2006) do report polygonal segments of cloud there.

### *7.4.6 Other wavelike features*

The "ribbon wave" at 47°N planetographic latitude (section 7.1.2) was discovered by Voyager (Smith et al. 1981, 1982; Sromovsky et al. 1983), and detected again in 1994-95 HST images (Sanchez-Lavega et al. 2002a). It appears to still be present, though its morphology is somewhat different. It is visible in 2007 ISS images (Fig. 7.4) near 41°N planetocentric as a more zonally oriented bright cloud band at some longitudes, interrupted by an isolated kink in its structure but more wavy in appearance to the east. VIMS viewed the ribbon in 2008 in 2.7 μm reflected sunlight, finding that it circles the planet at this

latitude with mean longitudinal wavelengths of ~4000 km, somewhat shorter than the 5710 ± 260 km wavelength derived by Godfrey and Moore (1986) from Voyager images. The ribbon wave is embedded in and moves with a strong (140 m $s^{-1}$) eastward jet, with cyclonic and anticyclonic vortices nested to its north and south. UV and methane band images indicate that the brightness reverses between the northern and southern parts of the ribbon. Radiative transfer modeling suggests that the haze top is 14 km higher to the south than to the north, consistent with upper level upwelling/downwelling in anti-cyclonic/cyclonic shear regions (Godfrey and Moore 1986; Sanchez-Lavega et al. 2002a). The pattern resembles those seen in laboratory rotating annulus experiments of sloping convection (Hide et al. 1994). In view of the strong thermal gradients measured across the ribbon (Conrath and Pirraglia 1983), Sromovsky et al. (1983) and Godfrey and Moore (1986) suggested that it might be the product of baroclinic instability. The presence of a flattening or possible reversal in the sign of the latitudinal gradient of upper troposphere potential vorticity at this latitude (section 7.3.8; Fig. 7.16) is consistent with such an interpretation. Godfrey and Moore (1986) detected the ribbon in UV images and concluded that it extends upward from the cloud level to at least 170 mb. CIRS in fact detects periodic temperature anomalies at 160 mb at this latitude (Fletcher et al. 2007c; Fig. 7.23 upper) that are likely to be associated with the ribbon. Thin undulating bright bands are also seen in VIMS 5 μm images (Fig. 7.3 lower); this might be consistent with a baroclinic instability origin if the temperature gradients driving the perturbation were due to latent heat release at the water cloud level. Saturn's southern hemisphere also exhibits subtle ribbon-like features with similar morphology in eastward jets at 48 and 32°S, but these do not fully encircle the planet (Sanchez-Lavega et al. 2000). It is interesting to note that no ribbon waves have been detected in Jupiter's midlatitude eastward jets.

The "string-of-pearls" discovered in VIMS 5-μm imagery at 33.5°N planetocentric (Baines et al., 2009c; Fig. 7.23 lower) is located at pressures greater than 1 bar. It is not seen either in ISS images of the ammonia cloud and upper tropospheric haze (Fig. 7.4) or in CIRS upper troposphere temperature maps (Fig. 7.23 upper), suggesting that it is strictly a deep-seated feature with little upward propagation. It has been observed consistently for over 2.8 years. The holes of enhanced emission are spaced ~3500 km apart, span ~800 km each, and are confined to a latitude range of ± 2°. The string-of-pearls resides near a westward jet and exhibits a retrograde mean zonal motion of 22.65 ± 0.04 m $s^{-1}$ in the Voyager reference frame.

## 7.5 Theories and models of the general circulation

### *7.5.1 Deep cylinders vs. shallow weather layers*

Two endpoint scenarios exist for the jet structure below the clouds on giant planets. In the ``shallow structure'' scenario, the jets are confined to a layer within several scale heights below the clouds (e.g., Hess and Panofsky 1951, Ingersoll and Cuzzi 1969). Through the thermal-wind relationship, this would require the anticyclonic regions (zones) to be warm and cyclonic regions (belts) to be cold. Such temperature contrasts might result from latent heating associated with condensation of water vapor, latent heating from ortho-para conversion, or latitudinal variations in absorbed sunlight. In the ``deep structure'' scenario, the observed cloud-level jets are hypothesized to extend downward through the ~$10^4$-km-thick molecular envelope. This scenario is motivated by the likelihood that Jupiter and Saturn transport their internal heat flux via convection (section 7.2.2), and hence that their interiors must be close to a barotropic state. Under such conditions, the Taylor-Proudman theorem implies that the jets would be constant on cylinders parallel to the rotation axis (so-called ``Taylor columns'').

As emphasized by Vasavada and Showman (2005), hybrid scenarios are also possible with Taylor columns in the deep interior and a baroclinic thermal-wind region within the few scale heights below the clouds. The argument for near-barotropic conditions in the deep molecular envelope is strong, because convection homogenizes the entropy and plausible convective density anomalies are extremely small. However, all four giant planets exhibit distinctly *non*-barotropic conditions at the cloud level, with ~5 K variations of temperature with latitude on constant-pressure surfaces. Such a baroclinic region could easily penetrate several scale heights or more below the clouds (Allison 2000). In this scenario, the cloud-level winds would not represent the speeds of the Taylor columns, but rather the speeds of the Taylor columns plus the height-integrated thermal-wind shear within this outermost baroclinic zone.

Early work suggested a possible problem with the shallow-structure model for Saturn (Ingersoll et al. 1984), but recent updates may have dissolved this problem. Jupiter's approximate jet speeds can be explained using thermal-shear from a level of no motion at ~10 bars if the belt-zone temperature differences are only ~5-10 K (Ingersoll and Cuzzi 1969). The required belt-zone temperature differences and depths could plausibly result, for example, from latent heating due to condensation of water vapor. In the case of Saturn, however, the Voyager-era winds were thought to be predominantly eastward (Fig. 7.1). If the level of no motion were at tens of bars, the required latitudinal temperature differences would be a factor of two, which are implausibly large. The required latitudinal temperature contrasts could be decreased by moving the level of no motion deeper (Ingersoll et al. 1984). However, it is now clear that Saturn's rotation rate is poorly known (see Chapter 11), and proposed revisions to the rotation rate (Anderson and Schubert 2007) imply that the jet profile consists of alternating eastward *and* westward jets. This revision largely mutes the difficulty outlined by Ingersoll et al. (1984) and has other potential advantages (section 7.3.8), but there is as yet no definitive *physical* basis for concluding that the faster rotation rate estimate is indeed the true internal rotation rate (section 7.2.1).

Most authors have long assumed that the strong zonal jets observed at cloud level do not penetrate into Jupiter and Saturn's metallic regions (at pressures exceeding ~1-2 Mbar and depths of perhaps $10^4$ km) because the Lorentz force would brake strong zonal flows there (Kirk and Stevenson 1987, Grote et al. 2000, Busse 2002). Recently, Liu et al. (2008) extended these arguments by suggesting that the zonal flows cannot penetrate even to the base of the molecular region (substantially above the dynamo-generating region). Motivating their work is the experimental inference (e.g., Weir et al. 1996, Nellis et al. 1992, 1999) that the transition from molecular to metallic is smooth, implying the existence of a substantial layer at the base of the molecular region that, while not metallic, exhibits significant electrical conductivity. Based on an inward extrapolation of the axisymmetric part of the observed magnetic field, and assuming the cloud-level winds extend downward on cylinders, Liu et al. (2008) calculate that the Ohmic dissipation would exceed the planet's observed luminosity if the Taylor columns penetrate deeper into the interior than 0.96 and 0.86 of the radius for Jupiter and Saturn, respectively. The implication is that the Taylor columns do not penetrate deeper than this level. As Liu et al. (2008) point out, it is difficult to envision how the Taylor columns would terminate immediately above this level (or indeed anywhere within the near-isentropic molecular envelope) because plausible deviations from barotropicity are very small within the molecular envelope. Liu et al. (2008) therefore favor a scenario with mid- and high-latitude winds confined primarily to a weather layer near the clouds. The equatorial jet may be an exception, since even if it were barotropic it does not penetrate deeper than the cutoff radius calculated by Liu et al. (2008).

Glatzmaier (2008) challenged the Liu et al. (2008) scenario on the grounds that they simply extrapolated inward the magnetic field and zonal flows using plausibility arguments (rather than, for example, a self-consistent 3D magnetohydrodynamics calculation) and that other plausible configurations for the deep zonal flows could imply much lower Ohmic dissipation, thereby circumventing the Liu et al. constraint. Non-zero Ohmic dissipation requires the poloidal component of magnetic field to have a component perpendicular to the lines of constant angular velocity of fluid motion. This is the case for the assumptions of Liu et al. Glatzmaier pointed out, however, that if one extrapolates the zonal jets inward not along cylinders parallel to the rotation axis but instead on lines parallel to the internal poloidal magnetic field, then the Ohmic dissipation would be zero. However, this configuration would require the Taylor-Proudman theorem to be significantly violated for the zonal jets in the molecular envelope, which is not an easy task. Glatzmaier (2008) proposed that this could occur if, for example, the convective Reynolds stress plays an important role in the force balance (thereby causing a violation of geostrophy, on which the Taylor-Proudman theorem is based). But, given Jupiter and Saturn's small heat fluxes, and hence the small power available for causing Reynolds stresses, the accelerations due to Reynolds stresses must likewise be weak compared with the Coriolis and pressure-gradient forces associated with the basic zonal-jet structure.

### *7.5.2 Distinguishing deep-or-shallow structure from deep-or-shallow forcing*

Vasavada and Showman (2005) and Showman et al. (2006) emphasized that one must distinguish deep versus shallow models for the *structure* of the jets from deep versus shallow models for the *forcing* that maintains the jets. Most authors have implicitly assumed that shallow forcing (e.g., thunderstorms or baroclinic instabilities within the cloud layer) can only produce shallow jets (and thereby that the forcing must be deep if the jets are deep). Showman et al. (2006) and Lian and Showman (2008) constructed a model based on the primitive equations that explicitly showed, however, that deep jets can easily result

from shallow forcing as well as from deep forcing. In their models, they applied a jet pumping confined to pressures less than a few bars, intended to represent the convergences of eddy momentum flux associated with weather-layer processes such as thunderstorms or baroclinic instabilities. These eddy accelerations were assumed zero at pressures exceeding a few bars. Their solutions, however, showed that the shallow eddy accelerations induce a meridional flow that (in the case of a giant planet with an almost neutrally stratified interior) extends to essentially arbitrary depths. The east-west Coriolis acceleration on these meridional motions then pumps the zonal jets at all depths, not just those within the weather layer. The result is a jet structure consisting of a baroclinic thermal-wind region in the weather layer (where the jet pumping occurs in their model) underlain by barotropic zonal jets, extending to the bottom of the domain, whose speeds can attain values similar to those at the top.[1] An implication is that the fast winds observed by the Galileo probe down to 20 bars on Jupiter (Atkinson et al. 1998) cannot be interpreted as implying that the zonal jets have a deep-convective origin, as has often been done in the literature.

It is also conceivable that *deep* forcing could drive *shallow* jets. For example, convection in the interior could generate waves that propagate upward and induce zonal winds at a low pressure detached from the generation region of these waves. Such a process is responsible, for example, for generating stratospheric zonal winds in the Quasi-Biennial Oscillation on Earth (Baldwin et al. 2001) and in the Quasi-Quadrennial Oscillations on Jupiter and perhaps the Semi-Annual Oscillation on Saturn (Leovy et al. 1991; Friedson 1999; Li and Read 2000; Fouchet et al. 2008; Orton et al. 2008).

### *7.5.3 Models for jet pumping*

Vasavada and Showman (2005) provided an extensive review of the theories and models for pumping the zonal jets on Jupiter and Saturn up through early 2005. We refer the reader there for an introduction; here, we emphasize only the most recent developments. Jet-formation theories can loosely be categorized into the ``shallow forcing'' scenario, where jet pumping occurs by baroclinic instabilities, thunderstorms, or other weather-layer processes within the cloud layer, and the ``deep forcing'' scenario, where the jet pumping results from Reynolds stresses associated with convection within the molecular envelope. The past few years have seen significant development in both approaches.

As emphasized by Vasavada and Showman (2005), most modern theories for jet formation on giant planets assume that the jets result from an inverse energy cascade modified by the $\beta$ effect. By allowing propagating, dispersive Rossby waves, the $\beta$ effect introduces anisotropy in the turbulent interactions that often lead to the production of jets with a latitudinal length scale of $L_R \sim \pi(U/\beta)^{1/2}$, called the Rhines scale, where $U$ is a characteristic zonal wind speed (Rhines 1975). This mechanism was first explored for Jupiter by Williams (1978), and since that time, numerous numerical and laboratory studies have been performed that investigate jet formation by this process.

The traditional interpretation is that the Rhines scale is a transition wavenumber between turbulence (which acts at scales smaller than $L_R$) and Rossby waves (which act at scales larger than $L_R$). The idea is that small-scale turbulence experiences an inverse cascade that drives the energy to larger and larger length scales, but once the turbulence reaches scales of $L_R$, further transfer of the energy to larger scales would require wave-turbulence interactions, which are inefficient. Energy would thus pile up at scales comparable to $L_R$. In the older 2D- turbulence literature, the Rhines scale was thus often interpreted as an ``arrest'' or ``halting'' scale, as though the Rhines scale acted as a barrier to the inverse cascade. This picture was developed in the context of decaying turbulence studies (where turbulence is initialized in an initial state which then freely evolves without any further forcing or large-scale damping).

However, the above interpretation of $L_R$ does not carry over to studies with small-scale forcing. Indeed, recent work has clarified that the $\beta$ effect cannot provide a source of energy dissipation and thus does not act to ``arrest'' the inverse cascade in any meaningful sense (Galperin et al. 2006; Sukoriansky et al. 2007). Furthermore, in some contexts (known as the "zonostrophic regime"; Galperin et al. 2006, 2008), the wave-turbulence transition actually occurs at a wavelength $L_\beta \sim (\varepsilon/\beta^3)^{1/5}$ (where $\varepsilon$ is the small-scale isotropic energy injection rate) which may be significantly smaller than $L_R$ (Huang et al. 2001; Sukoriansky et al. 2007). In a system that lacks large-scale dissipation but that is forced at small scales, the kinetic energy in-

[1] Because Showman et al. (2006) and Lian and Showman (2008) used a shallow-atmosphere model, the jets penetrated downward vertically, but in reality these jets would penetrate downward along cylinders parallel to the rotation axis.

creases continually over time, so the Rhines scale increases too because of its dependence on $U$. In a system with small-scale forcing and large-scale friction (e.g., Rayleigh drag), the drag removes the injected energy as it cascades upscale, so a statistical balance is reached with an approximately steady mean wind speed and hence $L_R$. In both cases (assuming the friction is not overly strong), $L_R$ roughly represents the scale containing the most energy, which corresponds typically to the jet width.

The zonostrophic regime (Galperin et al. 2006, 2008) represents a particular situation found when $L_R$ and $L_\beta$ are widely separated (by at least a factor of 2), so that a significant inertial range develops between these scales. In this case, the turbulent energy transfers on scales smaller than $L_\beta$ become highly anisotropic and tend to focus energy strongly into zonally-symmetric flow components. The result is that more and more energy gets concentrated into the zonal jets until a dynamic equilibrium is reached between jet pumping and energy removal by large-scale friction processes and the barotropic instability of the jets themselves. Under these circumstances, the zonal mean jet structure may acquire a steeply sloped kinetic energy spectrum $E(k) \sim C_Z \beta^2 k^{-5}$ (where $C_Z \sim 0.5$; Huang et al. 2001, Sukoriansky et al. 2002), which contrasts with the isotropic spectrum $E(k) \sim C_K \varepsilon^{2/3} k^{-5/3}$ ($C_K \sim 4 - 6$) in the normal upscale energy cascade. Although $\varepsilon$ is not well established for any of the gas giant planets, rough estimates can be obtained from the eddy-zonal flow conversion rates, $C(K_E,K_Z)$, found by Salyk et al. (2006) and Del Genio et al. (2007a) for Jupiter and Saturn. However, these conversion rates should not be confused with $\varepsilon$ itself, which represents the isotropic spectral energy transfer rate between nearby `shells' of similar $|k|$. Laboratory experiments in regimes approaching zonostrophic conditions (Read et al. 2004, 2007) suggest that $\varepsilon \lesssim 0.2\ C(K_E,K_Z)$, indicating minimum values for $k_\beta$ (non-dimensionalised by planetary radius) of ~70 for Jupiter and ~80 for Saturn. These may be compared with estimates of dimensionless $k_R$ for these planets of ~10-20, indicating a substantial scale separation between $k_\beta$ and that of the jets. This confirms that both Jupiter and Saturn lie well within the zonostrophic regime (Galperin et al. 2006, 2008), with implications for the anisotropic energy transfers within the circulation and the accumulation of kinetic energy into near-barotropic jets.

One further intriguing aspect of the zonostrophic regime is the occurrence of nonlinear Rossby-like traveling waves that do not obey the usual linear Rossby wave dispersion relation (Sukoriansky et al. 2008). These appear to have the character of forced modes, whose phase speeds are controlled by nonlinear interactions with larger amplitude (usually low wavenumber) waves. Their manifestation as unusually slowly-moving Rossby-like waves is reminiscent of the slowly-moving thermal waves identified on Saturn by Achterberg and Flasar (1996) (section 7.4.3), although confirmation of this analogy will need much more detailed diagnostics of the wave flows on Saturn than are available currently.

Several one-layer models have recently shed light on the weather-layer dynamics of Jupiter and Saturn in the presence of static stability (i.e. finite Rossby deformation radius $L_d$). Showman (2007) and Scott and Polvani (2007) performed forced-dissipative studies using the one-layer shallow-water equations, which govern the evolution of a thin layer of constant-density fluid on a sphere (intended to represent the weather-layer in the 1.5 layer formulation; see Dowling and Ingersoll 1989). Showman (2007) forced the flow by episodically injecting isolated mass pulses, intended to represent the effects of episodic thunderstorms that transport mass into the weather layer. Damping, intended to mimic radiation, consisted of Newtonian relaxation that removed available potential energy by flattening the shallow-water layer. Scott and Polvani (2007), following earlier 2D studies, forced the flow by injecting turbulence randomly everywhere simultaneously; for damping they explored both frictional drag and radiative relaxation of layer thickness. Despite the differences in the formulation, both studies find that small $L_d$ (less than a few thousand km) suppresses the $\beta$ effect, leading to the production of numerous vortices rather than jets. This is consistent with one-layer studies using the simpler quasigeostrophic (QG) equations (Okuno and Masuda 2003; Smith 2004; Theiss 2004). Because $L_d$ decreases with increasing latitude (an effect of increasing Coriolis parameter), a critical latitude typically exists below which the flow is jet-dominated and above which the flow is vortex dominated.

In contrast, Li et al. (2006) performed a one-layer QG study on a $\beta$ plane, and found that multiple jets formed over a wide range of deformation radii and other parameters. The reasons for the differences are unclear. As in Showman (2007), forcing by moist convection in this study is represented by the injection of mass pulses that create local negative vorticity sources; these are balanced by a positive vorticity source associated with uniform radiative cooling. Perhaps the major difference is that mass is injected randomly in space in the Showman (2007) simulations, while in Li et al. (2006) mass pulses are triggered only when the thickness of the weather layer decreases below a threshold value. This restricts the convective source to cyclonic shear regions, as is observed on Jupiter and to some extent on Saturn (section 7.4.2), and in some sense mimics the effect that organization of low-level convergence and divergence by the mean meridional circulation would have in a 3-D

model. Anticyclonic vortices have been observed in the vicinity of convective outflow on Saturn (Porco et al. 2005), although imaging sequences do not yet show evidence that such features give up energy to the mean flow (Del Genio et al. 2007a).

In the forced shallow-water studies of Showman (2007) and Scott and Polvani (2007), like that of previous freely evolving shallow-water studies (Cho and Polvani 1996; Iacono et al. 1999; Peltier and Stuhne 2002), the equatorial jet is westward in the Jovian/Saturnian regime of small deformation radius and Rossby number. This behavior has long been considered a failing of the shallow-water model as applied to Jupiter and Saturn (Vasavada and Showman 2005). Recently, however, Scott and Polvani (2008) presented shallow-water simulations, forced by injection of small-scale turbulence and damped by large-scale radiative relaxation, that develop a superrotation analogous to that observed on Jupiter and Saturn. Within the context of their simulations, this result is robust and occurred over a wide range of deformation radii. Scott and Polvani (2008) suggest that the emergence of superrotation may be favored when the adopted damping is radiative relaxation rather than frictional drag. Nevertheless, the result is puzzling, because the simulations of Showman (2007) always developed equatorial subrotation despite the usage of a radiative damping. Further work is needed to resolve the issue.

Sayanagi et al. (2008) performed an idealized study, using the primitive equations, of 3D decaying stably stratified turbulence on a $\beta$ plane. The motivation was to determine whether Jupiter- and Saturn-like jets form in 3D and investigate whether a small deformation radius can suppress jet formation in 3D as it can in the one-layer QG and shallow-water systems. The simulations showed, under conditions relevant to Jupiter and Saturn, that jets can indeed form. If the first-baroclinic deformation radius was substantially smaller than the barotropic Rhines scale $\pi(U/\beta)^{1/2}$, jet formation was inhibited, consistent with the one-layer studies. Interestingly, the simulations also showed that the jets became vertically coherent over a vertical length scale $Lf/N$, where $L$ is the latitudinal width of the jets. This result is consistent with the scaling proposed by Charney (1971) that the inverse energy cascade is isotropic in three dimensions when the vertical coordinate is multiplied by $N/f$.

Motivated by the possibility that Jupiter and Saturn's jets result from baroclinic instabilities in the cloud layer, Kaspi and Flierl (2007) performed a two-layer QG study driven by imposed temperature contrasts on a $\beta$ plane. The novel aspect here was the use of a shallow-atmosphere positive value of $\beta$ in the top layer and a negative value, relevant for the deep interior, in the bottom layer. The top layer thus represents the shallow weather layer and the bottom layer represents the deep interior (Ingersoll and Pollard [1982] showed that if fluid columns act as Taylor columns that span the entire planet, the spherical geometry leads to a negative value of $\beta$). Kaspi and Flierl (2007) found that the two-beta model promotes baroclinic instability relative to a model with equal beta in both layers; their simulations developed multiple robust zonal jets.

Lian and Showman (2008) presented 3D simulations driven by shallow weather-layer forcing that develop numerous zonal jets similar to those on Jupiter and Saturn. The forcing consisted of latitudinal temperature gradients imposed via Newtonian heating at pressures less than ~10 bars. The shallow temperature contrasts led to baroclinic instabilities that pumped the jets in the weather layer. Intriguingly, as described above, the jets developed deep barotropic components. In the simulations, the weather-layer eddy convergences induce meridional circulation cells that penetrate deeply into the interior, and the east-west Coriolis force acting on this motion pumps the deep jets. In the Jupiter-like cases, typically ~25 jets occurred, similar to observations. In some cases, in agreement with observations, the simulated jets violate the barotropic and Charney-Stern stability criteria, achieving curvatures of the zonal wind with northward distance, $\partial^2 u/\partial y^2$, up to $2\beta$, and a hyperstaircase potential vorticity profile similar to that observed is produced (section 7.3.8). Some simulations also developed a Jupiter-like equatorial superrotation, but only if the forcing was chosen to induce a latitudinal temperature gradient near the equator. A similar response to imposed equatorial forcing had earlier been obtained in the 3-D primitive equation model of Yamazaki et al. (2005).

In Lian and Showman (2008), the Newtonian heating was intended to crudely represent possible latitudinal variations of latent heating, solar-energy absorption, or other cloud-layer heating mechanisms. The latitudinal variation of this heating function was a free parameter, and superrotation only resulted for particular choices of this function. Lian and Showman (2009) extended this work by self-consistently including a simple representation of moist convection and removing arbitrary heating functions. In addition to the momentum, heat, and continuity equations, they solved an equation for the transport of water vapor in the domain. Wherever water vapor was supersaturated, they reduced its abundance to saturation and applied the appropriate latent heating to the temperature equation. No microphysics was included; cloud particles were assumed to rain downward to the bottom of the domain. Radiative cooling was applied evenly throughout. In the simulations, ascending motion leads to supersaturation, which induces latent heating, causing a warming that enhances the ascending motion. In this way, a self-sustaining circulation with horizontal temperature contrasts develops; baroclinic instabilities then induce eddy ac-

celerations that pump multiple east-west jet streams. Intriguingly, for a Jupiter-like simulation with three times solar water, an equatorial superrotation spontaneously develops (Fig. 7.24, left). When Uranus/Neptune cases were explored with 30 times solar water, equatorial *subrotation* occurred, reminiscent of the observed equatorial subrotation on Uranus and Neptune.

Schneider and Liu (2009) performed 3D weather-layer simulations of Jupiter using the dry primitive equations. Their simulations extended to ~3 bars pressure and contained a linear drag poleward of 33° at the base of the model to represent Ohmic dissipation in the deep interior (Liu et al. 2008). Their approach is generally similar to that of Lian and Showman (2009); however, they adopted a simple grey radiative-transfer scheme, imposed an intrinsic flux at the base of the model, and included a convective parameterization that transported thermal energy whenever conditions approached neutrally stable. Schneider and Liu's (2009) simulations developed multiple east-west midlatitude jets (whose speed depends on the strength of the imposed drag) and a Jupiter-like equatorial superrotation. They suggest that the superrotation seen in their simulations results from wave/mean-flow interactions associated with Rossby waves generated by convective events near the equator.

Several advances have occurred over the past several years in 3D simulations of convection in giant planet interiors. Previous 3D convection models adopted relatively thick shells with inner/outer radius ratios typically less than ~0.7, and generally produced only a few very broad jets (Aurnou and Olson 2001; Christensen 2001, 2002). Although these early studies always produced a superrotating equatorial jet, a positive feature, there was a discouraging lack of resemblence between the simulated jet profiles and those observed on Jupiter and Saturn. Recently, however, Heimpel et al. (2005) and Heimpel and Aurnou (2007) performed 3D simulations with much thinner shells (inner/outer radius ratios of 0.85 and 0.9). Like the earlier studies, these simulations are Boussinesq, meaning that they assume a basic-state density that is independent of radius, and have free-slip momentum boundary conditions at both the top and bottom. Interestingly, when the control parameters (Rayleigh and Ekman number) are tuned to obtain a Jupiter-like wind speed, these thin-shell simulations develop a surprisingly Jupiter- and Saturn-like wind profile with a superrotating jet and numerous weaker, midlatitude eastward and westward jets (Fig. 7.24, right). The convective heat fluxes predicted by these models exhibit a minimum at the equator and maxima at the poles, consistent with the observationally inferred latitude variation of internal heat loss (Ingersoll 1976).

These are promising results. Nevertheless, the meaning of the lower boundary in these simulations is unclear. The strong barotropic jets imply the existence of strong horizontal pressure contrasts, which in these models are supported by the impermeable lower boundary. On Jupiter and Saturn, however, there is no internal boundary that could support such pressure variations. Instead, the jets would need to decay with depth before reaching the metallic region, implying the existence in the molecular envelope of thermal-wind shear that would require large lateral density contrasts to support. It is not obvious whether there exists any mechanism to produce such density contrasts (Liu et al. 2008). An alternate study that adopts a no-slip boundary condition at the bottom, perhaps more relevant to the magnetohydrodyanamic drag expected there, develops a rapid equatorial jet but very weak mid- and high-latitude jets (Aurnou and Heimpel 2004). This suggests that explaining Jupiter and Saturn's mid- and high-latitude jets in the deep-convection models may be problematic.

The superrotating equatorial jet in the 3D Boussinesq simulations of Aurnou and Olson (2001), Christensen (2001, 2002), Heimpel et al. (2005), and Heimpel and Aurnou (2007) results from the interaction of columnar convective rolls with the curving spherical planetary surface (Busse 2002; Vasavada and Showman 2005). This mechanism, which can be viewed as a ``topographic'' $\beta$ effect, requires convective rolls that act as coherent Taylor columns (i.e., the convective rolls must remain coherent along their entire length from the northern to the southern boundary). As Glatzmaier et al. (2009) point out, current 3D convection studies are relatively laminar (a result of the low resolution necessary in a 3D study), which - combined with the fact that the simulated convective structures are relatively large-scale - promotes such columnar coherence. In reality, convective plumes are probably much narrower than current models can resolve; because of their small scales, such plumes are less likely to be geostrophic and thus may not exhibit the columnar structure necessary for the topographic $\beta$ effect to occur.[2]

Instead, Glatzmaier et al. (2009) propose that equatorial superrotation on Jupiter and Saturn results from the interaction of convection with the radial density gradient (an effect that is ignored in the Boussinesq models). On Jupiter and Saturn, the density varies by a factor of ~1000 from the cloud layer to the deep interior, and most of this density variation occurs near

[2] The *jets*, however, are large scale and should still exhibit a relatively columnar structure, since the Taylor-Proudman theorem applies to a geostrophically balanced, barotropic fluid regardless of whether the density varies with radius.

the surface. As a rising plume expands, it spins up anticyclonically, leading to a wavelike behavior that propagates eastward, with faster eastward propagation for fluid elements farther from the rotation axis. This radial dependence of the eastward propagation speed causes an eastward tilt in ascending convective plumes and a westward tilt in descending convective plumes (Glatzmaier et al. 2009). The Reynolds stresses acting on such tilted convective columns transport eastward momentum radially outward and westward momentum radially inward (Busse 2002; Vasavada and Showman 2005; Glatzmaier et al. 2009), leading to differential rotation with a superrotating jet at the equatorial surface. The advantage of this mechanism over the topographic $\beta$ effect is that it is *local* and does not require convective columns to span the entire planet as a Taylor column. Evonuk and Glatzmaier (2006, 2007), Evonuk (2008), and Glatzmaier et al. (2009) presented 2D numerical simulations in the equatorial plane to confirm these qualitative arguments. However, a possible stumbling block for this mechanism is that it would also predict equatorial superrotation on Uranus and Neptune, where equatorial subrotation is observed instead.

### *7.5.4 Do the observations constrain our models?*

The most basic observational constraints to be met by any model of jet formation are the observed profiles of zonal wind and temperature with latitude in the upper troposphere; specifically, the existence of a strong superrotating equatorial jet, numerous weaker high-latitude jets, and meridional temperature variations of only a few K. Recent numerical models have made significant advances in matching these constraints. Three independent shallow-atmosphere models now exist that, under Jupiter- and Saturn-like conditions, spontaneously produce multiple midlatitude jets and a strong superrotating equatorial jet similar to those on Jupiter or Saturn - the one-layer shallow-water model of Scott and Polvani (2008) and the 3D primitive-equation models of Lian and Showman (2009) and Schneider and Liu (2009). In contrast to some previous shallow-atmosphere studies, these models produce equatorial superrotation naturally, without ad-hoc forcing functions. Likewise, in the deep-convection arena, Boussinesq models in a thin shell (Heimpel et al. 2005; Heimpel and Aurnou 2007) show promise in explaining not only the equatorial superrotation (long a strength of the deep-convective models) but also the alternating midlatitude jets (something that thick-shell convection models had previously failed to do). Nevertheless, many areas for improvement remain in both classes of models, and the approaches must ultimately be merged if we are to obtain a full understanding of the general circulation within giant planets.

Other observational constraints also exist. Cloud tracking has allowed estimation of the horizontal eddy-momentum fluxes $u'v'$; these results imply that eddies pump momentum up-gradient into the jets on both Saturn and Jupiter (Del Genio et al. 2007a; Salyk et al. 2006; section 7.3.3). Given the observed $u'v'$ values, the power per unit area associated with the conversion of eddy to zonal mean kinetic energy would exceed Saturn's luminosity if the fluxes extended beyond ~2 bars; thus, these eddies (or at least the accelerations they induce) appear to be truly shallow. Even then, the implied kinetic energy fluxes approach ~1 W $m^{-2}$, which is a substantial fraction of the total energy available for doing work. These results imply that the baroclinic atmosphere cannot be neglected when modeling jet pumping on the giant planets.

What is the process responsible for producing these jet-pumping eddies? Histograms of the $u'v'$ values at particular latitudes on jet flanks show that the distribution peaks around zero, with long tails at both positive and negative $u'v'$, but that the distribution is skewed such that the positive tail dominates on the south flanks of eastward jets and the negative tail dominates on the north flanks of eastward jets (Fig. 7.25, left). Such a skewed distribution implies that, *on average*, eddies pump momentum up-gradient into jet cores. Interestingly, shallow-atmosphere models driven by baroclinic instabilities in the weather layer explain these distributions surprisingly well (Lian and Showman 2008; Fig. 7.25, right). This agreement supports the possibility that baroclinic instabilities pump the jets at cloud level. However, other cloud-level sources of turbulence, such as thunderstorms, might be capable of generating the observed fluxes. Indeed laboratory studies of geostrophic turbulence on a β-plane, dominated either by baroclinic instabilities (Bastin and Read 1998; Wordsworth et al. 2008) *or* unstably-stratified convection (Condie and Rhines 1994; Read et al. 2004, 2007), show a strong tendency to develop eddy-driven barotropic jets, so the question as to which process dominates on the gas giant planets must remain open until further evidence on the respective characteristics of baroclinic instability and deep convection becomes available.

## 7.6 Discussion

Our current tentative understanding of Saturn's atmospheric thermal structure and circulation, based on direct measurements and inferences from Cassini data, can be summarized as follows. Moist adiabatic ascent, radiative cooling aloft, and compensating dry adiabatic descent produce a reversal of the meridional temperature gradient between the water cloud level and the upper troposphere, such that cyclonic regions are cool and anti-cyclonic regions warm near the water cloud base while the opposite is true near and above the visible clouds (Showman and de Pater 2005). Between the water condensation level and the level of reversal of *dT/dy*, zonal winds should strengthen with height according to the thermal wind equation. Above this level, the thermal wind decays with height as observed by CIRS down to at least 800 mb. Since VIMS-derived winds are slightly stronger than ISS-derived winds, the reversal of *dT/dy* probably occurs below the ammonium hydrosulfide condensation level. The meridional circulation reverses sign at a somewhat higher level, near the altitude sensed in ISS images.

Despite this more comprehensive emerging picture, many questions still remain. Whether the zonal winds strengthen, decay, or remain constant down to and below the (still unknown) water cloud level is still unknown. How the inferred circulation relates to near-infrared continuum and 5 μm cloud patterns on Saturn, and why the wind-albedo correlation differs from that on Jupiter, is still uncertain. Which class of candidate mechanisms (or what combination of them) drives the observed cloud level circulation at different latitudes is yet to be determined. The eddy process that forces the mechanically driven upper troposphere circulation is also not certain. Seasonal variability is already evident near the tropopause and in the stratosphere, but the Cassini dataset itself only covers a small fraction of a Saturn year. The actual strength of Saturn's prograde equatorial jet, the reason it exists, and its more temporally variable nature relative to other latitudes, remain a mystery. Below we describe advances that we anticipate taking place in the modeling arena to more fully exploit the Cassini dataset and suggest observational strategies that could address many of the remaining questions.

### *7.6.1 Future modeling directions*

Modeling of the dynamics of the gas giant planets has progressed tremendously in a short time, due both to increases in computing power and an emerging understanding of the required physics. To continue moving forward, the major weaknesses of each class of models must be addressed. Idealized models have contributed to understanding of the inverse cascade, the significance of the Rhines scale, and the conditions required for a prograde equatorial jet. The next step must be to identify and simulate the specific forcing and dissipation mechanisms responsible for the behavior seen in these models. Shallow weather layer models, which depend on moist convection as either the direct source of eddies that maintain the flow or the generator of temperature gradients that drive baroclinic instability, must begin to implement state-of-the-art cumulus parameterizations to become credible. Cumulus parameterization is itself a topic of active research, and the adaptation of such models for Saturn would benefit from the further use of cloud-resolving models (Hueso and Sánchez-Lavega 2004) to explore different assumptions about the cloud microphysics and background thermodynamic structure. Current shallow weather layer models are hydrostatic, which limits their ability to realistically portray the dynamical coupling between the visible cloud level and water condensation level, which are separated by a thick near-adiabatic layer. Global non-hydrostatic fine resolution models are imminent in Earth atmospheric science and ultimately should be pursued for the gas giants as computing power increases.

The deep convective cylinder class of models is even more computationally challenging because they simulate a much greater depth of the atmosphere. They are also limited by our lack of knowledge of the interiors of gas giant planets. The central questions that have emerged for these models are the depth to which the cylindrical configuration and the associated zonal flow extends and the physics that determines this lower boundary. Two research directions must be pursued to address these issues. First, most cylinder models are Boussinesq for computational convenience. 2-D simulations that relax this assumption produce distinctly different behavior of the convective plumes and suggest that some of the theoretical difficulties of the cylinder approach may be overcome in the presence of realistic stratification (Glatzmaier et al. 2009), but eventually it must become possible to conduct such simulations in 3-D to determine whether these ideas are truly viable. Second, fully 3-D magnetohydrodynamic simulations will be required to settle the issue of Ohmic dissipation constraints on the inner cylinder radius.

To date, simulations of Saturn's stratosphere have been largely restricted to 1-D chemistry-diffusion models, from which zeroth-order inferences about the dynamics could be made (Moses and Greathouse 2005). These are beginning to give way to 2-D interactive chemistry-dynamics models, which will be better positioned to provide insights into relationships seen in the CIRS and IRTF datasets. Already such models have raised questions about the processes that produce the differing latitudinal profiles of $C_2H_6$ and $C_2H_2$ on Saturn (Moses et al. 2007; see Chapter 6). However, even 2D models must be utilized with care, since 3D eddies can substantially influence the strength and direction of tracer transport in the zonal mean. Although 2D transport models can include a parameterization of such eddy transports, such as through the Transformed Lagrangian Mean approximation (e.g. Andrews et al. 1987), the accurate representation of fully 3D transport needs a fully 3D model. So a long term goal should be to adapt fully 3D general circulation models to incorporate interactive chemistry, much as is being developed by the terrestrial atmosphere modeling community.

The Cassini mission has provided a series of observational constraints that any model must satisfy. In addition to zonal wind profiles and temperature patterns, any viable model must also simulate other indices of the flow such as the distribution of convective clouds and disequilibrium gas concentrations, meridional and vertical velocity patterns, and process-level diagnostics such as potential vorticity and eddy momentum fluxes. Many published giant planet model simulations are limited in their diagnosis of the structure of the circulation and the energy and momentum balances that produce it, thus making it difficult to evaluate them. Future modeling studies should propose observables that would be indicative of the mechanisms at work on the gas giant planets as input for the remote sensing community to develop an effective strategy for future exploration.

### *7.6.2 Long-term observational needs*

Many of our questions about Saturn's upper troposphere and stratosphere center on the role of seasonal forcing and will thus benefit greatly by observing at different points in the seasonal cycle. The Cassini Equinox mission should be sufficient to detect hemispheric shifts in the tropospheric haze and the response of the near-tropopause temperature structure to such changes. A potential Cassini Solstice mission extension would allow us to view seasonal shifts in the stratospheric meridional circulation and to detect downward propagation of temperature and wind anomalies that are the signature of the semi-annual and quasi-biennial oscillations on Earth, if such behavior exists on Saturn.

At lower altitudes, most questions concern the structure and dynamics of the atmosphere below the visible cloud level. For Jupiter, NASA's Juno mission, scheduled to launch in 2011 and enter Jupiter orbit in 2016, will provide key constraints on the depth to which the jets extend below the clouds. For Saturn, the Cassini orbital configuration precludes such measurements because the orbit is quasi-equatorial and much too far from Saturn. However, end-of-mission scenarios under consideration would place Cassini in a highly inclined orbit with a periapse close to Saturn (below the rings), allowing the final mission phase to provide Juno-like constraints on the depth of Saturn's jets as well. Although caution will be needed in interpreting the results in terms of deep-or-shallow jet forcing (Showman et al. 2006; Vasavada and Showman 2005), such observations will nevertheless provide invaluable constraints for understanding the general circulation and the mechanisms of jet maintenance. Detailed measurements of the magnetic field at this time may also help constrain Saturn's actual deep interior rotation period.

The key feature of Juno for atmospheric dynamics is its multi-channel microwave radiometer, which will sound the water vapor profile down to about 100 bars. These observations will not only determine Jupiter's water abundance (by approximately locating the condensation level) but will also distinguish water vapor amounts in belts and zones and thereby constrain the moisture convergence/divergence at depth that we postulate to exist on the gas giants (Fig. 7.18). This information for Jupiter will obviously have ramifications for Saturn as well. However, intriguing differences in the pattern of moist convection on the two planets exist: On Jupiter convection is restricted to cyclonic shear regions (Porco et al. 2003), while on Saturn convective clouds (including some of the most vigorous storms) also appear in westward and eastward jets. Thus, in the long term, microwave radiometer water profiling of Saturn would be desirable. An alternative is a Saturn Multi-Probes Mission (Atreya 2003), which could sample both cyclonic and anti-cyclonic temperate regions on Saturn, with a possible third probe entering the apparently distinct equatorial region. Probes are less desirable than orbiters because they provide a sparse and potentially non-representative sample, as was the case for Galileo. Their advantage, however, is high vertical resolution,

including the chance to detect and measure the strength of the hypothesized stable layer at depth that water condensation would create, which is crucial to shallow weather layer theories of driving the cloud level flow.

Eventually, active remote sensing must become viable for the giant planets. On Earth, lidars and millimeter cloud radars allow the thinnest hazes to be detected and precisely located in altitude and the thickest cloud systems to be profiled from top to bottom (Stephens et al. 2002). On Saturn, such instruments could accurately characterize the stratospheric and tropospheric hazes, determine the ammonia cloud top, definitively detect the ammonium hydrosulfide layer that to this point exists only in theory, and most importantly, characterize the nature of cloud structure at the water cloud level. This would tell us whether there is an extensive water cloud layer at all, as the early thermo-chemical models hypothesized, or whether water condensation is limited to scattered shallow cumulus and occasional deep penetrating cumulonimbus clouds, as is true of Earth's tropics. Active remote sensing is a challenge for the giant planets because of the mass of the instruments and the need for orbits to pass very close to the cloud tops to enhance the spatial resolution. Saturn in turn is more challenging than Jupiter because its water condensation level is likely to be much deeper. Until remote sensing down to the water condensation level and below becomes a reality, however, it will be difficult for the numerous theories of Saturn's general circulation to be regarded as anything more than simply plausible ideas.

**Acknowledgments**

This work was supported by NASA and ESA through the Cassini-Huygens Mission and the NASA Planetary Atmospheres Program. We thank John Barbara and Lilly del Valle for assistance with several figures and two anonymous reviewers for constructive comments.

**References**


Acarretta, J.R., Sánchez-Lavega, A.: Vertical cloud structure in Saturn's 1990 equatorial storm. Icarus **137,** 24-33 (1999)

Achterberg, R.K., Flasar, F.M.: Planetary-scale thermal waves in Saturn's upper troposphere. Icarus **119**, 350-369 (1996)

Aguiar, A.C.B., et al.: A laboratory model of Saturn's north polar hexagon. Icarus, submitted (2009)

Alexander, O'D.A.F.: The Planet Saturn. Faber and Faber, London (1962)

Allison, M.: A similarity model for the windy jovian thermocline. Planet. Space Sci. **48**, 753-774 (2000)

Allison, M., Stone, P.H.: Saturn meteorology: A diagnostic assessment of thin-layer configurations for the zonal flow. Icarus **54**, 296-308 (1983)

Allison, M., Godfrey, D.A., Beebe, R.F.: A wave dynamical interpretation of Saturn's polar hexagon. Science **247**, 1061-1063 (1990)

Allison, M., Del Genio, A.D., Zhou, W.: Richardson number constraints for the Jupiter and outer planet wind regime. Geophys. Res. Letters **22,** 2957-2960 (1995)

Anderson, J.D., Schubert, G.: Saturn's gravitational field, internal rotation, and interior structure, Science 317, 1384-1387 (2007)

Andrews, D. G., Holton, J. R., Leovy, C. B.: Middle Atmosphere Dynamics. Academic Press, New York (1987)

Arnol'd, V.I.: On an a priori estimate in the theory of hydrodynamic stability. Am. Math. Soc. Transl. Ser. 2 **79**, 267-269 (1966)

Atkinson, D.H., Pollack, J.B., Seiff, A.: The Galileo probe Doppler Wind Experiment: Measurement of the deep zonal winds on Jupiter. J. Geophys. Res. **103**, 22,911-22,928 (1998)

Atreya, S.K.: Composition, clouds, and origin of Jupiter's atmosphere – a case for deep multiprobes into giant planets. In Wilson, A. (ed.), Proc. Int. Workshop 'Planetary Probe Atmospheric Entry and Descent Trajectory Analysis and Science', pp. 57-62, ESA SP-544, Noordwijk, Netherlands (2003)

Aurnou, J.M., Olson, P.L.: Strong zonal winds from thermal convection in a rotating spherical shell. Geophys. Res. Lett. **28**, 2557-2559 (2001)

Aurnou, J.M., Heimpel, M.H.: Zonal jets in rotating convection with mixed mechanical boundary conditions. Icarus **169**, 492-498 (2004)

Bagenal, F.: A new spin on Saturn's rotation. Science **316**, 380-381 (2007)

Baines, K.H., et al.: The atmospheres of Saturn and Titan in the near-infrared: First results of Cassini/VIMS. Earth, Moon, Plan. **96**, 119-147 (2005)

Baines, K.H., et al.: To the depths of Venus: Exploring the deep atmosphere and surface of our sister world with Venus Express. Planet. Space Sci. **54**, 1263-1278 (2006)

Baines, K.H., et al.: Saturn's north polar cyclone and hexagon at depth revealed by Cassini/VIMS. Planet. Space Sci., submitted (2009a)

Baines, K.H., et al.: Storm clouds on Saturn: Lightning-induced chemistry and associated materials consistent with Cassini/VIMS spectra. Planet. Space Sci., submitted (2009b)

Baines, K.H., et al.: The deep clouds of Saturn: Morphology, spatial distribution, and dynamical implications as revealed by Cassini/VIMS. Icarus, submitted (2009c)

Baldwin, M.P., et al.: The quasi-biennial oscillation. Rev. Geophys. **39**, 179-229 (2001)

Barnet, C.D., Beebe, R.F., Conrath, B.J: A seasonal radiative-dynamic model of Saturn's troposphere. Icarus **98**, 94-107 (1992)

Bastin, M.E., Read, P.L.: Experiments on the structure of baroclinic waves and zonal jets in an internally heated rotating cylinder of fluid. Phys. Fluids **10**, 374-389 (1998)

Beebe, R.F., et al.: The onset and growth of the 1990 equatorial disturbance on Saturn. Icarus **95**, 163-17 (1992)

Bézard, B., Gautier, D., Conrath, B: A seasonal model of the Saturnian upper troposphere: Comparison with Voyager infrared measurements. Icarus **60**, 274-288 (1984)

Bézard, B., Gautier, D.: A seasonal climate model of the atmospheres of the giant planets at the Voyager encounter time. Icarus **61**, 296-310 (1985)

Brown, R.H., et al.: The Cassini visual and infrared mapping spectrometer (VIMS) investigation. Space Sci. Rev. **115**, 111-168 (2004)

Busse, F.H.: Convective flows in rapidly rotating spheres and their dynamo action. Phys. Fluids **14**, 1301-1314 (2002)

Caldwell, J., et al.: The drift of Saturn's north polar spot observed by the Hubble Space Telescope. Science **260**, 326-329 (1993)

Carlson, B.E., Rossow, W.B., Orton, G.S.: Cloud microphysics of the giant planets. J. Atmos. Sci. **45**, 2066-2081 (1988)

Cess, R.D., Caldwell, J.: A Saturnian stratospheric seasonal climate model. Icarus **38**, 349-35, (1979)

Charney, J.G.: Geostrophic turbulence. J. Atmos. Sci. **28**, 1087-1095 (1971)

Charney, J. G.,, Drazin, P. G.: Propagation of planetary-scale disturbances from the lower into the upper atmosphere, J. Geophys. Res. **66**, 83-109 (1961)

Cho, J.Y.-K., Polvani, L.M.: The emergence of jets and vortices in freely evolving, shallow-water turbulence on a sphere. Phys. Fluids **8**, 1531-1552 (1996)

Choi, D.S., Showman, A.P., Brown,, R.H.: Cloud features and zonal wind measurements of Saturn's atmosphere as observed by Cassini/VIMS. J. Geophys. Res., doi:10.1029/2008JE003254, in press (2009)

Christensen, U.R.: Zonal flow driven by deep convection in the major planets. Geophys. Res. Lett. **28**, 2553-2556 (2001)

Christensen, U.R.: Zonal flow driven by strongly supercritical convection in rotating spherical shells. J. Fluid Mech. **470**, 115-133 (2002)

Condie, S. A., Rhines, P. B.: A convective model for the zonal jets in the atmospheres of Jupiter and Saturn. Nature **367**, 711-713 (1994)

Conrath, B.J., Gierasch, P.J.: Global variation of the *para* hydrogen fraction in Jupiter's atmosphere and implications for dynamics on the outer planets. Icarus **57**, 184-204 (1984)

Conrath, B.J., Pirraglia, J.A.: Thermal structure of Saturn from Voyager infrared measurements: Implications for atmospheric dynamics. Icarus **53**, 286-292 (1983)

Conrath, B.J., Gierasch, P.J., Leroy, S.S.: Temperature and circulation in the stratosphere of the outer planets. Icarus **83**, 255-281 (1990)

Conrath, B.J., Gierasch, P.J., Ustinov, E.A.: Thermal structure and para hydrogen fraction on the outer planets from Voyager IRIS measurements. Icarus **135**, 501-517 (1998)

Del Genio, A.D., McGrattan, K.B.: Moist convection and the vertical structure and water abundance of Jupiter's atmosphere. Icarus **84**, 29-53 (1990)

Del Genio, A.D., et al.: Saturn eddy momentum fluxes and convection: First estimates from Cassini images, Icarus **189**, 479–492 (2007a)

Del Genio, A.D., Yao, M.-S., Jonas, J.: Will moist convection be stronger in a warmer climate? Geophys. Res. Lett. **34**, L16703, doi:10.1029/2007GL030525 (2007b).
Derbyshire, S.H., et al.: Sensitivity of moist convection to environmental humidity. Quart. J. Roy. Meteor. Soc. **130**, 3055-3079 (2004)
Desch, M.D., Kaiser,M.L.: Voyager measurement of the rotation period of Saturn's magnetic field. Geophys. Res. Lett. **8**, 253-256 (1981)
Dowling, T. E.: Dynamics of Jovian atmospheres, Ann. Rev. Fluid Mech., **27**, 293-334 (1995)
Dowling, T. E., Ingersoll, A.P.: Potential vorticity and layer thickness variations in the flow around Jupiter's Great Red Spot and White Oval BC. J. Atmos. Sci. **45**, 1380–1396 (1988)
Dowling, T. E., Ingersoll, A.P.: Jupiter's Great Red Spot as a shallow water system. J. Atmos. Sci. **46**, 3256–3278 (1989)
Drossart, P.D.: Scientific goals for the observation of Venus by VIRTIS on ESA/Venus Express mission. Planet. Space Sci. **55**, 1653-1672 (2007)
Dunkerton, T.: On the mean meridional mass motions of the stratosphere and mesosphere, J. Atmos. Sci. **35**, 2325-2333 (1978)
Dyudina, U.A., et al.: Lightning storms on Saturn observed by Cassini ISS and RPWS during 2004-2006. Icarus **190**, 545-555 (2007)
Dyudina, U.A., et al.: Dynamics of Saturn's south polar vortex. Science **319**, 1081 (2008a)
Dyudina, U.A., et al.: Saturn's south polar vortex compared to other large vortices in the solar system. Icarus, doi:10.1016/j.icarus.2009.02.014, in press (2009)
Elachi, C., et al.: RADAR: The Cassini Titan radar mapper. Space Sci. Rev. **115**, 71-110 (2004)
Eliassen, A., Palm, E.: On the transfer of energy in stationary mountain waves, Geophys. Publ. **22**(3), 1-23 (1961)
Emanuel, K.: Tropical cyclones. Annu. Rev. Earth Planet. Sci. **31**, 75-104 (2003)
Evonuk, M., Glatzmaier, G.A.: A 2D study of the effects of the size of a solid core on the equatorial flow in giant planets. Icarus **181**, 458-464 (2006)
Evonuk, M., Glatzmaier, G.A.: The effects of rotation rate on deep convection in giant planets with small solid cores. Planet. Space Sci. **55**, 407-412 (2007)
Evonuk, M.: The role of density stratification in generating zonal flow structures in a rotating fluid. Astrophys. J. **673**, 1154-1159 (2008)
Fischer, G., et al.: Saturn lightning recorded by Cassini/RPWS in 2004. Icarus **183**, 135-152 (2006)
Fischer, G., et al.: Analysis of a giant lightning storm on Saturn. Icarus **190**, 528-544 (2007)
Flasar, F.M., et al.: An intense stratospheric jet on Jupiter. Nature **427**, 132-135 (2004)
Flasar, F.M., et al.: Exploring the Saturn system in the thermal infrared: The composite infrared spectrometer. Space Sci. Rev. **115**, 169-297 (2004)
Flasar, F.M., et al.: Temperatures, winds and composition in the Saturnian system. Science **307**, 1247-1251 (2005)
Fletcher, L.N., et al.: The meridional phosphine distribution in Saturn's upper troposphere from Cassini/CIRS observations. Icarus, **188**, 72-88 (2007a)
Fletcher, L.N., et al.: Characterising Saturn's vertical temperature structure from Cassini/CIRS. Icarus **189**, 457-478 (2007b)
Fletcher, L.N., et al.: Saturn's atmosphere: Structure and composition from Cassini/CIRS. Ph.D. dissertation, University of Oxford, UK (2007c)
Fletcher, L.N., et al.: Temperature and composition of Saturn's polar hot spots and hexagon. Science **319**, 79-81 (2008)
Fouchet, T., et al.: An equatorial oscillation in Saturn's middle atmosphere. Nature **453**, 200-202 (2008)
Fouchet, T., et al.: Saturn composition and chemistry. Chapter 6, this book (2009)
Friedson, A.J.: New observations and modeling of a QBO-like oscillation in Jupiter's stratosphere. Icarus **137**, 34-55 (1999)
Frierson, D.M.W.: Midlatitude static stability in simple and comprehensive general circulation models. J. Atmos. Sci. **65**, 1049-1062 (2008)
Fruh, W.-G. , Read, P. L.: Experiments on a barotropic rotating shear layer. Part 1. Instability and steady vortices, J. Fluid Mech.. **383**, 143-173 (1999)
Galopeau, P.H.M., Lecacheux, A.: Variations of Saturn's radio period measured at kilometer wavelengths. J. Geophys. Res. **105**, 13,089-13,102 (2000)
Galperin, B., et al.: Anisotropic turbulence and zonal jets in rotating flows with a β-effect. Nonlin. Processes Geophys. **13**, 83–98 (2006)
Galperin, B., Sukoriansky, S., Dikovskaya, N.: Zonostrophic turbulence. Physica Scripta **T132** 014034, doi:10.1088/0031-8949/2008/T132/014034n(2008)
García-Melendo, E., Sánchez-Lavega, A., Hueso, R.: Numerical models of Saturn's long-lived anticyclones, Icarus **191,** 665-677 (2007)
García-Melendo, E., et al.: Vertical shears in Saturn's eastward jets at cloud level. Icarus, doi: 10.1016/j.icarus.2009.02.022, in press (2009)
Gezari, D.Y., et al.: New features in Saturn's atmosphere revealed by high-resolution thermal images. Nature **342**, 777-780 (1989)
Gierasch, P.J.: Jovian meteorology: Large-scale moist convection. Icarus **29,** 445-454 (1976)
Gierasch, P.J.: Radiative-convective latitudinal gradients for Jupiter and Saturn models with a radiative zone. Icarus **142**, 148-154 (1999)
Gierasch, P.J., Conrath, B.J., Magalhães, J.A.: Zonal mean properties of Jupiter's upper troposphere from Voyager infrared observations. Icarus **67**, 456-483 (1986)
Gierasch, P.J., et al.: Observation of moist convection in Jupiter's atmosphere. Nature **403**, 628-630 (2000)
Gierasch, P.J., Conrath, B.J., Read, P.L.: Nonconservation of Ertel potential vorticity in hydrogen atmospheres. J. Atmos. Sci. **61**, 1953-1965 (2004)
Gillet, F. C., Orton, G. S.: Center-to-limb observations of Saturn in the thermal infrared. Astrophys. J. **195**, L47-L49 (1975)
Glatzmaier, G.A.: A note on "Constraints on deep-seated zonal winds inside Jupiter and Saturn." Icarus **196**, 665-666 (2008)
Glatzmaier, G.A., Evonuk, M., Rogers, T.M.: Differential rotation in giant planets maintained by density-stratified turbulent convection. Geophys. Astrophys. Fluid Dyn **103**., 31-51 (2009)
Godfrey, D.A.: A hexagonal feature around Saturn's north pole. Icarus **76**, 335–356 (1988)
Godfrey, D.A.: The rotation period of Saturn's polar hexagon. Science **247**, 1206-1207 (1990)
Godfrey, D.A., Moore, V.: The saturnian ribbon feature – A baroclinically unstable model. Icarus **68**, 313-343 (1986)
Greathouse, T.K., et al.: Meridional variations of temperature, $C_2H_2$ and $C_2H_6$ abundances in Saturn's stratosphere at southern summer solstice. Icarus **177**, 18-31 (2005)
Grote, E., Busse, F.H., Tilgner, A.: Regular and chaotic spherical dynamos. Phys. Earth Planet Int. **117**, 259-272 (2000)
Guillot, T.: Interiors of giant planets inside and outside the solar system. Science **286**, 72-77 (1999)
Guillot, T.: The interiors of giant planets: Models and outstanding questions. Ann. Rev. Earth Planet. Sci. **33**, 493-530 (2005)
Guillot, T., et al.: Are the giant planets fully convective? Icarus **112**, 354-367 (1994)

Gurnett, D.A., et al.: Radio and plasma wave observations at Saturn from Cassini's approach and first orbit. Science **307**, 1255-1259 (2005)
Gurnett, D.A., et al.: The variable rotation period of the inner region of Saturn's plasma disk. Science **316**, 442-445 (2007)
Hamilton, K.: Dynamics of the tropical middle atmosphere: A tutorial review. Atmos.-Ocean **36**, 319-354 (1998)
Hanel, R., et al.: Infrared observations of the Saturnian system from Voyager 1. Science **212**, 192-200 (1981)
Hanel, R.A., et al.: Albedo, internal heat flux, and energy balance of Saturn. Icarus **53**, 262-285 (1983)
Hartmann, D. L.: The general circulation of the atmosphere and its variability. J. Meteor. Soc. Japan **85B**, 123-143 (2007)
Heimpel, M., Aurnou, J., Wicht, J.: Simulation of equatorial and high-latitude jets on Jupiter in a deep convection model. Nature **438**, 193-196 (2005)
Heimpel, M., Aurnou, J.: Turbulent convection in rapidly rotating spherical shells: A model for equatorial and high latitude jets on Jupiter and Saturn. Icarus **187**, 540-557 (2007)
Held, I.M., Andrews, D.G.: On the direction of the eddy momentum flux in baroclinic instability. J. Atmos. Sci. **40**, 2220-2231 (1983)
Hesman, B.E., et al.: Saturn's latitudinal $C_2H_2$ and $C_2H_6$ abundance profiles from Cassini/CIRS and graound-based observations. Icarus, doi:10.1016/j.icarus.2009.02.013, in press (2009)
Hess, S.L., Panofsky, H.A.: The atmospheres of the other planets. In Malone, T.F. (ed.), Compendium of Meteorology, pp. 391-400, Amer. Meteor. Soc., Boston (1951)
Hide, R., Lewis, S.R., Read, P.L.: Sloping convection: A paradigm for large-scale waves and eddies in planetary atmospheres? Chaos **4**, 135-162 (1994)
Howard, L. N., Drazln, P. G.: On instability of parallel flow of inviscid fluid in a rotating system with variable Coriolis parameter. J. Math. Phys. N **43**, 83-99 (1964)
Huang, H.-P., Galperin, B., Sukoriansky, S.: Anisotropic spectra in two-dimensional turbulence on the surface of a rotating sphere. Phys. Fluids **13**, 225-240 (2001)
Hubbard, W., et al.: Interior of Saturn. Chapter 5, this book (2009)
Hueso, R., Sánchez-Lavega, A.: A three-dimensional model of moist convection for the giant planets. II. Saturn's water and ammonia moist convective storms. Icarus **172**, 255-271 (2004)
Hunt, G.E., et al.: Dynamical features in the northern hemisphere of Saturn from Voyager 1 images. Nature **297**, 132-134 (1982)
Iacono, R., Struglia, M.V., Roncji, C.: Spontaneous formation of equatorial jets in freely decaying shallow water turbulence. Phys. Fluids **11**, 1272-1274 (1999)
Ingersoll, A.P.: Pioneer 10 and 11 observations and the dynamics of Jupiter's atmosphere. Icarus **29**, 245-253 (1976)
Ingersoll, A.P., Cuzzi, J.N.: Dynamics of Jupiter's cloud bands. J. Atmos. Sci, **26**, 981-985 (1969)
Ingersoll, A.P., Pollard, D.: Motion in the interiors and atmospheres of Jupiter and Saturn: Scale analysis, anelastic equations, barotropic-stability criterion. Icarus **52**, 62-80 (1982)
Ingersoll, A.P., Porco, C.C.: Solar heating and internal heat flow on Jupiter. Icarus **35**, 27-43 (1978)
Ingersoll, A.P., et al.: Structure and dynamics of Saturn's atmosphere. In Gehrels, T., Matthews, M.S. (eds.), Saturn, pp. 195-238. U.of Arizona Press, Tucson (1984)
Ingersoll, A.P., et al.: Moist convection as the energy source for the large-scale motions in Jupiter's atmosphere. Nature **403**, 630-631 (2000)
Ingersoll, A.P., et al.: Dynamics of Jupiter's atmosphere. In Bagenal, F., et al. (eds.), Jupiter: The Planet, Satellites, and Magnetosphere, pp. 105-128. Cambridge U. Press, New York (2004)
Janssen, M.A., Allison, M., Lorenz, R.D.: Saturn's thermal emission at 2-cm wavelength and implications for atmospheric composition and dynamics. Poster, Saturn After Cassini-Huygens Symposium, London, UK (2008)
Kaiser, M.L., Connerney, J.E.P., Desch, M.D.: Atmospheric storm explanation of saturnian electrostatic discharges. Nature **303**, 50-53 (1983)
Karkoschka, E., Tomasko, M.G.: Saturn's upper troposphere 1986-1989. Icarus **97**, 161-181 (1992)
Karkoschka, E., Tomasko, M.: Saturn's vertical and latitudinal cloud structure 1991-2004 from HST imaging in 30 filters. Icarus **179**, 195-221 (2005)
Kaspi, Y., Flierl, G.R.: Formation of jets by baroclinic instability on gas planet atmospheres. J. Atmos. Sci. **64**, 3177-3194 (2007)
Kirk, R.L., Stevenson, D.J.: Hydromagnetic implications of zonal flows in the giant planets. Astrophys. J. **316**, 836-846 (1987)
Kurth, W.S., et al.: A Saturnian longitude system based on a variable kilometric radiation period. Geophys. Res. Lett. **34**, L02201, doi:10.1029/2006GL028336 (2007)
Kurth, W.S., et al.: An update to a Saturnian longitude system based on kilometric radio emissions. J. Geophys. Res. **113**, A05222, doi:10.1029/2007JA012861 (2008)
Leovy, C.B., Friedson, A.J., Orton, G.S.: The quasiquadrennial oscillation of Jupiter's equatorial stratosphere. Nature **354**, 380-382 (1991)
Li, L., Ingersoll, A.P., Huang, X.: Interaction of moist co nvection with zonal jets on Jupiter and Saturn. Icarus **180**, 113-123 (2006)
Li, X., Read, P.L.: A mechanistic model of the quasi-quadrennial oscillation in Jupiter's stratosphere. Planet. Space Sci. **48**, 637-669 (2000)
Lian, Y., Showman, A.P.: Deep jets on gas giant planets. Icarus **194,** 597-615 (2008)
Lian, Y., Showman, A.P.: Generation of zonal jets by moist convection on the giant planets. Icarus, submitted (2009)
Lindal, G.F., Sweetnam, D.N., Eshleman, V.R.: The atmosphere of Saturn: an anlysis of the Voyager radio occultation measurements. Astron. J. **90**, 1136-1146 (1985)
Lindzen, R.S., Farrell, B., Tung, K.-K.: The concept of wave overreflection and its application to barotropic instability. J. Atmos. Sci. **37**, 44-63 (1980)
Liu, J, Goldreich, P.M., Stevenson, D.J.: Constraints on deep-seated zonal winds inside Jupiter and Saturn. Icarus **196**, 653-664 (2008)
Magalhaes, J.A., et al.: Slowly moving thermal features on Jupiter. Icarus **88**, 39-72 (1990)
Massie, S.T., Hunten, D.M.: Conversion of *para* and *ortho* hydrogen in the Jovian planets. Icarus **49**, 213-226 (1982)
Mitchell, D., et al.: Saturn magnetospheric dynamics. Chapter 11, this book (2009)

Mitchell, J. L., Maxworthy, T.: Large-scale turbulence in the Jovian atmosphere. In Ghil, M., Benzi, R., Parisi, G. (eds.), Turbulence and Predictability in Geophysical Fluid Dynamics and Climate Dynamics, pp. 226-240, Societa Italiana di Fisica. (1985)
Moses, J. I., Greathouse, T.K.: Latitudinal and seasonal models of stratospheric photochemistry on Saturn: Comparison with infrared data from IRTF/TEXES. J. Geophys. Res. **110**, E09007, doi:10.1029/2005JE002450 (2005)
Moses, J.I., et al.: Meridional distribution of hydrocarbons on Satgurn: Implications for stratospheric transport. Workshop on Planetary Atmospheres, Paper #9061, Greenbelt, Maryland (2007)
Nagy, A., et al.: Saturn's upper atmosphere and ionosphere. Chapter 9, this book (2009)
Nellis, W.J., et al.: Electronic energy gap of molecular hydrogen from electrical conductivity measurements at high shock pressures. Phys. Rev. Lett. **68**, 2937-2940 (1992)
Nellis, W.J., Weir, S.T., Mitchell, A.C.: Metallization and electrical conductivity of fluid hydrogen in Jupiter. Science **273**, 936-938 (1996)
Niino, H, Misawa, N.: An experimental and theoretical study of barotropic instability, J. Atmos. Sci. **41**, 1992-2011 (1984)
Okuno, A., Masuda, A.: Effect of horizontal turbulence on the geostrophic turbulence on a beta-plane: suppression of the Rhines effect. Phys. Fluids **15**, 56-65 (2003)
Ollivier, J.L., et al.: Seasonal effects in the thermal structure of Saturn's stratosphere from infrared imaging at 10 microns. Astron. Astrophys. **356**, 347-356 (2000)
Orsolini, Y., Leovy, C.B.: A model of large-scale instabilities in the Jovian troposphere. 1. Linear model. Icarus **106**, 392-405 (1993a)
Orsolini, Y., Leovy, C.B.: A model of large-scale instabilities in the Jovian troposphere. 2. Quasi-linear model. Icarus **106**, 406-418 (1993b)
Orton, G. S., Ingersoll, A. P.: Saturn's atmospheric temperature structure and heat budget. J. Geopyhs. Res. **85**, 5871-5881 (1980)
Orton, G.S., et al.: Thermal maps of Jupiter: Spatial organization and time dependence of stratospheric temperatures, 1980 to 1990. Science **252**, 537-542 (1991)
Orton, G., Yanamandra-Fisher, P.A.: Saturn's temperature field from high-resolution middle-infrared imaging. Science **307**, 696-698 (2005)
Orton, G. A., et al.: Semi-annual oscillations in Saturn's low-latitude stratospheric temperatures. Nature **453**, 196-199 (2008)
Orton, G., et al.: Knowledge of Saturn system prior to Cassini. Chapter 3, this book (2009)
Peltier, W.R., Stuhne, G.R.: The upscale turbulent cascade: shear layers, cyclones, and gas giant bands. In Pearce, R.P. (ed.), Meteorology at the Millenium, pp. 43-61, Academic Press, New York (2002)
Pérez-Hoyos, S., et al.: Saturn's cloud structure and temporal evolution from ten years of Hubble Space Telescope images (1994-2003). Icarus **176**, 155-174 (2005)
Pérez-Hoyos, S., Sánchez-Lavega, A., French, R. G.: Short-term changes in the belt/zone structure of Saturn's Southern Hemisphere (1996-2004). Astronomy and Astrophysics **460,** 641-645 (2006)
Piccioni, G., et al.: South-polar features on Venus similar to those near the north. Nature **450**, 637-640 (2007)
Pirraglia, J.A.: Dissipationless decay of Jovian jets. Icarus **79**, 196-207 (1989)
Pirraglia, J.A., et al.: Thermal structure and dynamics of Jupiter and Saturn. Nature **292**, 677–679 (1981)
Porco, C.C., et al.: Cassini imaging of Jupiter's atmosphere, satellites, and rings. Science **299**, 1541-1547 (2003)
Porco, C.C., et al.: Cassini imaging science: Instrument characteristics and capabilities and anticipated scientific investigations at Saturn. Space Sci. Rev. **115**, 363-497 (2004)
Porco, C.C., et al.: Cassini imaging science: Initial results on Saturn's atmosphere. Science **307**, 1243–1247 (2005)
Read, P.L., et al.: Jupiter's and Saturn's convectively driven banded jets in the laboratory. Geophys. Res. Lett. **31**, L22701 (2004)
Read, P.L., et al.: Dynamics of convectively driven banded jets in the laboratory. J. Atmos. Sci. **64**, 4031-4052 (2007)
Read, P.L., et al.: Mapping potential vorticity dynamics on Jupiter: 1. Zonal mean circulation from Cassini and Voyager 1 data. Quart. J. Roy. Meteor. Soc. **132**, 1577-1603 (2006a)
Read, P.L., Gierasch, P.J., Conrath, B.J.: Mapping potential-vorticity dynamics on Jupiter: II: the Great Red Spot from Voyager 1 and 2 data. Quart. J. Roy. Meteor. Soc. **132**, 1605-1625 (2006b)
Read, P.L., et al.: Mapping potential vorticity dynamics on Saturn: Zonal mean circulation from Cassini and Voyager data. Planet. Space Sci., in press (2009)
Rhines, P.B.: Waves and turbulence on a beta-plane. J. Fluid Mech. **69**, 417-443 (1975)
Rieke, G. H.: The thermal radiation of Saturn and its rings. Icarus **26**, 37-44 (1975)
Salyk, C., et al.: Interaction between eddies and mean flow in Jupiter's atmosphere: Analysis of Cassini imaging data. Icarus **185**, 430–442 (2006)
Sánchez-Lavega, A.: Motions in Saturn's atmosphere: before Voyager encounters. Icarus **49**, 1–16 (1982)
Sánchez-Lavega, A.: Saturn's Great White Spots. Sky and Telescope **78**, 141 - 143 (1989)
Sanchez-Lavega, A. , Battaner, E.: Long-term changes in Saturn's atmospheric belts and zones. Astr. Astrophys. Suppl. Ser. **64**, 287−301 (1986)
Sánchez-Lavega, A., Battaner, E.: The nature of Saturn's atmospheric Great White Spots. Astron. Astrophys. **185**, 315-326 (1987)
Sánchez-Lavega, A., et al.: The great white spot and disturbances in Saturn's equatorial atmosphere during 1990. Nature **353**, 397-401 (1991)
Sánchez-Lavega, A. et al.: Temporal behavior of cloud morphologies and motions in Saturn's atmosphere, Journal of Geophysical Research **98** (E10), 18857 - 18872 (1993a)
Sánchez-Lavega, A., et al.: Ground-based observations of Saturn's north polar spot and hexagon. Science **260**, 329-332 (1993b)
Sánchez-Lavega, A. et al.: Photometry of Saturn's 1990 equatorial disturbance. Icarus **108**, 158 - 168 (1994)
Sánchez-Lavega, A., et al.: Large-scale storms in Saturn's atmosphere during 1994. Science **271**, 631-634 (1996)
Sánchez-Lavega, A., et al.: New observations and studies of Saturn's long-lived north polar spot. Icarus **128**, 322-334 (1997)
Sánchez-Lavega, A., et al.: Discrete cloud activity in Saturn's equator during 1995, 1996, and 1997. Planet. Space Sci. **47**, 1277-1283 (1999)
Sánchez-Lavega, A., Rojas, J.F., Sada, P.V.: Saturn's zonal winds at cloud level. Icarus **147**, 405–420 (2000)
Sánchez-Lavega. A.: Observations of Saturn's ribbon wave 14 years after its discovery. Icarus **158**, 272-275 (2002a)
Sánchez-Lavega, A., et al.: No hexagonal wave around Saturn's Southern Pole. Icarus, **160** 216-219 (2002b)

Sánchez-Lavega, A., et al.: A strong decrease in Saturn's equatorial jet at cloud level. Nature **423**, 623-625 (2003)
Sánchez-Lavega, A., et al.: Observations and models of the general circulation of Jupiter and Saturn. In Ulla, A., Manteiga, M. (eds.), Lecture Notes and Essays in Astrophysics I, pp. 63-85. Real Sociedad Española de Física, Universidad de Vigo (2004a)
Sánchez-Lavega, A., et al.: Saturn's cloud morphology and zonal winds before the Cassini encounter. Icarus **170**, 519-523 (2004b)
Sánchez-Lavega, A., et al.: A strong vortex in Saturn's South Pole, Icarus **184**, 524-531 (2006)
Sánchez-Lavega, A., Hueso, R., Pérez-Hoyos, S.: The three-dimensional structure of Saturn's equatorial jet at cloud level. Icarus **187**, 510-519 (2007)
Sayanagi, K.M., Showman, A.P.: Effects of a large convective storm on Saturn's equatorial jet. Icarus **187,** 520-539 (2007)
Sayanagi, K.M., Showman, A.P., Dowling, T.E.: The emergence of multiple robust zonal jets from freely-evolving, three-dimensional stratified geostrophic turbulence with applications to Jupiter. J. Atmos. Sci. **65,** 3947-3962 (2008)
Schneider, T., Liu, J.J.: Formation of jets and equatorial superrotation on Jupiter. J. Atmos. Sci. **66**, 579-601 (2009)
Schumacher, C., Houze, R.A. Jr.: Stratiform precipitation production over sub-Saharan Africa and the tropical east Atlantic as observed by TRMM. Quart. J. Roy. Meteor. Soc, **132**, 2235-2255 (2006)
Scott, R.K., Polvani, L.M.: Forced-dissipative shallow-water turbulence on the sphere and the atmospheric circulation of the giant planets. J. Atmos. Sci. **64**, 3158-3176 (2007)
Scott, R.K., Polvani, L.M.: Equatorial superrotation in shallow atmospheres. Geophys. Res. Letters **35**, L24202, doi:10.1029/2008GL036060 (2008)
Showman, A.P.: Numerical simulations of forced shallow-water turbulence: effects of moist convection on the large-scale circulation of Jupiter and Saturn. J. Atmos. Sci. **64,** 3132-3157 (2007)
Showman, A.P., de Pater , I.: Dynamical implications of Jupiter's tropospheric ammonia abundance. Icarus **174**, 192-204 (2005)
Showman, A.P., Gierasch, P.J., Lian, Y.: Deep zonal winds can result from shallow driving in a giant-planet atmosphere. Icarus **182,** 513-526 (2006)
Smith, B.A., et al.: The Jupiter system through the eyes of Voyager 1. Science **204**, 951-972 (1979)
Smith, B.A., et al.: Encounter with Saturn:Voyager 1 imaging Science results. Science **212**, 163–190 (1981)
Smith, B. A., et al.: A new look at the Saturn system: The Voyager 2 images. Science **215**, 504-537 (1982)
Smith, K.S.: A local model for planetary atmospheres forced by small-scale convection. J. Atmos. Sci. **61**, 1420-1433 (2004)
Sommeria, J., Meyers, S.D., Swinney, H.: Experiments on vortices and Rossby waves in eastward and westward jets. In A. R. Osborne (ed.), Nonlinear Topics in Ocean Physics, pp. 227-269, North-Holland, Amsterdam (1991)
Sromovsky, L.A., et al.: Jovian winds from Voyager 2. Part II: Analysis of eddy transports. J. Atmos. Sci. **39**, 1413-1432 (1982)
Sromovsky, L.A., et al.: Voyager 2 observations of Saturn's northern mid-latitude cloud features: Morphology, motions, and evolution. J. Geophys. Res. **88**, 8650-8666 (1983)
Stephens, G.L., et al.: The CloudSat mission and the A-Train: A new dimension to space-based observations of clouds and precipitation. Bull. Amer. Meteor. Soc. **83**, 1771-1790 (2002)
Sukoriansky, S., Galperin, B., Dikovskaya, N.: Universal spectrum of two-dimensional turbulence on a rotating sphere and some basic features of atmospheric circulation on giant planets. Phys. Rev. Lett. **89**, 124501-1-124501-4 (2002)
Sukoriansky, S., Dikovskaya, N., Galperin, B.: On the arrest of inverse energy cascade and the Rhines scale. J. Atmos. Sci. **64**, 3312-3327 (2007)
Sukoriansky, S., Dikovskaya, N., Galperin, B.: Nonlinear waves in zonostrophic turbulence. Phys. Rev. Lett. **101**, 178501 (2008)
Temma, T., et al.: Vertical structure modeling of Saturn's equatorial region using high spectral resolution imaging. Icarus **175**, 464-489 (2005)
Theiss, J.: Equatorward energy cascade, critical latitude, and the predominance of cyclonic vortices in geostrophic turbulence. J. Phys. Ocean. **34**, 1663-1678 (2004)
Tokunaga, A. T., et al.: Spatially resolved infrared observations of Saturn: II. The temperature enhancement at the south pole of Saturn. Icarus **36**, 216-222 (1978)
Tomasko, M.G., West, R.A., Orton, G.S., Teifel, V.G.: Cloud and aerosols in Saturn's atmosphere. In Gehrels, T., Matthews, M.S., (eds.), Saturn, pp. 150-194, U. of Arizona Press, Tucson (1984)
Trafton, L.: Long-term changes in Saturn's troposphere. Icarus **63**, 374-405 (1985)
Vasavada, A.R., Showman, A.P.: Jovian atmospheric dynamics: an update after Galileo and Cassini. Rep. Prog. Phys. **68**, 1935-1996 (2006)
Vasavada, A., et al.: Cassini imaging of Saturn: southern hemisphere winds and vortices. J. Geophys. Res. **111**, E05004, doi:10.1029/2005JE002563 (2006)
Weidenschilling, S.J., Lewis, J.S.: Atmospheric and cloud structures of the Jovian planets. Icarus **20**, 465-476 (1973)
Weir, S.T., Mitchell, A.C., Nellis, W.J.: Metallization of fluid molecular hydrogen at 140 GPa. Phys. Rev. Lett. **76**, 1860-1863 (1996)
West et al.. Saturn clouds and aerosols. Chapter 8, this book (2009)
Westphal, J.A., et al.: Hubble Space Telescope observations of the 1990 equatorial disturbance on Saturn – images, albedos, and limb darkening. Icarus **100**, 485-498 (1992)
Williams, G.P.: Planetary circulations 1: Barotropic representations of Jovian and terrestrial turbulence. J. Atmos. Sci. **35**, 1399-1426 (1978)
Williams, G.P.: Jovian dynamics. Part III: Multiple, migrating, and equatorial jets. J. Atmos. Sci. **60**, 1270-1296 (2003)
Wordsworth, R.D., Read, P.L., Yamazaki , Y.H.: Turbulence, waves and jets in a differentially heated rotating annulus experiment, Phys. Fluids **20**, 126602 (2008)
Yamazaki, Y.H., Read, P.L., Skeet, D.R.: Hadley circulations and Kelvin wave-driven equatorial jets in the atmospheres of Jupiter and Saturn. Planet. Space Sci. **53**, 508-525 (2005)
Yanamandra-Fisher, P.A., et al.: Saturn's 5.2-μm cold spots: Unexpected cloud variability. Icarus **150**, 189-193 (2001)
Zipser, E.J., et al.: Where are the most intense thunderstorms on Earth? Bull. Amer. Meteor. Soc. **87**, 1057-1071 (2006)
Zuchowski, L.C., Read, P.L., Yamazaki , Y.H.: Modeling Jupiter's cloud bands and decks: 1. Jet scale meridional circulations on Jupiter. Icarus **200**, 548-562 (2009)

## Figure Captions

**Fig. 7.1.** Saturn Southern Hemisphere zonal wind profiles from the Cassini ISS data of Vasavada et al. (2006) based on the Voyager SKR rotation period (solid) and the Anderson and Schubert (2007) rotation period (dotted).

**Fig. 7.2.** VIMS views of Saturn's upper level hazes at 0.9 μm (left) and lower tropospheric clouds in thermal emission at 5.1 μm (right). Here, the original thermal image is shown photometrically reversed so the backlit silhouetted clouds are bright and holes in the clouds are dark, thus giving a more typical black and white view of clouds as they might be observed in sunlight if the overlying hazes were to disappear (Baines et al., 2009c).

**Fig. 7.3.** RADAR (upper; Janssen et al. 2008) vs. VIMS (lower; Baines et al. 2009c) cylindrical mosaics of Saturn. In the RADAR view, dark discrete features near 6°N and S latitude represent enhanced ammonia gas absorption at the 1.4-2.0 bar level underneath and at the ammonia condensation level near 1.4 bar. The latitudes, size, and shape of these gaseous features correlate well with the discrete cloud plumes seen in the equatorial region in 5-μm imagery, suggesting that the discrete clouds observed underneath the thick upper-level haze of Saturn are formed from ammonia gas condensation near the 1.4-bar level.

**Fig. 7.4.** Cassini ISS image mosaics of northern (upper left) and southern (lower left) midlatitudes in a continuum filter, and of the same northern latitudes in weak methane band (upper right) and moderate strength methane band (lower right) filters. Latitudes are planetocentric.

**Fig. 7.5.** Southern Hemisphere ISS continuum image with superimposed mean zonal wind profile (Vasavada et al., 2006).

**Fig. 7.6.** (a) Zonally-averaged zonal flow on Saturn, and (b) northward gradient of $\xi$ (solid line) and $\beta = df/dy$ (dashed line). Northern Hemisphere profiles were derived from Voyager images by Sanchez-Lavega et al. (2000) and Godfrey (1988), and Southern Hemisphere profiles from Cassini ISS images by Vasavada et al. (2006) and Sanchez-Lavega et al. (2006).

**Fig. 7.7.** Latitudinal profile of VIMS 5 μm cloud-tracked winds (black dots). Shown for comparison are Voyager (blue) and Cassini ISS continuum (red) wind profiles (Choi et al. 2009).

**Fig. 7.8.** Cross-section of temperature retrieved from Cassini CIRS nadir observations during the prime mission. The region between 5 and 50 mbar is not shown since the spectra are not sensitive to temperatures in that pressure range. Vertical dashed lines indicate the latitudes of the prograde (eastward) jets. (after Fletcher et al. 2007b).

**Fig. 7.9.** Comparison of Voyager, HST, and Cassini ISS wind profiles derived from images in filters sensing different vertical levels at different times (Sánchez-Lavega et al. (2000, 2003, 2007).

**Fig. 7.10.** Thermal winds derived from CIRS retrieved temperatures in the upper troposphere and stratosphere (upper panel) and their relationship to cloud-tracked winds at the visible cloud top derived from the results of Godfrey (1988), Vasavada et al. (2006), and Sánchez-Lavega et al. (2000, 2006)(lower panel) (Read et al., 2009).

**Fig. 7.11.** Vertical temperature profiles in the tropopause region at 20°N (dotted line), equator (solid line) and 20°S (dashed line) from Cassini CIRS data, showing a knee in the upper tropospheric temperature profile. (Fletcher et al. 2007b**).**

**Fig. 7.12.** Latitudinal profiles of 2 mbar ethane (upper) and acetylene (lower) abundance derived from CIRS data (from Howett et al. 2007).

**Fig. 7.13.** Time series of brightness temperatures at 7.8 μm ($CH_4$) and 12.2 μm ($C_2H_6$) obtained from ground-based observations. The temperatures are the difference of those at latitudes 15.5° and 3.6°. A sinusoidal best fit of the individual data (black curve) has a period of 15.6 years; the corresponding best fit of the annual average (dashed curve) yields a period of 15.0 years. After Orton et al. (2008).

**Fig. 7.14.** Upper: Meridional cross section of temperatures (K) obtained from CIRS limb sounding in the mid infrared. Note that the equator is alternatively colder and warmer with altitude relative to adjacent latitudes. Lower: Zonal winds, computed from the thermal wind equation along cylinders concentric about Saturn's rotation axis. The winds are relative to the winds at the 20-mbar (hPa) level. Positive winds are eastward. The dashed parabola encloses a zone of exclusion not accessible from the thermal wind equation. Winds within this region have been interpolated along isobars. After Fouchet et al. (2008).

**Fig. 7.15.** Meridional cross section of $C_2H_6$ from CIRS mid-infrared limb sounding.

**Fig. 7.16.** Profiles of Ertel potential vorticity ($q_E$, solid line) and mean zonal wind (u, dashed line) at $\theta = 160$ K in the upper troposphere, obtained by Read et al. (2009) from Cassini imaging and CIRS data. $q_E$ is normalised by the horizontal mean value of $g\partial\theta/\partial p$ to give a potential vorticity in units of $s^{-1}$.

**Fig. 7.17.** Outbreaks of intense moist convective storms on Saturn. Left upper: False color composite of Cassini ISS images of the 2004 dragon storm at 35°S in near-infared continuum (CB2) and moderate/strong methane band (MT2/MT3) filters. Redder shades indicate lower cloud tops, bluer shades higher cloud tops, and whiter shades high optically thick clouds and hazes. Right upper: HST Wide Field Planetary Camera 2 true color image of the 1994 equatorial Great White Spot. Lower: VIMS false color composite of a convective storm (yellow) near 35ºS in 2008 (Baines et al. 2009b).

**Fig. 7.18.** Schematic vertical-latitudinal cross-section of the region between the visible cloud level and water condensation level indicating the eastward (E) and westward (W) jet locations and associated eddy momentum flux, observed preferred locations of convective clouds, inferred meridional overturning circulation, and eddy heat fluxes for a possible baroclinic instability source of eddies. Observed aspects of the circulation are shown in red and inferred or hypothesized features in black. Adapted from Hartmann (2007).

**Fig. 7.19.** Top: Zonal mean wind velocity from Voyager imaging data. Middle and bottom: Observed amplitude and phase of the zonal wavenumber 2 thermal wave at 130 mbar from Voyager 1 IRIS data. From Achterberg and Flasar (1996).

**Fig. 7.20.** The north polar hexagon as seen in CIRS 100 mb temperatures (left; Fletcher et al. 2008) and in VIMS 5 μm emission (Baines et al. 2009a).

**Fig. 7.21.** Left: Typical profiles with radius of zonal flow and radial vorticity gradient in the barotropic instability laboratory experiments of Aguiar et al. (2009). Right: Streak image showing the fully developed hexagonal jet and weak anticyclonic peripheral vortices in the barotropically unstable jet flows.

**Fig. 7.22.** Left: False-color polar stereographic image of the south polar vortex. The image is made up of MT3, MT2, and CB2 images projected into the blue, green, and red color planes, respectively. High thin clouds therefore appear blue or green, low level clouds red, and thick clouds with high tops bright pink. The lower panels show a time sequence over 2.83 hr showing the shadows cast by the high clouds of the inner eyewall; the position of the Sun is indicated by the arrows. Right: ISS cloud-tracked zonal winds vs. latitude (panel A) and corresponding relative vorticity values (panel B). The solid curves in A represent constant absolute vorticity for a parcel moving poleward from latitude $\varphi_o$ . The solid surve in B is the vorticity corresponding to the wind profile in A; the points in B are vorticities for the bright puffy clouds in the left panel. The vertical dashed lines in A and B indicate the locations of the inner and outer "eyewalls." (From Dyudina et al. 2008).

**Fig. 7.23.** Upper: CIRS temperature anomalies at 160 mbar at the ribbon wave latitude (Fletcher et al. 2007c). Lower: 5 μm VIMS image illustrating the string-of-pearls and annular cloud features (Baines et al. 2009c).

**Fig. 7.24.** Examples of the zonal wind field in 3-D numerical models of gas giant atmospheres that produce both equatorial superrotation and multiple higher latitude alternating jets. Left: The 3-D shallow atmosphere model of Lian and Showman (2009) with 3x solar water abundance. Right: The 3-D convective cylinder model of Heimpel and Aurnou (2007) with inner/outer shell radius = 0.85 (warm/cool colors indicate eastward/westward flow).

**Fig. 7.25.** Histograms of eddy momentum flux north and south of a westward jet (left) observed in Cassini ISS images (Del Genio et al. 2007a) and (right) produced by baroclinic instability in the simulations of Lian and Showman (2008).

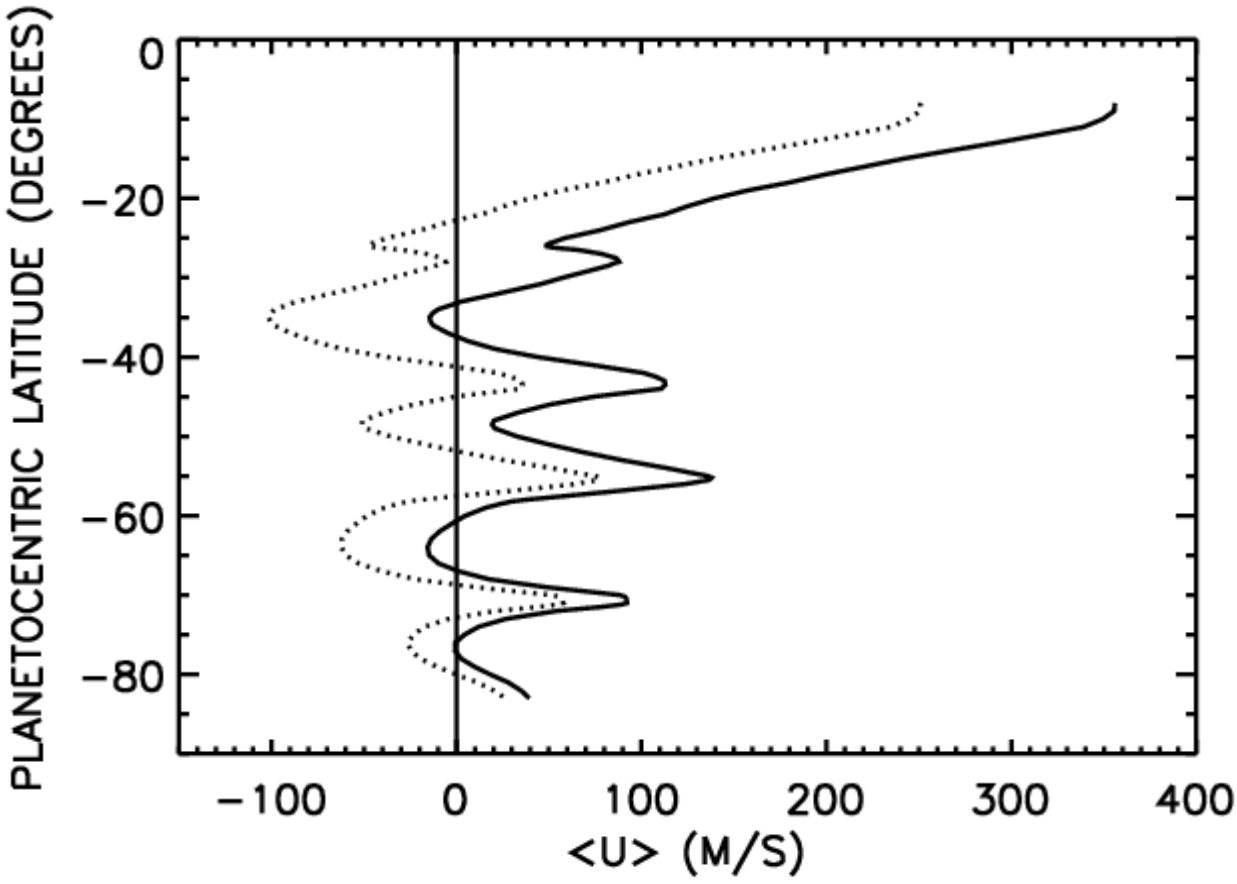


**Fig. 7.1.** Saturn Southern Hemisphere zonal wind profiles from the Cassini ISS data of Vasavada et al. (2006) based on the Voyager SKR rotation period (solid) and the Anderson and Schubert (2007) rotation period (dotted).

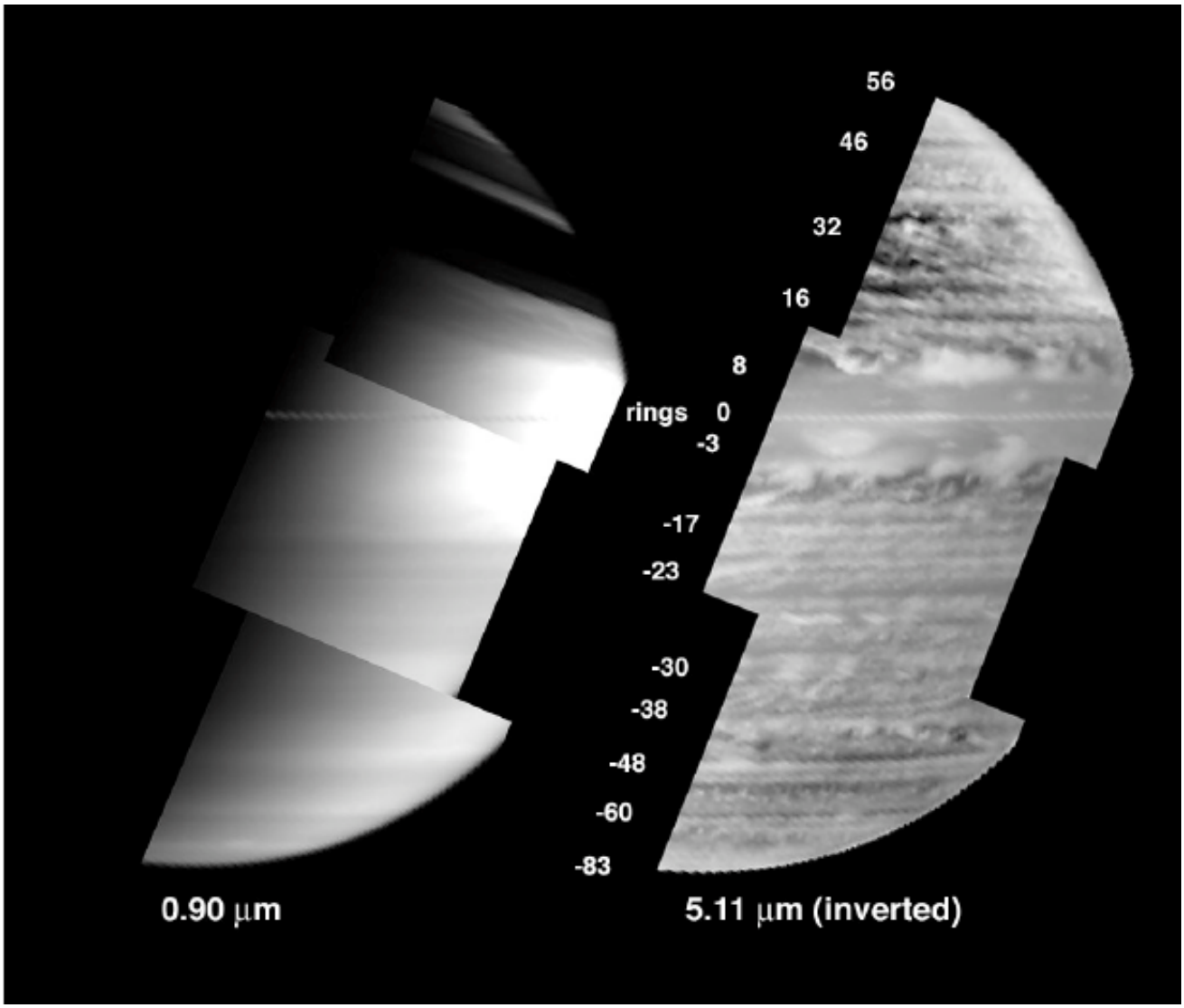


**Fig. 7.2.** VIMS views of Saturn's upper level hazes at 0.9 μm (left) and lower tropospheric clouds in thermal emission at 5.1 μm (right). Here, the original thermal image is shown photometrically reversed so the backlit silhouetted clouds are bright and holes in the clouds are dark, thus giving a more typical black and white view of clouds as they might be observed in sunlight if the overlying hazes were to disappear (Baines et al., 2009c).

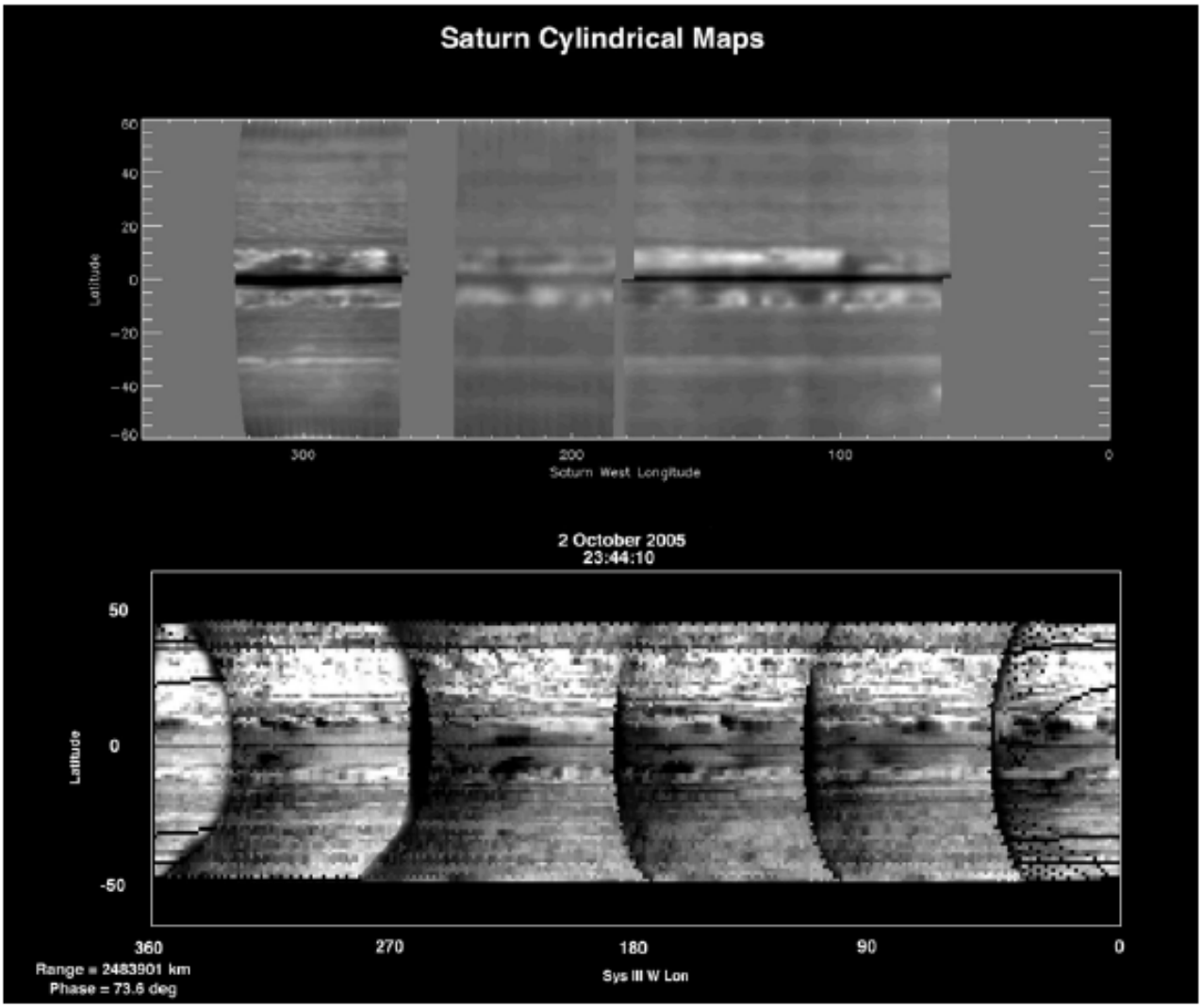


**Fig. 7.3.** RADAR (upper; Janssen et al. 2008) vs. VIMS (lower; Baines et al. 2009c) cylindrical mosaics of Saturn. In the RADAR view, dark discrete features near 6°N and S latitude represent enhanced ammonia gas absorption at the 1.4-2.0 bar level underneath and at the ammonia condensation level near 1.4 bar. The latitudes, size, and shape of these gaseous features correlate well with the discrete cloud plumes seen in the equatorial region in 5-μm imagery, suggesting that the discrete clouds observed underneath the thick upper-level haze of Saturn are formed from ammonia gas condensation near the 1.4-bar level.

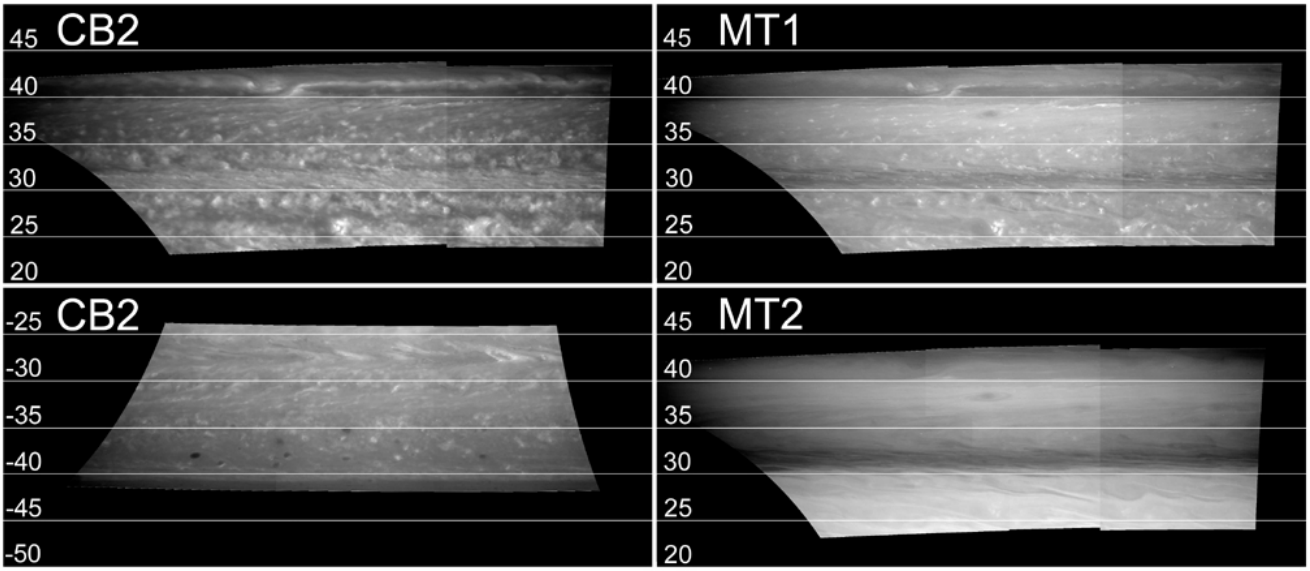


**Fig. 7.4.** Cassini ISS image mosaics of northern (upper left) and southern (lower left) midlatitudes in a continuum filter, and of the same northern latitudes in weak methane band (upper right) and moderate strength methane band (lower right) filters. Latitudes are planetocentric.

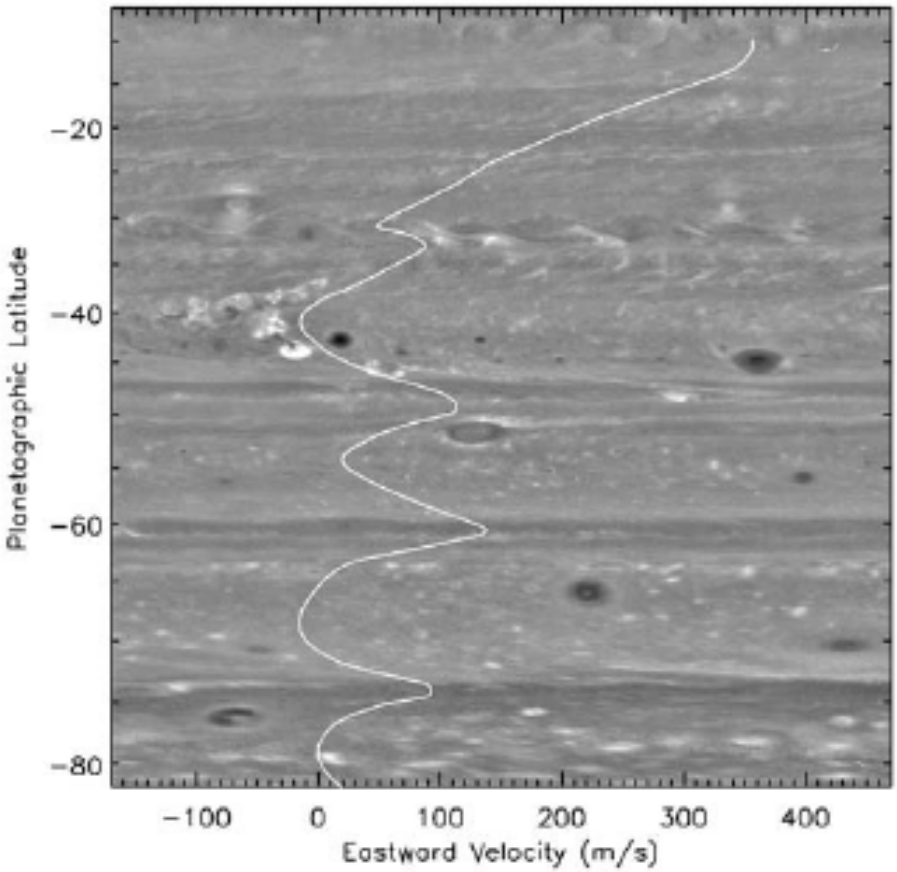


**Fig. 7.5.** Southern Hemisphere ISS continuum image with superimposed mean zonal wind profile (Vasavada et al., 2006).

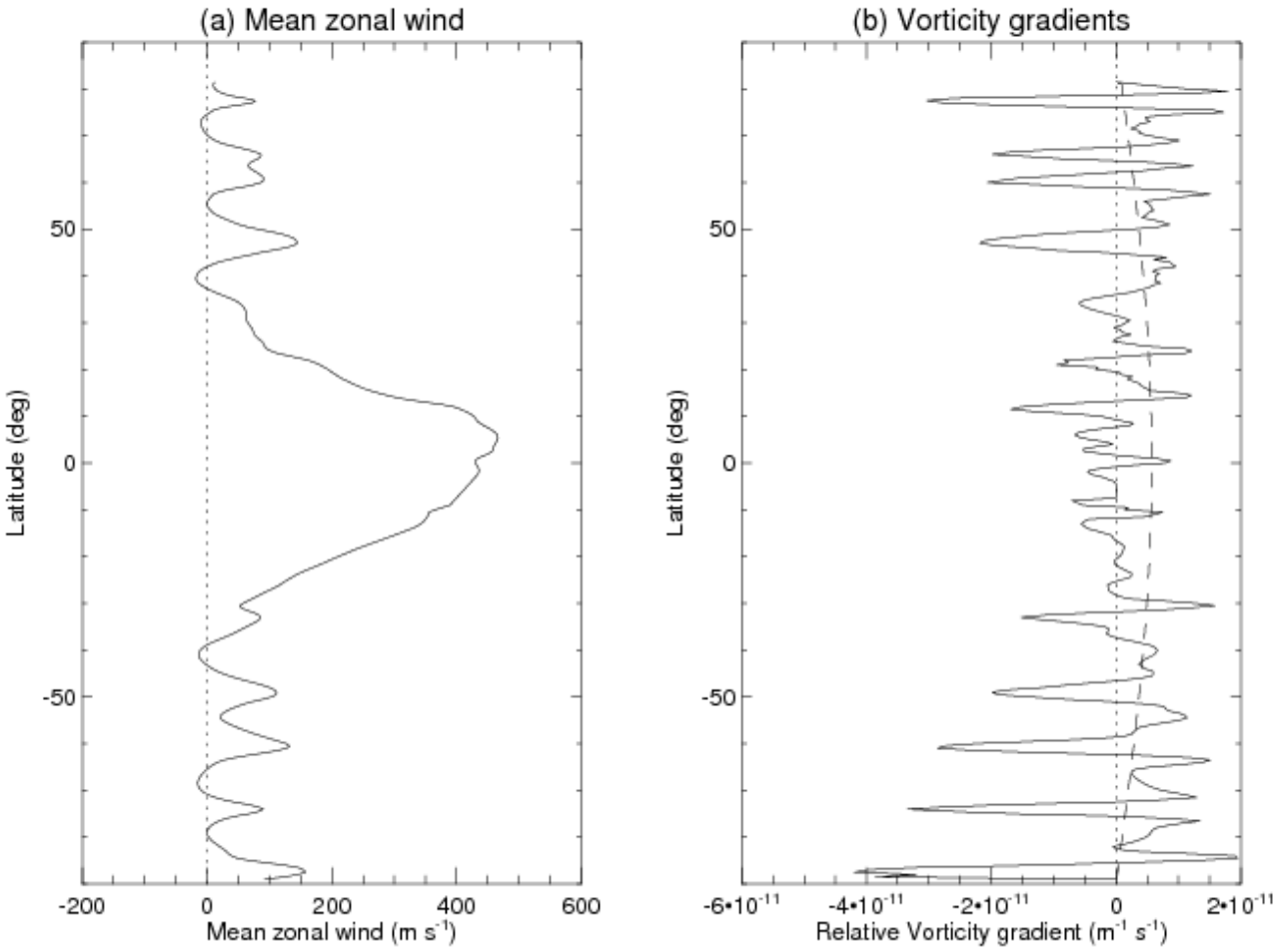


**Fig. 7.6.** (a) Zonally-averaged zonal flow on Saturn, and (b) northward gradient of $\xi$ (solid line) and $\beta = df/dy$ (dashed line). Northern Hemisphere profiles were derived from Voyager images by Sanchez-Lavega et al. (2000) and Godfrey (1988), and Southern Hemisphere profiles from Cassini ISS images by Vasavada et al. (2006) and Sanchez-Lavega et al. (2006).

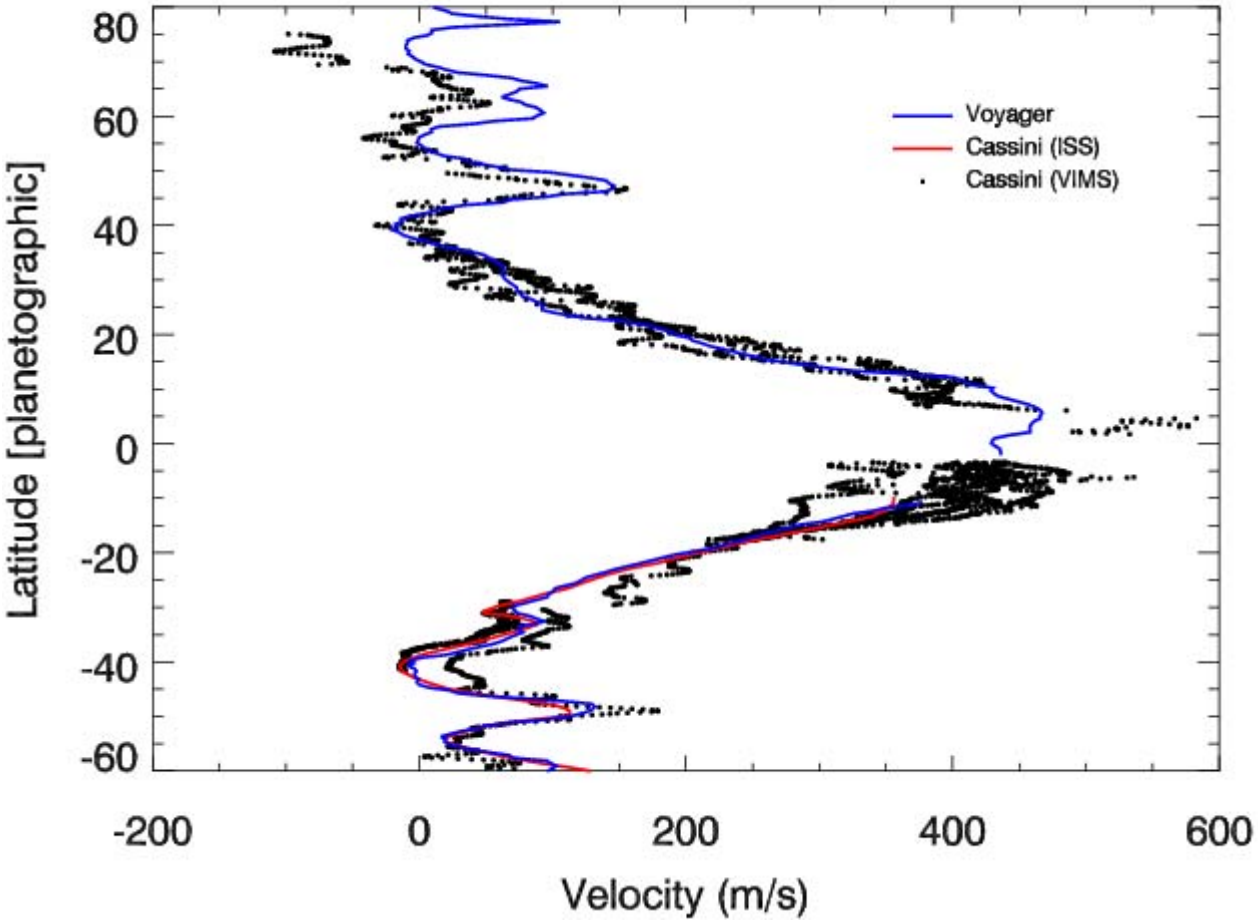


**Fig. 7.7.** Latitudinal profile of VIMS 5 μm cloud-tracked winds (black dots). Shown for comparison are Voyager (blue) and Cassini ISS continuum (red) wind profiles (Choi et al. 2009).

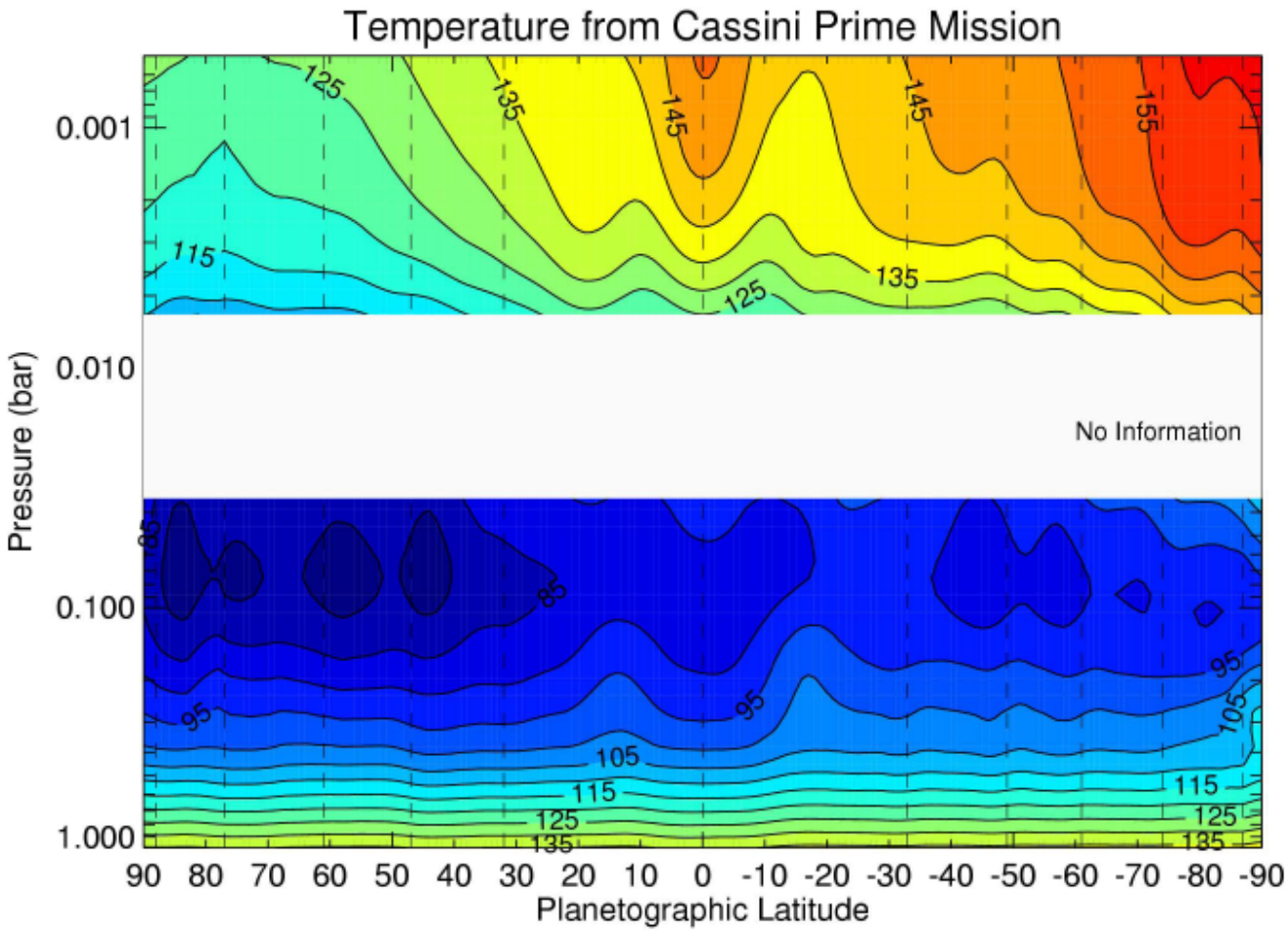


**Fig. 7.8.** Cross-section of temperature retrieved from Cassini CIRS nadir observations during the prime mission. The region between 5 and 50 mbar is not shown since the spectra are not sensitive to temperatures in that pressure range. Vertical dashed lines indicate the latitudes of the prograde (eastward) jets. (after Fletcher et al. 2007b).

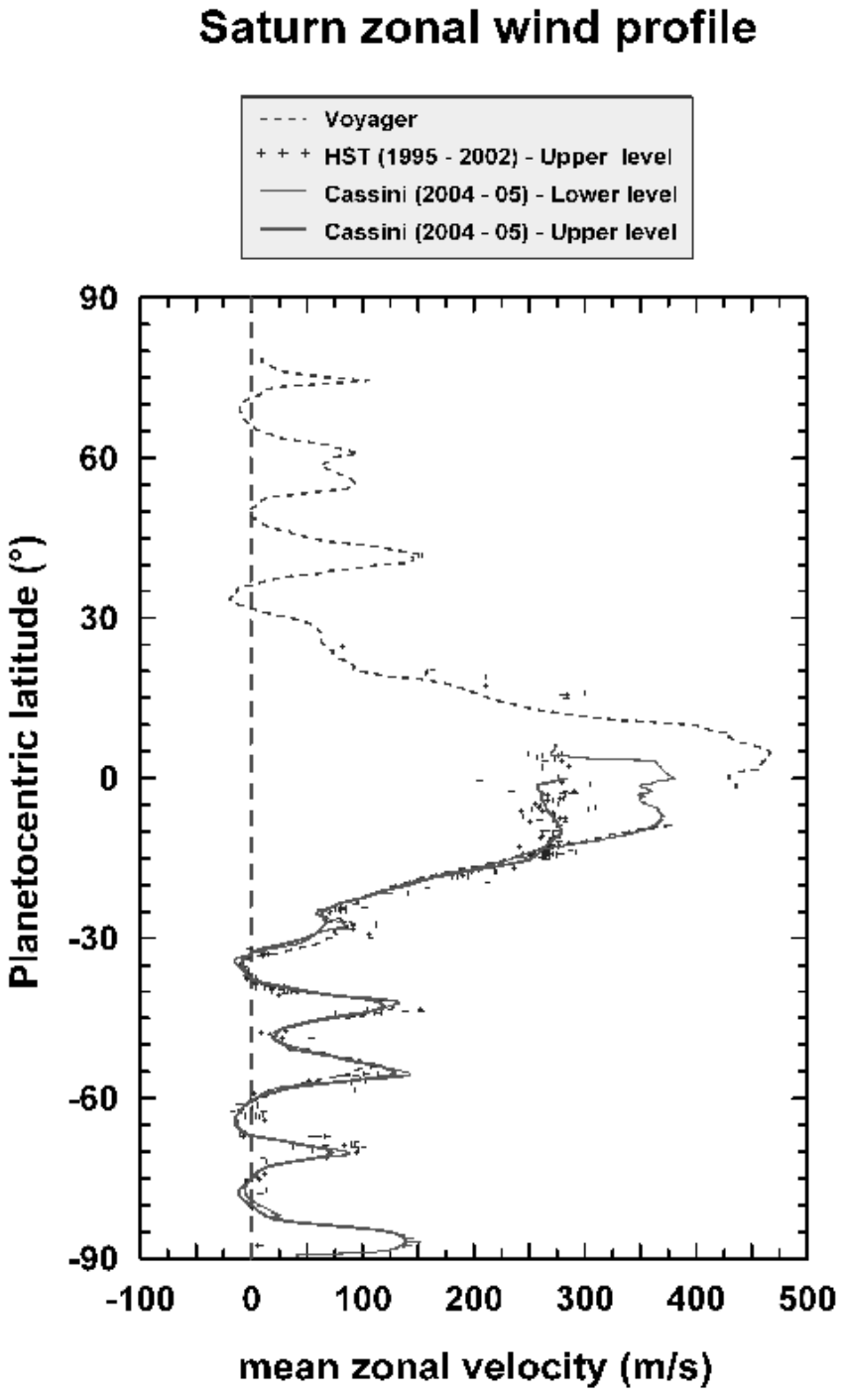


**Fig. 7.9.** Comparison of Voyager, HST, and Cassini ISS wind profiles derived from images in filters sensing different vertical levels at different times (Sánchez-Lavega et al. (2000, 2003, 2007).

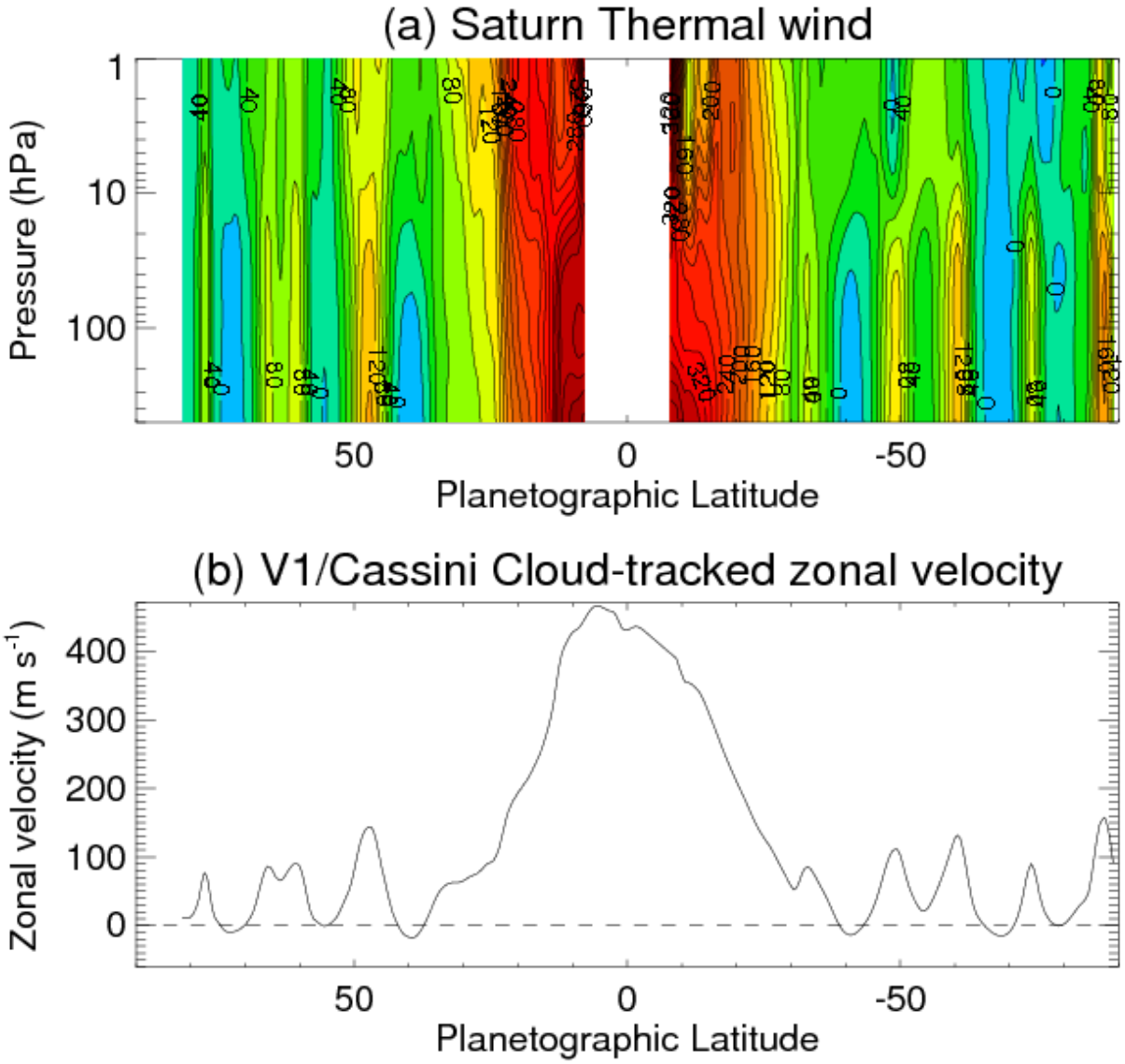


**Fig. 7.10.** Thermal winds derived from CIRS retrieved temperatures in the upper troposphere and stratosphere (upper panel) and their relationship to cloud-tracked winds at the visible cloud top derived from the results of Godfrey (1988), Vasavada et al. (2006), and Sánchez-Lavega et al. (2000, 2006)(lower panel) (Read et al., 2009).

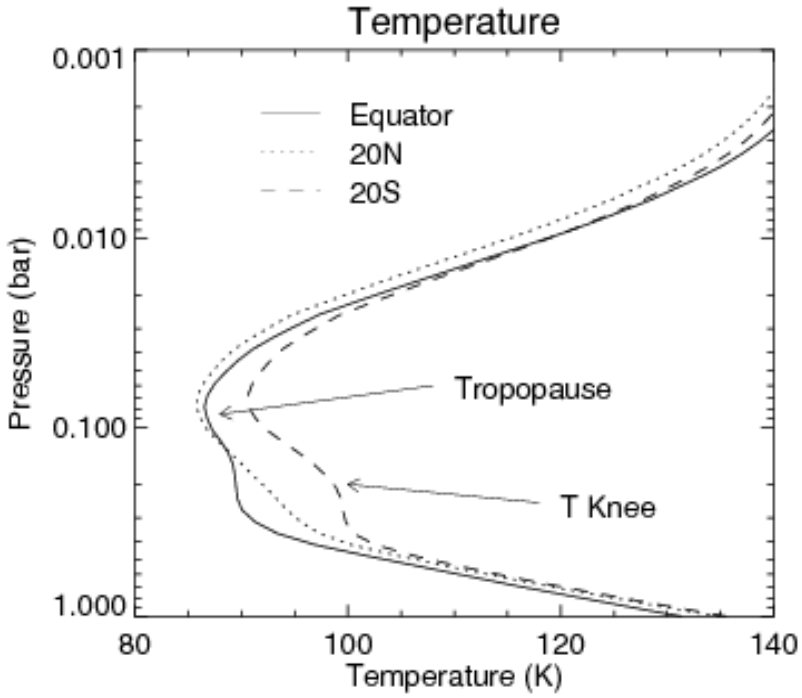


**Fig. 7.11.** Vertical temperature profiles in the tropopause region at 20°N (dotted line), equator (solid line) and 20°S (dashed line) from Cassini CIRS data, showing a knee in the upper tropospheric temperature profile. (Fletcher et al. 2007b)**.**

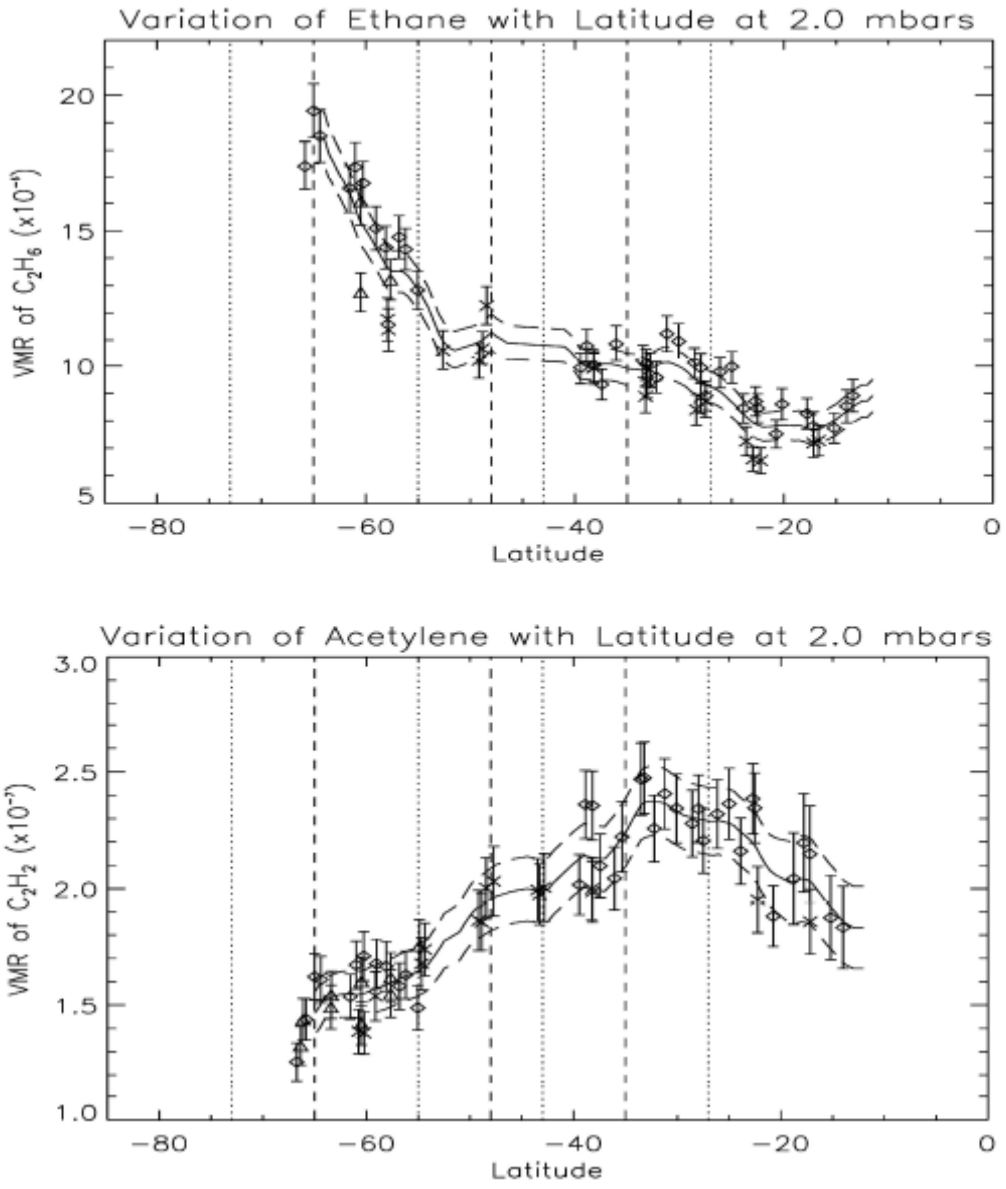


**Fig. 7.12.** Latitudinal profiles of 2 mbar ethane (upper) and acetylene (lower) abundance derived from CIRS data (from Howett et al. 2007).

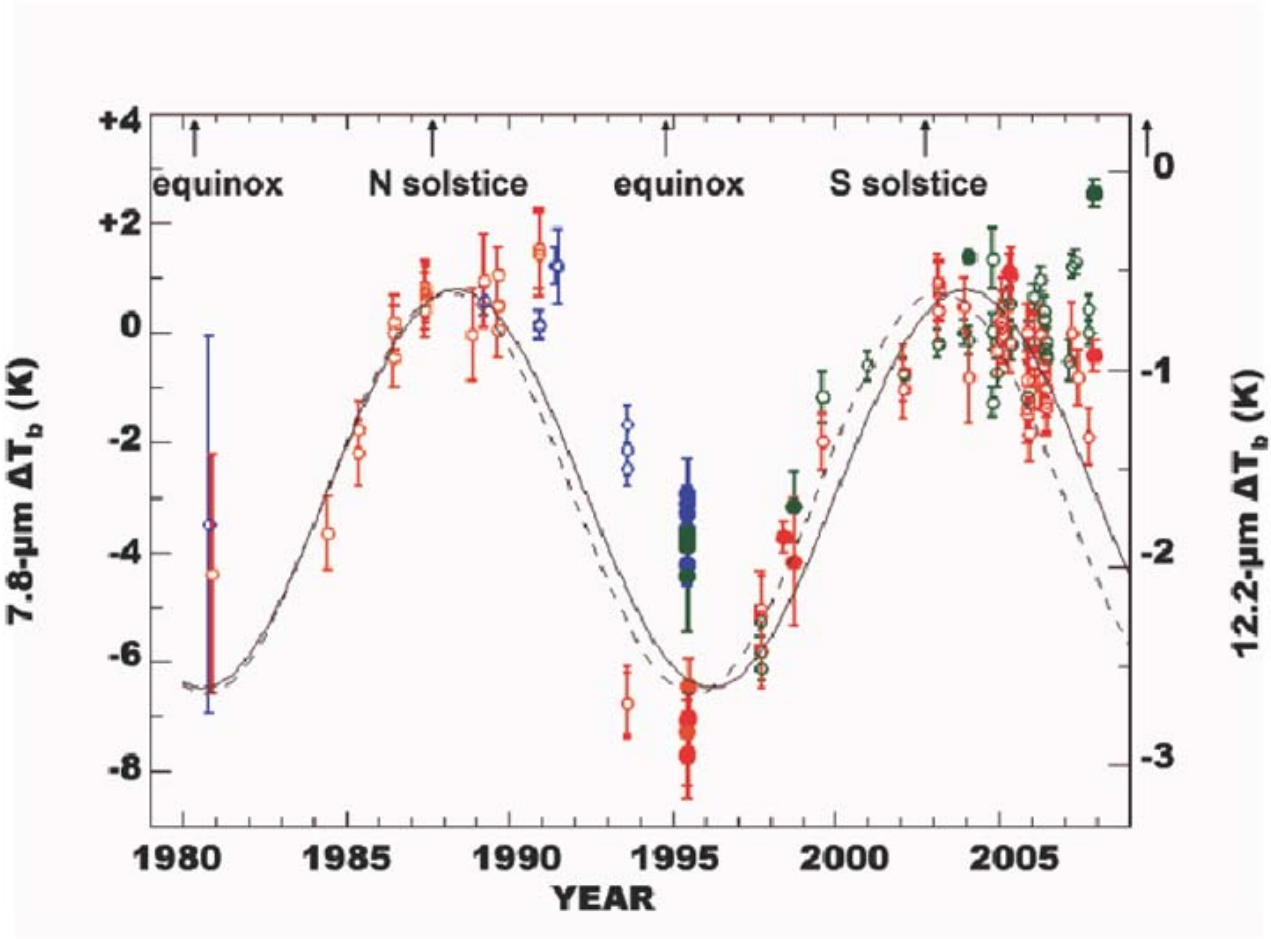


**Fig. 7.13.** Time series of brightness temperatures at 7.8 μm ($CH_4$) and 12.2 μm ($C_2H_6$) obtained from ground-based observations. The temperatures are the difference of those at latitudes 15.5° and 3.6°. A sinusoidal best fit of the individual data (black curve) has a period of 15.6 years; the corresponding best fit of the annual average (dashed curve) yields a period of 15.0 years. After Orton et al. (2008).

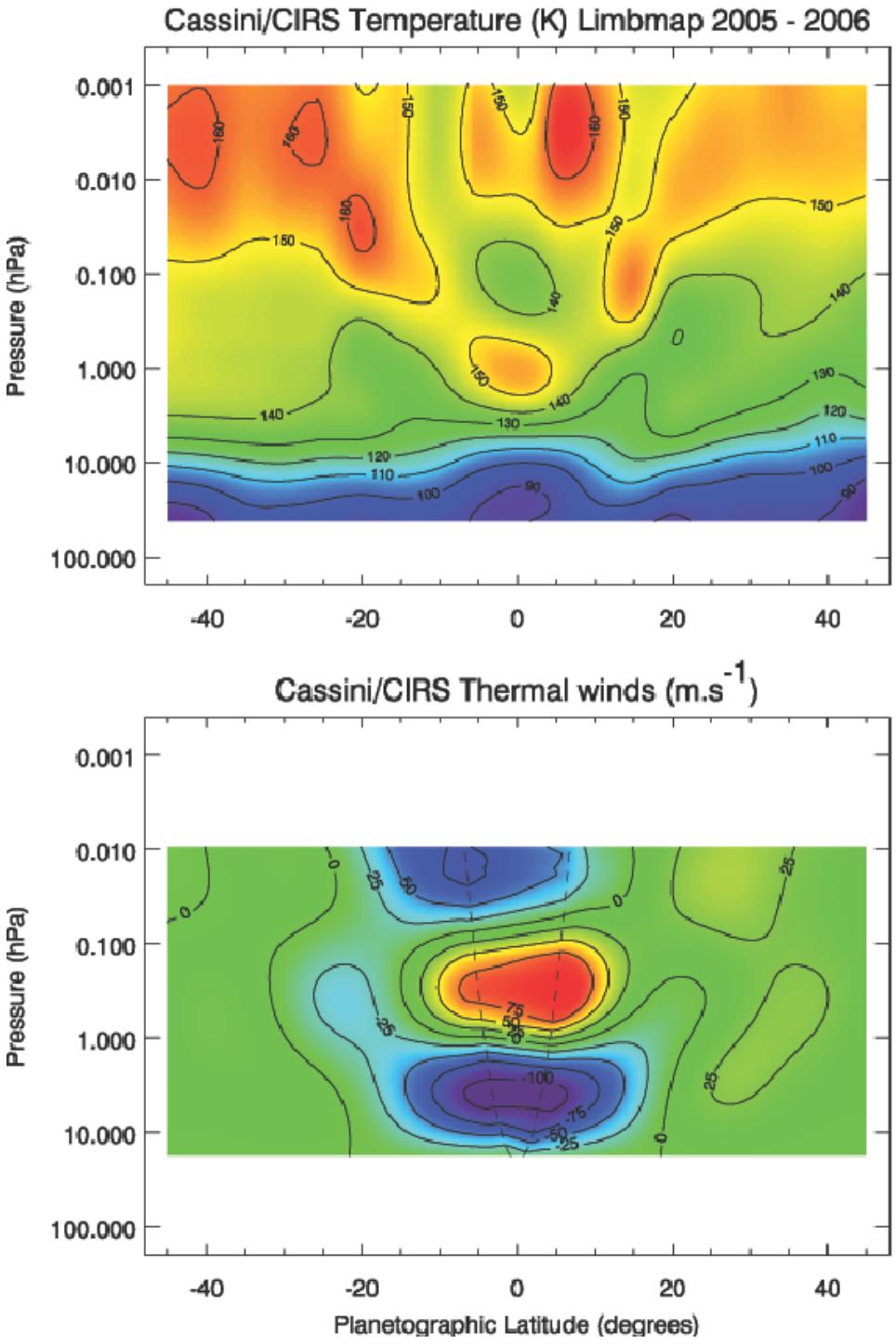


**Fig. 7.14.** Upper: Meridional cross section of temperatures (K) obtained from CIRS limb sounding in the mid infrared. Note that the equator is alternatively colder and warmer with altitude relative to adjacent latitudes. Lower: Zonal winds, computed from the thermal wind equation along cylinders concentric about Saturn's rotation axis. The winds are relative to the winds at the 20-mbar (hPa) level. Positive winds are eastward. The dashed parabola encloses a zone of exclusion not accessible from the thermal wind equation. Winds within this region have been interpolated along isobars. After Fouchet et al. (2008).

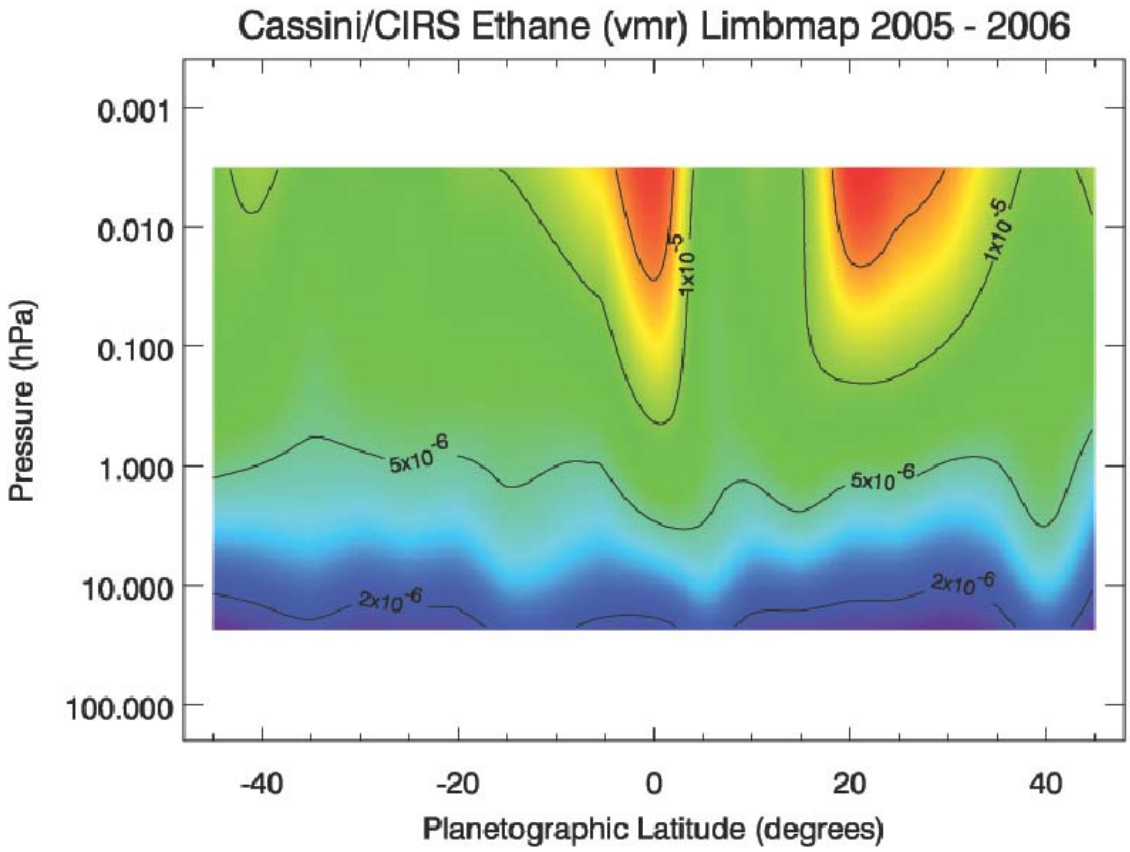


**Fig. 7.15.** Meridional cross section of $C_2H_6$ from CIRS mid-infrared limb sounding.

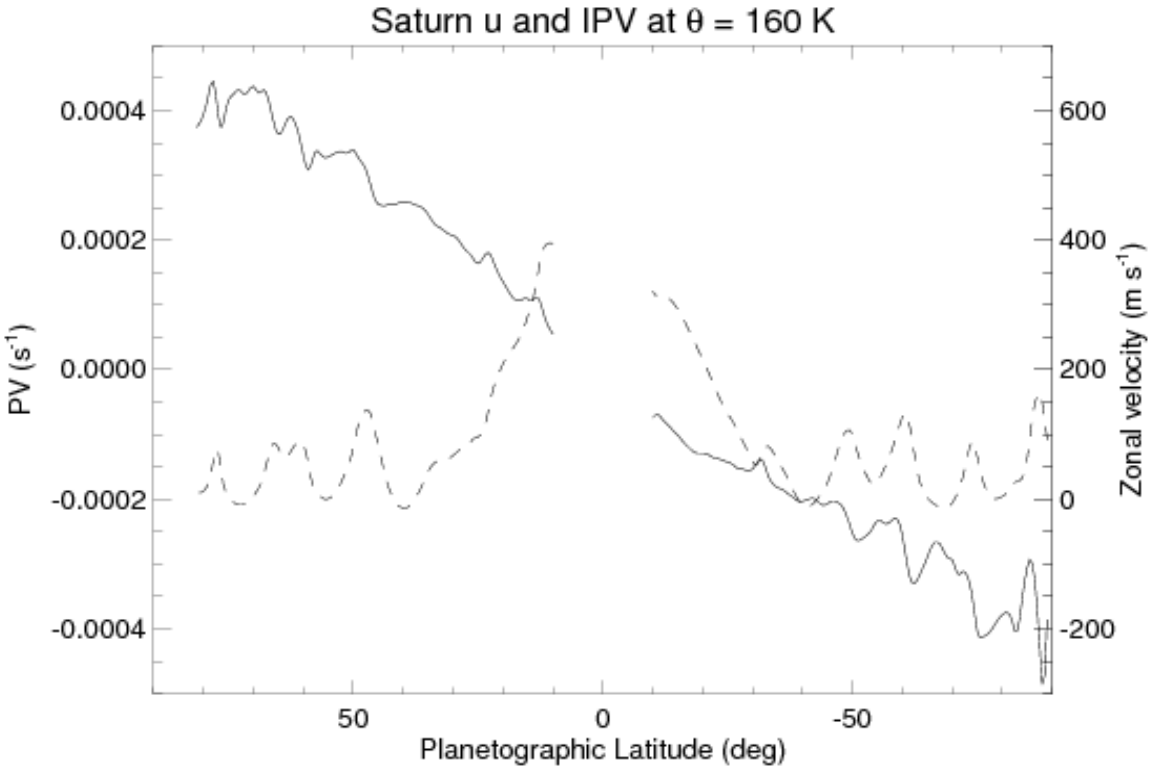


**Fig. 7.16.** Profiles of Ertel potential vorticity ($q_E$, solid line) and mean zonal wind (u, dashed line) at $\theta$ = 160 K in the upper troposphere, obtained by Read et al. (2009) from Cassini imaging and CIRS data. $q_E$ is normalised by the horizontal mean value of $g\partial\theta/\partial p$ to give a potential vorticity in units of $s^{-1}$.

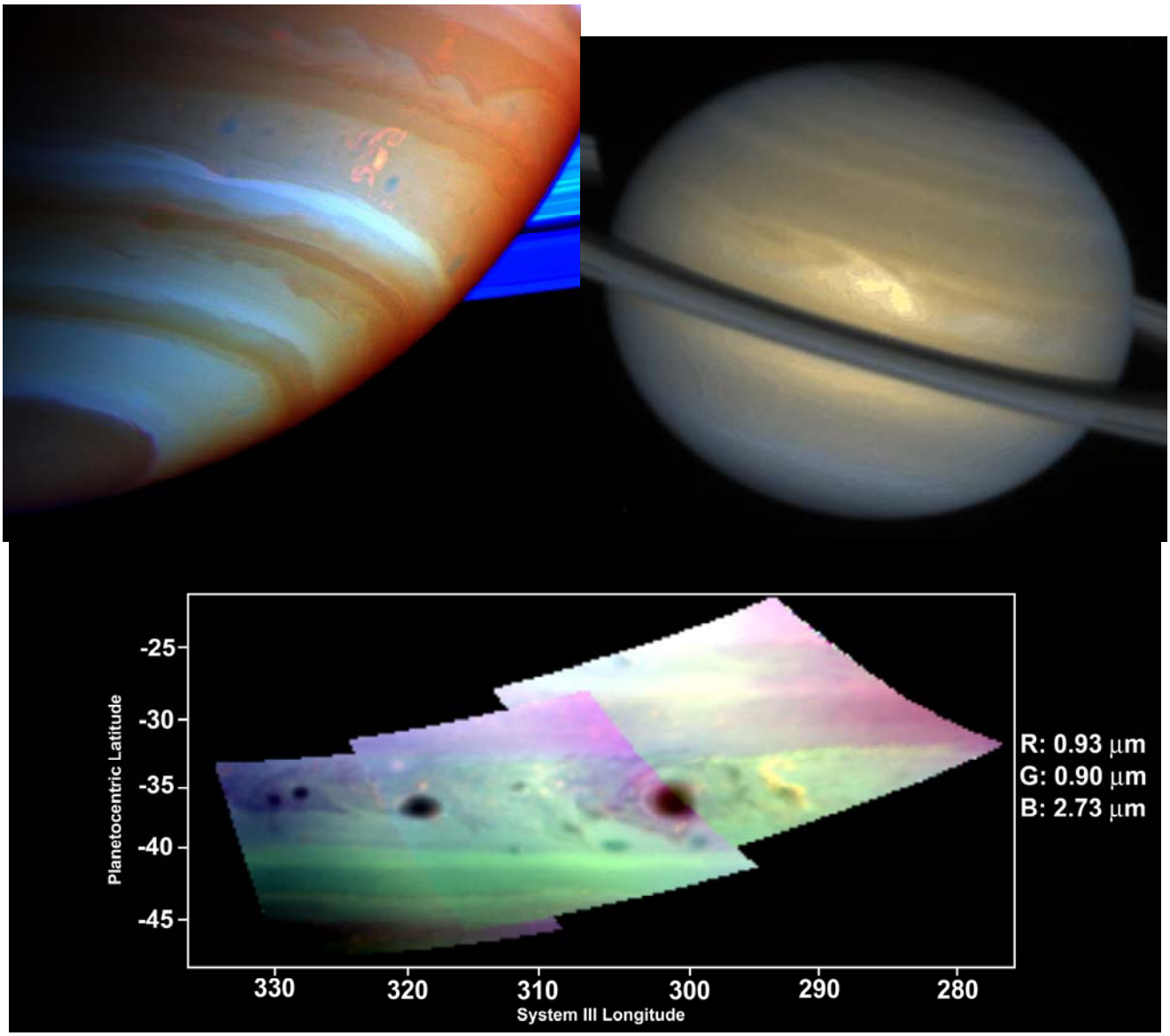


**Fig. 7.17.** Outbreaks of intense moist convective storms on Saturn. Left upper: False color composite of Cassini ISS images of the 2004 dragon storm at 35°S in near-infared continuum (CB2) and moderate/strong methane band (MT2/MT3) filters. Redder shades indicate lower cloud tops, bluer shades higher cloud tops, and whiter shades high optically thick clouds and hazes. Right upper: HST Wide Field Planetary Camera 2 true color image of the 1994 equatorial Great White Spot. Lower: VIMS false color composite of a convective storm (yellow) near 35ºS in 2008 (Baines et al. 2009b).

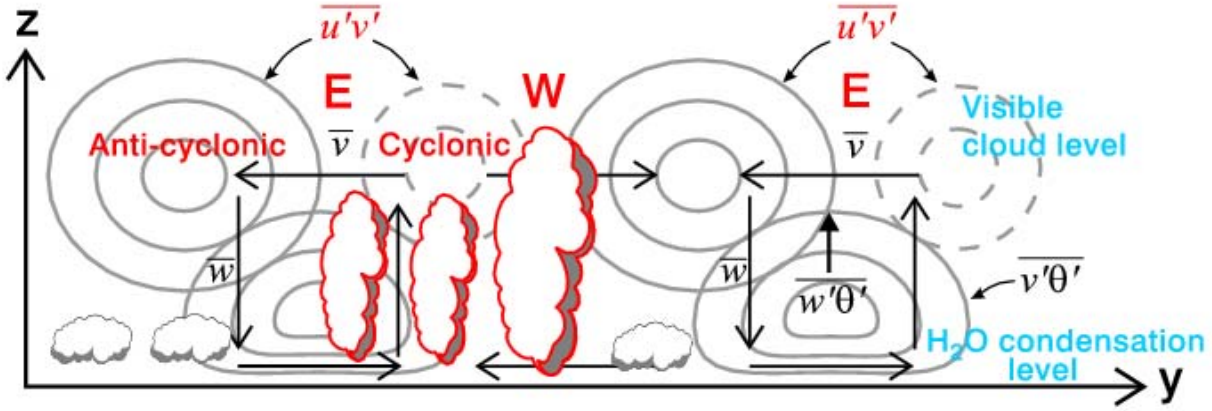


**Fig. 7.18.** Schematic vertical-latitudinal cross-section of the region between the visible cloud level and water condensation level indicating the eastward (E) and westward (W) jet locations and associated eddy momentum flux, observed preferred locations of convective clouds, inferred meridional overturning circulation, and eddy heat fluxes for a possible baroclinic instability source of eddies. Observed aspects of the circulation are shown in red and inferred or hypothesized features in black. Adapted from Hartmann (2007).

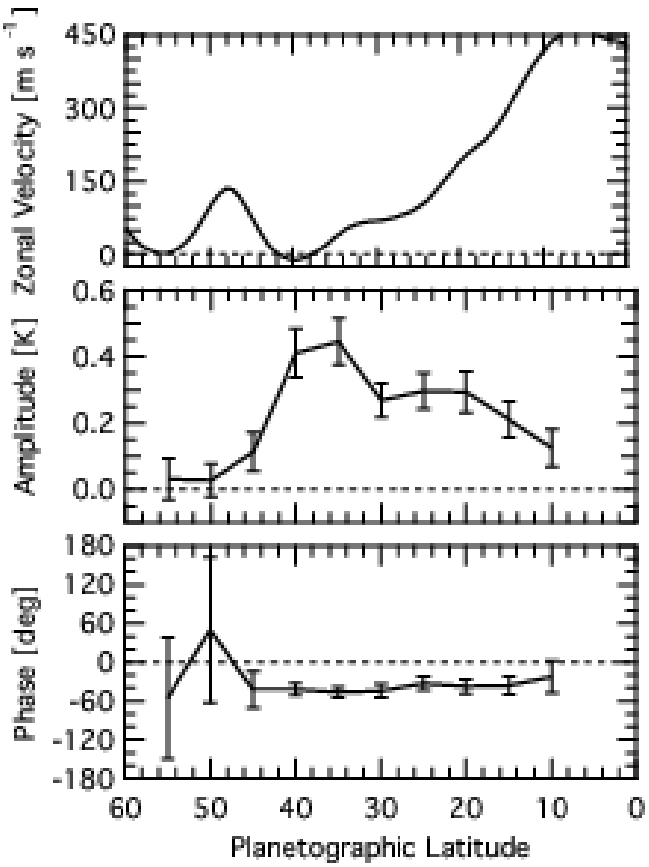


**Fig. 7.19.** Top: Zonal mean wind velocity from Voyager imaging data. Middle and bottom: Observed amplitude and phase of the zonal wavenumber 2 thermal wave at 130 mbar from Voyager 1 IRIS data. From Achterberg and Flasar (1996).

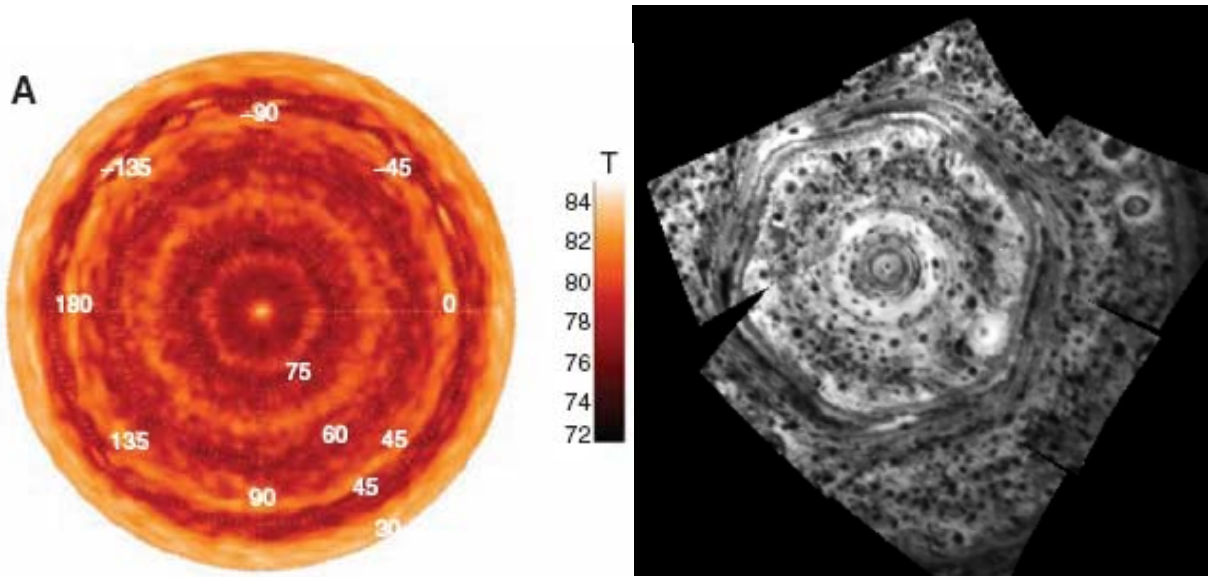


**Fig. 7.20.** The north polar hexagon as seen in CIRS 100 mb temperatures (left; Fletcher et al. 2008) and in VIMS 5 μm emission (Baines et al. 2009a).

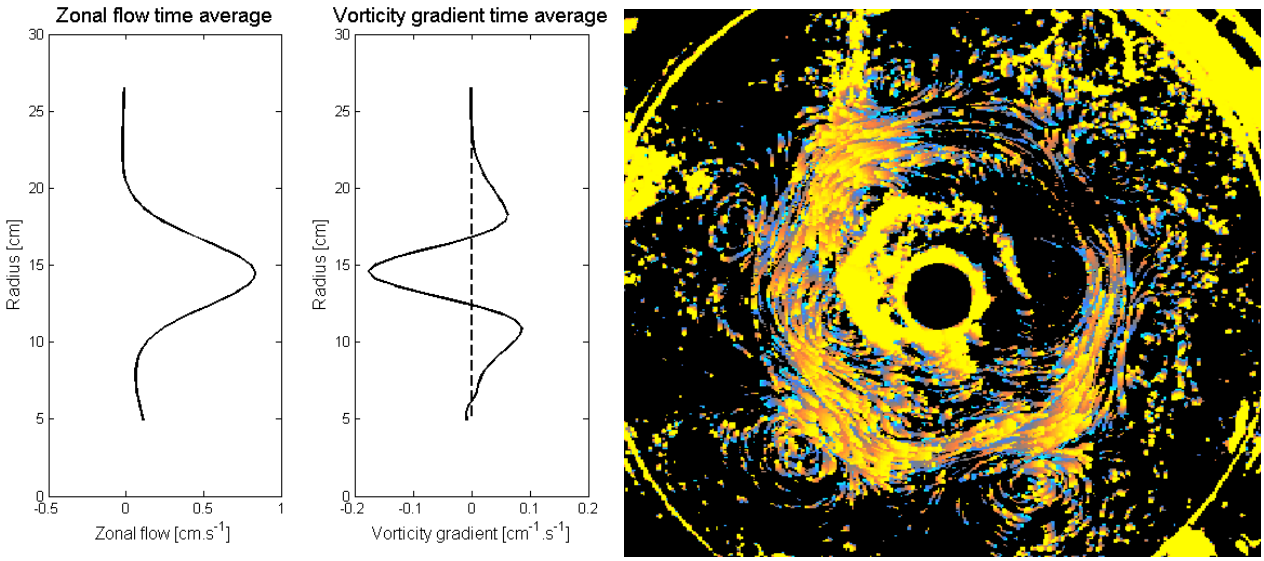


**Fig. 7.21.** Left: Typical profiles with radius of zonal flow and radial vorticity gradient in the barotropic instability laboratory experiments of Aguiar et al. (2009). Right: Streak image showing the fully developed hexagonal jet and weak anticyclonic peripheral vortices in the barotropically unstable jet flows.

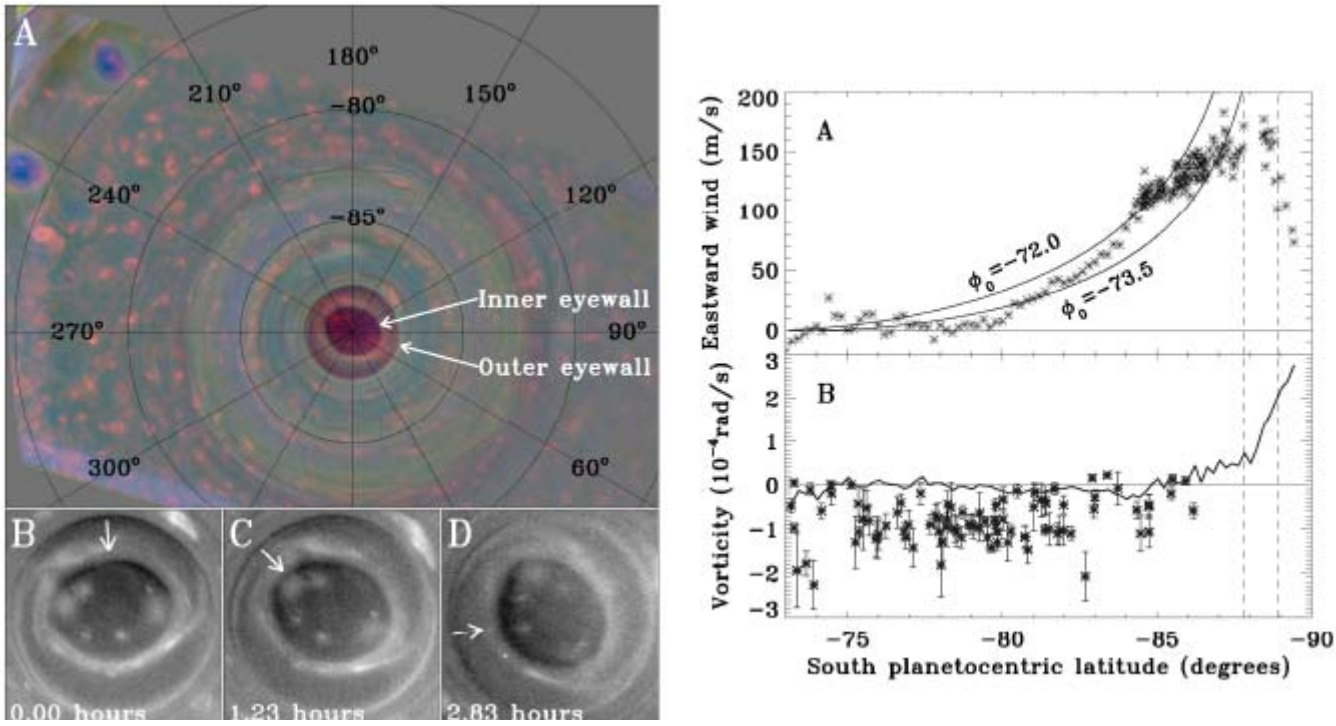


**Fig. 7.22.** Left: False-color polar stereographic image of the south polar vortex. The image is made up of MT3, MT2, and CB2 images projected into the blue, green, and red color planes, respectively. High thin clouds therefore appear blue or green, low level clouds red, and thick clouds with high tops bright pink. The lower panels show a time sequence over 2.83 hr showing the shadows cast by the high clouds of the inner eyewall; the position of the Sun is indicated by the arrows. Right: ISS cloud-tracked zonal winds vs. latitude (panel A) and corresponding relative vorticity values (panel B). The solid curves in A represent constant absolute vorticity for a parcel moving poleward from latitude $\varphi_o$ . The solid surve in B is the vorticity corresponding to the wind profile in A; the points in B are vorticities for the bright puffy clouds in the left panel. The vertical dashed lines in A and B indicate the locations of the inner and outer "eyewalls." (From Dyudina et al. 2008).

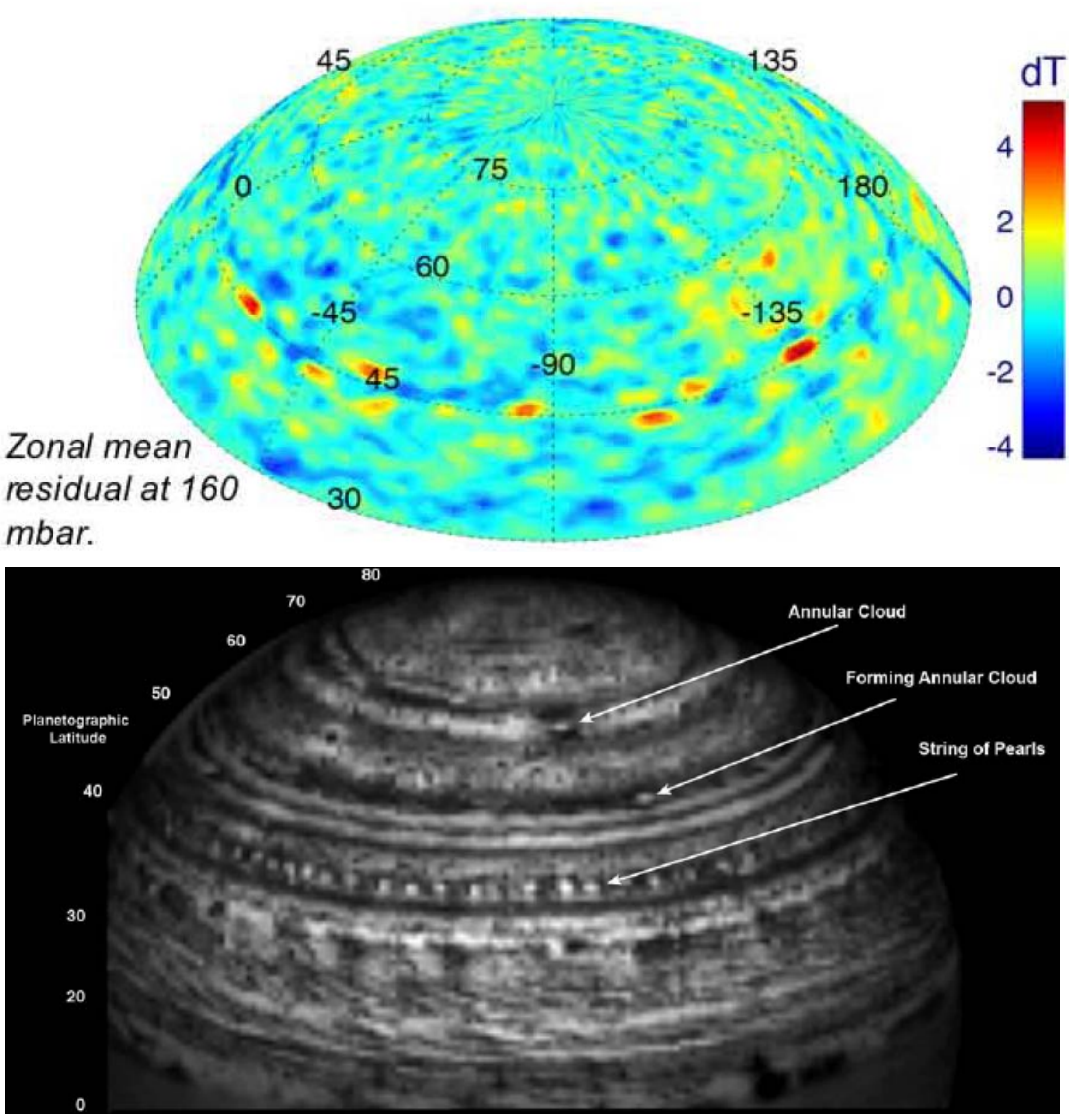


**Fig. 7.23.** Upper: CIRS temperature anomalies at 160 mbar at the ribbon wave latitude (Fletcher et al. 2007c). Lower: 5 μm VIMS image illustrating the string-of-pearls and annular cloud features (Baines et al. 2009c).

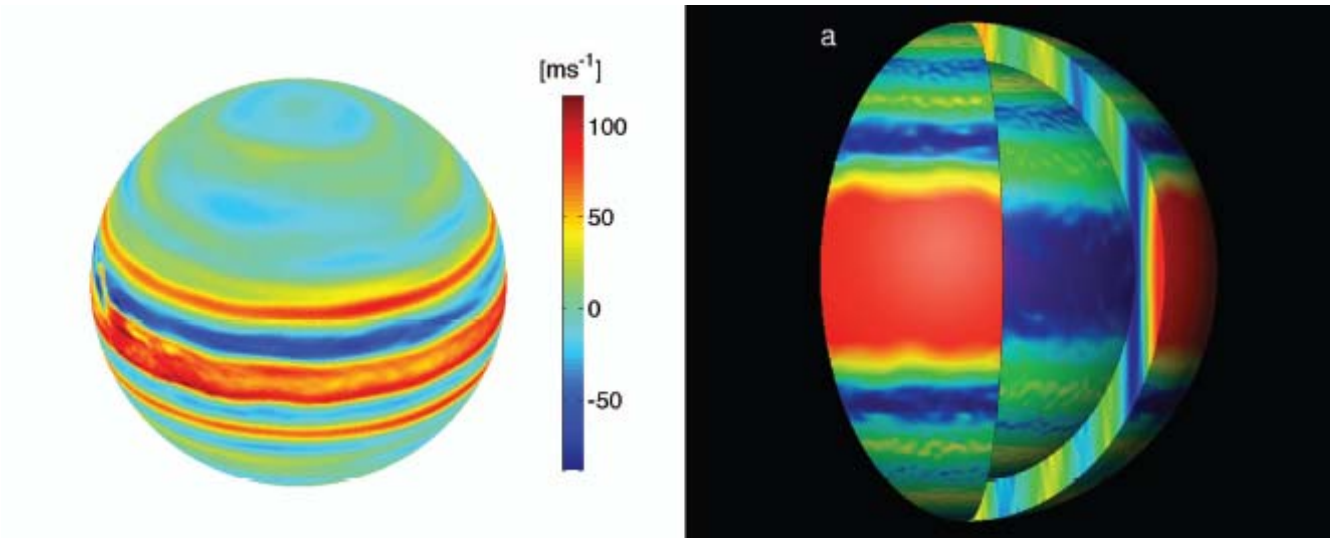


**Fig. 7.24.** Examples of the zonal wind field in 3-D numerical models of gas giant atmospheres that produce both equatorial superrotation and multiple higher latitude alternating jets. Left: The 3-D shallow atmosphere model of Lian and Showman (2009) with 3x solar water abundance. Right: The 3-D convective cylinder model of Heimpel and Aurnou (2007) with inner/outer shell radius = 0.85 (warm/cool colors indicate eastward/westward flow).

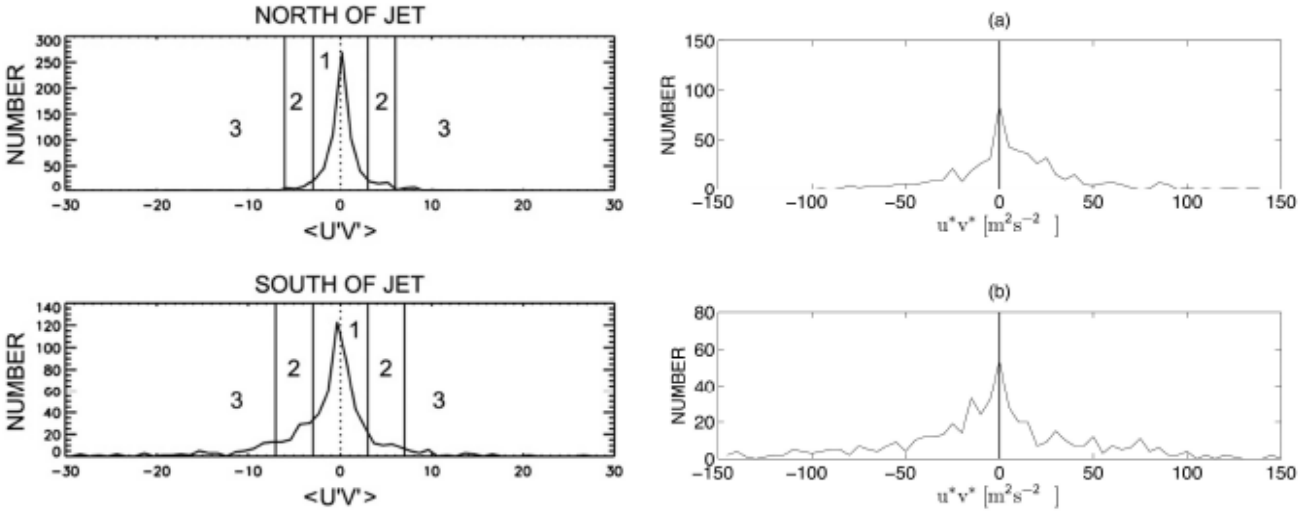


**Fig. 7.25.** Histograms of eddy momentum flux north and south of a westward jet (left) observed in Cassini ISS images (Del Genio et al. 2007a) and (right) produced by baroclinic instability in the simulations of Lian and Showman (2008).